




5-2010

## **Multi-scale Simulation of Linear, Short-Chain Polyethylene Liquids under Flow Conditions**

Jun Mo Kim

*The University of Tennessee*, [jkim31@utk.edu](mailto:jkim31@utk.edu)

Follow this and additional works at: [https://trace.tennessee.edu/utk\\_graddiss](https://trace.tennessee.edu/utk_graddiss)

 Part of the [Complex Fluids Commons](#), and the [Polymer Science Commons](#)

---

### **Recommended Citation**

Kim, Jun Mo, "Multi-scale Simulation of Linear, Short-Chain Polyethylene Liquids under Flow Conditions. " PhD diss., University of Tennessee, 2010.  
[https://trace.tennessee.edu/utk\\_graddiss/713](https://trace.tennessee.edu/utk_graddiss/713)

This Dissertation is brought to you for free and open access by the Graduate School at TRACE: Tennessee Research and Creative Exchange. It has been accepted for inclusion in Doctoral Dissertations by an authorized administrator of TRACE: Tennessee Research and Creative Exchange. For more information, please contact [trace@utk.edu](mailto:trace@utk.edu).

To the Graduate Council:

I am submitting herewith a dissertation written by Jun Mo Kim entitled "Multi-scale Simulation of Linear, Short-Chain Polyethylene Liquids under Flow Conditions." I have examined the final electronic copy of this dissertation for form and content and recommend that it be accepted in partial fulfillment of the requirements for the degree of Doctor of Philosophy, with a major in Chemical Engineering.

Brian J. Edwards, Major Professor

We have read this dissertation and recommend its acceptance:

Bamin Khomami, David J. Keffer, Shanfeng Wang

Accepted for the Council:

Carolyn R. Hodges

Vice Provost and Dean of the Graduate School

(Original signatures are on file with official student records.)

To the Graduate Council:

I am submitting herewith a dissertation written by Jun Mo Kim entitled “*Multi-scale simulation of linear, short-chain polyethylene liquids under flow conditions.*” I have examined the final electronic copy of this dissertation for form and content and recommend that it be accepted in partial fulfillment of the requirements for the degree of Doctor of Philosophy, with a major in Chemical Engineering.

Brian J. Edwards, Major Professor

We have read this dissertation and recommend its acceptance:

Bamin Khomami

David J. Keffer

Shanfeng Wang

Accepted for the Council:

Carolyn R. Hodges  
Vice Provost and Dean of the Graduate School

(Original signatures are on file with official student records.)

**Multi-scale Simulation of Linear, Short-Chain Polyethylene  
Liquids under Flow Conditions**

A Dissertation Presented for the

Doctor of Philosophy Degree

The University of Tennessee, Knoxville

Jun Mo Kim

May 2010

## **Dedication**

I dedicate this Doctoral dissertation to my wife, Seri Son, my parents, Young Kun Kim, Yun Hee Choi, and my parents-in-law, Seung Byung Son, Sun Hee Doh, my sister, Yuri Kim, my brother-in-law Chang Hee Son, my grandmother, Sun Ran Oh, and my grandmother-in-law, Chae Min Park. I also wish to express my appreciation to my friend, Chunggi Baig for his endless support and encouragement during the course of my graduate study.

## Acknowledgements

I would like to thank my advisor Prof. Brian Edwards for his excellent guidance, endless encouragement, and invaluable advice during my Ph. D. study. I also appreciate Prof. David Keffer for his outstanding guidance in my initial Ph. D. study and his ideas in computer programming. I wish to thank Prof. Bamin Khomami for excellent teaching in his class and assistance in understanding the concept of Brownian dynamics simulations.

In the process of my studies, many people helped me on many aspects that are indispensable. I am thankful to Prof. Martin Kröger for his help in analyzing topological constraints, Dr. Kostas Daoulas for his advice in performing simulations of entangled systems, Dr. Vidya Venkataramani for her assistance in performing initial BD simulations and regarding the brightness distribution method, and Prof. Vlasios Mavrantzas for his support. Special thanks are given to Dr. Chunggi Baig for his endless support and encouragement, brilliant suggestions, and enormous help during my Ph. D. studies. I also appreciate Pavlos Stephanou for his help and discussion in developing the coarse-grained model and implementing the BD simulations. I would like to thank Prof. Shanfeng Wang, who kindly agreed to be on my committee. Finally, I deeply appreciate my wife and family for all the support that they provided to me during my Ph. D. studies.

## Abstract

The rheological and structural properties of polymeric liquids cannot be condensed within a single numerical model. They should be described within hierarchical, multi-level numerical models in which each sub-model is responsible for different time and length scales; atomistic, mesoscopic, and continuum. In this study, the rheological and structural properties of linear, short-chain polyethylene liquids were investigated from the classical atomistic level to the mesoscopic and continuum levels of description. At the atomistic level of description, nonequilibrium molecular dynamics (NEMD) simulations of linear, short-chain polyethylene liquids spanning from  $C_{16}H_{24}$  to  $C_{128}H_{256}$  were performed to advance our knowledge of fundamental characteristic of chain molecules under shear and planar elongational flow. Furthermore, entanglement characteristics, such as the shortest primitive path length, and the network configurations, were investigated as functions of strain rate in both vastly different flow fields using the topological Z-code. At the mesoscopic level of description, Brownian dynamics (BD) simulations of a freely-jointed chain with equivalent contour length to  $C_{78}H_{158}$  were carried out to compare single-chain dynamics in dense liquids (NEMD) and dilute solutions (BD) under shear flow. In addition, the macromolecular configurational diversity of individual chains in dense liquids and dilute solutions was explored using a brightness distribution method inspired by the rheo-optical investigation of DNA solutions. Based on these observations, a simple coarse-grained mesoscopic model for unentangled polymeric liquids and semi-dilute solutions was proposed and compared with NEMD simulation

data and experiments of semi-dilute DNA solutions under shear flow in terms of the rheological and structural properties, such as viscosity, normal stress coefficients, conformation tensor, and so on. Moreover, this model was further coarse-grained to the continuum level through pre-averaging and compared with NEMD simulation data to examine the relationships between different levels of description on the rheological and structural properties of unentangled polymeric materials under shear flow.



## Table of Contents

<b>Chapter I</b>	<b>Introduction</b>	1
<b>Chapter II</b>	<b>Background</b>	
2.1	The state of current modeling of polymeric liquids dynamics	4
2.2	Experimental methods on individual chain dynamics	6
2.3	Computer simulations of individual chain dynamics	8
<b>Chapter III</b>	<b>Simulation Methodology</b>	
3.1	Nonequilibrium molecular dynamics simulation	10
3.2	Brownian dynamics simulation of a bead-rod chain	19
3.3	Brownian dynamics simulation of a bead-spring chain	21
3.3.1	Model development	21
3.3.2	Bead-spring model	22
3.3.3	Mesoscopic level of description	24
3.3.4	Continuum level of description	28
3.3.5	Rheological and structural properties	31
3.4	Topological Z-code algorithm	32

3.5	Brightness distribution for configurations of chain molecules	34
-----	---	----

## **Chapter IV Results and discussion**

4.1	Rheological and entanglement characteristics of linear-chain polyethylene liquids in shear and planar elongational flows at the atomistic level using nonequilibrium molecular dynamics simulation	36
-----	--	----

4.2	Visualization of conformational changes of linear short-chain polyethylenes under shear and planar elongational flows	67
-----	---	----

4.3	Comparison of single chain dynamics at atomistic and mesoscopic level dynamics of the end-to-end vector	87
-----	---	----

4.4	A mean-field anisotropic diffusion model for unentangled polymeric liquids and semi-dilute solutions	129
-----	--	-----

<b>Chapter V</b>	<b>Summary and Conclusion</b>	<b>155</b>
------------------	-------------------------------	------------

<b>References</b>	<b>163</b>
-------------------	------------

<b>Vitae</b>	<b>173</b>
--------------	------------

## List of Tables

Table 3.1.1	State points of linear polyethylene chain liquids.	15
Table 3.1.2	The number of configurations for $C_{24}H_{50}$ , $C_{50}H_{102}$ , $C_{78}H_{158}$ , and $C_{128}H_{258}$ under shear flow and planar elongational flow (PEF).	18
Table 4.1.1	Shear viscosities $\eta$ as functions of dimensionless shear rate for $C_{50}H_{102}$ , $C_{78}H_{158}$ , and $C_{128}H_{258}$ .	39
Table 4.1.2	The mean-square, end-to-end distance of chains and the mean-square radius of gyration of chains as functions of dimensionless shear rate for $C_{50}H_{102}$ , $C_{78}H_{158}$ , and $C_{128}H_{258}$ .	41
Table 4.2.1	Statistical measures of polymer configurations for all four liquids at equilibrium, in shear, and in PEF.	72
Table 4.2.2	Topological characteristic quantities at equilibrium for each liquid: contour length, tube diameter, and number of entanglements.	73

## List of Figures

Fig. 3.4.1	Representative configuration classes of chain molecules as defined by the brightness distribution of Venkataramani <i>et al.</i> [Venkataramani <i>et al.</i> , 2008].	35
Fig. 4.1.1	Comparison of $\eta$ and $\eta_1$ for polyethylene melts as functions of strain rate.	38
Fig. 4.1.2	The mean-square chain end-to-end distance and the mean square chain radius of gyration for $C_{128}H_{258}$ under shear and PEF as functions of strain rate.	40
Fig. 4.1.3	Snapshots of molecular configurations under equilibrium (a), shear flow at the highest shear rate simulated, $\dot{\gamma}^* = 0.8$ (b), and PEF at the highest strain rate simulated, $\dot{\epsilon}^* = 0.2$ (c) for $C_{128}H_{258}$ .	43
Fig. 4.1.4	Comparison of mean pressure for polyethylene melts as a function of strain rate.	46
Fig. 4.1.5	The intermolecular LJ potential energy per united atom vs. strain rate.	47
Fig. 4.1.6	The bond-torsional energy per mode vs. the strain rate.	50
Fig. 4.1.7	The bond-stretching energy vs. the strain rate.	52
Fig. 4.1.8	The intramolecular LJ potential energy per (mode - 4) as a function of strain rate.	53
Fig. 4.1.9	The bond-bending energy per mode vs. the strain rate.	54

Fig. 4.1.10	Contour length of the primitive path vs. time after start-up of flow for $C_{78}H_{158}$ .	59
Fig. 4.1.11	Stationary values for primitive path vs. strain rate for $C_{24}H_{50}$ .	62
Fig. 4.1.12	Primitive path vs. molecular weight for various strain rates.	63
Fig. 4.1.13	'Number of entanglements' $Z_{coil}$ (assuming equilibrium statistics) vs. strain rate for $C_{24}H_{50}$ .	64
Fig. 4.1.14	Tube diameter (assuming equilibrium statistics) vs. strain rate for $C_{24}H_{50}$ .	65
Fig. 4.1.15	Tube diameter vs. molecular weight for various strain rates.	66
Fig. 4.2.1.	All chains of $C_{78}H_{158}$ at equilibrium (a), reduced shear rate of 0.8 (b), and elongation rate of 0.2 (c).	68
Fig. 4.2.2.	Ten random chains of $C_{24}H_{50}$ (a), $C_{50}H_{102}$ (b), $C_{78}H_{158}$ (c), and $C_{128}H_{258}$ (d) at equilibrium.	71
Fig. 4.2.3.	Ten random chains of $C_{24}H_{50}$ (a), $C_{50}H_{102}$ (b), $C_{78}H_{158}$ (c), and $C_{128}H_{258}$ (d) at a reduced shear rate of 0.8.	75
Fig. 4.2.4.	Ten random chains of $C_{24}H_{50}$ (a), $C_{50}H_{102}$ (b), $C_{78}H_{158}$ (c), and $C_{128}H_{258}$ (d) at reduced shear rate of 0.2.	77
Fig. 4.2.5.	Conformation tensor components of $C_{24}H_{50}$ , $C_{50}H_{102}$ , $C_{78}H_{158}$ , and $C_{128}H_{258}$ under shear (left column) and PEF (right column).	79
Fig. 4.2.6.	Snapshots of the molecular structure under shear (upper row) and PEF (bottom row) and the corresponding distribution functions as determined by the Eigenvalues and Eigenvectors of the conformation tensor.	81

Fig. 4.2.7.	Projections of atomistic chain structure of $C_{128}H_{258}$ onto shortest primitive path.	82
Fig. 4.2.8.	Snapshots of the $C_{50}H_{102}$ liquid undergoing shear at a reduced shear rate of 0.8.	85
Fig. 4.2.9.	Snapshots of the $C_{50}H_{102}$ liquid undergoing PEF at a reduced strain rate of 0.2.	86
Fig. 4.3.1.	The mean-square chain end-to-end distance for $C_{78}H_{158}$ as a function of $Wi$ from the atomistic NEMD (open symbols) and BD (filled symbols) simulations.	89
Fig. 4.3.2.	The intermolecular and intramolecular Lennard-Jones potential energies as functions of $Wi$ .	94
Fig. 4.3.3.	Probability distributions of magnitude of end-to-end vector for the five values of $Wi$ designated by the vertical lines in Figure 4.3.1. as calculated in the NEMD (4.3.3a) and BD (4.3.3b) simulations.	98
Fig. 4.3.4.	The magnitude of end-to-end vector and the orientation angle with respect to the flow direction, $\theta$ , as functions of time for a random chain of the NEMD (4.3.4a) and BD (4.3.4b) simulations.	105
Fig. 4.3.5.	The $xx$ component of radius of gyration of a random single chain as a function of time.	107
Fig. 4.3.6.	Probability distribution of positive and negative end-to-end vector orientation in the dense liquids (NEMD simulations) at four values of $Wi$ .	108

Fig. 4.3.7.	Probability distribution of representative chain configuration classes in the dense liquids (NEMD simulations) at four values of $Wi$ .	111
Fig. 4.3.8.	Probability distribution of molecules within the three regions of $ R_{ete} $ defined in the text for the dense liquids (NEMD simulations).	114
Fig. 4.3.9.	Time cross-correlation functions versus observation time for three values of $Wi$ (4.3.8a), and the power spectral density (4.3.8b) versus frequency for two values of $Wi$ that exhibit minima in the cross-correlation function curves in the dense liquid simulations.	116
Fig. 4.3.10.	Characteristic timescales versus $Wi$ .	118
Fig. 4.3.11.	Log-log plots of the characteristic timescales, relative to the Rouse time, versus $Wi$ for the NEMD (open symbols) and BD (filled symbols) simulations.	126
Fig. 4.4.1.	The mean-square end-to-end distance as a function of $Wi$ .	130
Fig. 4.4.2.	The steady shear viscosity vs. $Wi$ .	132
Fig. 4.4.3.	The normal stress coefficients as functions of $Wi$ .	135
Fig. 4.4.4.	Comparison of the shear stress computed from models with experimental results of semi-dilute DNA solutions as a function of $Wi$ .	136

Fig. 4.4.5.	The orientation angle of the mesoscopic model as a function of $Wi$ . The inset of this figure displays the orientation angle at $\alpha = 0.6$ vs. $Wi$ in log-log plot.	138
Fig. 4.4.6.	Molecular configuration thickness in the mesoscopic model as a function of $Wi$ .	140
Fig. 4.4.7.	The mean molecular extension in the mesoscopic model vs. $Wi$ . The inset of this figure is the mean fractional extension vs. $Wi$ .	141
Fig. 4.4.8.	The non-zero components of the conformation tensor as a function of $Wi$ .	144
Fig. 4.4.9.	Same probability distribution functions of a bead-rod chain vs. $ \mathbf{R}_{ete} $ at five values of $Wi$ with different bin sizes.	146
Fig. 4.4.10.	The probability distribution of the NEMD simulations and the mesoscopic model vs. $ \mathbf{R}_{ete} $ .	148
Fig. 4.4.11.	The time correlation functions of the $xx$ component of the end-to-end vector vs. observation time at $Wi = 0.1$ and $Wi = 1000$ .	150
Fig. 4.4.12.	The characteristic time scale, $\tau_{xx}$ , as a function of $Wi$ .	154



## Chapter I Introduction

Most of the day-to-day products present in the contemporary lifestyle, such as clothing, communication devices, computers, medical instruments, coatings and huge number of other crucial applications, are made by processing molten polymeric materials under flow conditions. In order to obtain the final products, the polymeric materials undergo numerous processes under various flow conditions. Hence, understanding the rheological and microstructural behavior of polymeric liquids in flowing systems is important in the polymer processing industry and for advancing the state of knowledge concerning the fundamental characteristics of chain molecules under flow. However, the rich rheological and structural characteristics displayed by polymeric liquids are too complex to be described by a single constitutive model. They need to be described using hierarchical, multi-level models in which each sub-model is responsible for different time and length scales: atomistic, mesoscopic, and continuum. In this study, the rheological and structural properties of linear, short-chain polyethylene liquids are investigated starting with a classical atomistic potential model and then coarse graining to the mesoscopic level, and then to a macroscopic continuum model.

At the atomistic level of description, nonequilibrium molecular dynamics (NEMD) simulations of linear, short-chain polyethylene liquids spanning from  $C_{24}H_{50}$  to  $C_{128}H_{256}$  can be used to advance our knowledge of the fundamental characteristics of chain molecules under shear and planar elongational flows (PEF). In addition, to

obtain direct evidence regarding the effect of standard flows on chain configurations, visualizations of the molecular structure of linear, short-chain polyethylene liquids under flow conditions can be simulated and compared with their equilibrium static structures. These graphics provide a structural understanding of the various statistical measures that are used in the literature to characterize the changes in chain configuration as a function of strain rate and chain length, and allow a visualization of the inherent chain dynamics and orientation induced by shear and elongational flows. Furthermore, entanglement characteristics can also be investigated as functions of strain rate in both shear and PEF. For examples, it is quite instructive from a rheological point of view to determine how the entanglement number, shortest primitive path length, etc., correlate with the rheological quantities in these vastly different flow fields.

The observations of the motions of individual chain molecules are crucial to further development and refinement of rheological and topological models of the dynamics of polymeric liquids. For example, the individual chains tumble and rotate under shear flow, but on average they are aligned with respect to the flow direction. However, most past modeling efforts have been aimed at the description of the evolution of bulk-averaged quantities, such as the conformation or stress tensors, under the influence of an applied external flow field [Bird *et al.*, 1987a]. Hence, at the mesoscopic level of description, Brownian dynamics (BD) simulations of a freely-jointed chain with equivalent contour length to that simulated at the atomistic level can be used to compare single-chain dynamics in dense liquids (atomistic NEMD) and

dilute solutions (coarse-grained BD) under shear flow. In addition, the macromolecular configurational diversity of single chains in dense liquids and dilute solutions can also be explored using a brightness distribution method inspired by the rheo-optical investigation of DNA solutions.

Based on observations at the atomistic and mesoscopic levels of description, it is possible to derive a mean-field mesoscopic model to mimic the anisotropic diffusive motion of an arbitrary chain within the confines of tube-like structures that are formed by the surrounding stretched chains at high  $Wi$ . Herein, such a model is derived using a bead-spring chain with a finitely-extensible nonlinear elastic (FENE) force law for each spring and an anisotropic diffusion tensor. BD simulations are used to examine the model's behavior under shear flow. Moreover, this model is further coarse-grained to the continuum level through pre-averaging and compared with NEMD simulation data to examine the relationships between different levels of description on the rheological and structural properties of unentangled polymeric materials under shear flow.

## Chapter II Background

### 2.1 The state of current modeling of polymeric liquids dynamics

The most fundamental theoretical tool for understanding polymer dynamics is an atomistic model of a polymer chain based on inter-chain and intra-chain force fields between atomistic units. However, this tool has not been exploited to any significant degree in this field for two reasons; 1) accurate atomistic models are few and not very well developed yet, except for a few simple homopolymers such as polyethylene; and 2) computational requirements are severe to examine polymeric systems of entangled chains, but only relatively short-chain, unentangled liquids.

To overcome the limitations of the atomistic models of polymer chains, the coarse-graining procedure has been used in modeling of polymeric liquids [Müller-Plathe, 2002]. In coarse-graining, the degrees of freedom of an atomistic model are decreased by replacing them with interactions at the super-atom level. In other words, the order of ten atoms or a small chemical repeat unit in the atomistic model was substituted by a super-atom that describes the dynamics of the collective unit. Although huge progress has been made during recent years in linking the atomistic level of description to the coarse-grained atomistic level of description systematically [Harmandaris *et al.*, 2006], more accurate relationships between atomistic models and coarse-grained mesoscopic models are needed for describing more entangled and complex structures of polymeric liquids.

At the mesoscopic level of description, polymeric liquids have been described by Brownian dynamics simulation of bead-rod, bead-spring models, and dumbbells [Bird *et al.*, 1987b]. A polymer chain at the atomistic level is coarse-grained as a bead-rod chain by elimination of degrees of freedom associated with segmental motion that do not change within the time window of interest. These stiff segments are modeled as rods which have the length of a Kuhn step. This model can be further coarse-grained to a bead-spring chain with various spring force laws, such as Hookean spring, finitely extensible nonlinear elastic (FENE) spring and so on, not only to reduce computations requirements but also to extract useful information hiding behind the complexity of polymeric liquids. The bead-spring chain can also be further coarse-grained to a simple dumbbell model at the macroscopic level of description for the most coarse-grained system description.

Brownian dynamics simulations of polymeric liquids under flow conditions have been developed by Liu (1989), Zylka and Ottinger (1989), Grassia and Hinch (1996), and Doyle *et al.* (1997), among many others. These models at the mesoscopic level of description show numerous successes in describing the behavior of polymeric liquids under flow conditions. However, any information that is present on microscopic timescales is effectively removed from the final evolution equations due to subsequent approximations, such as pre-averaging. Moreover, Brownian simulations seem to be restricted to a concentrations of a few  $c^*$ , at most semi-dilute solutions [Dambal *et al.*, 2009], where  $c^*$  is defined by a concentration at which polymer coils start to overlap.

Most of the continuum models of polymeric liquids have been developed from configurational distribution functions using pre-averaging [Bird *et al.*, 1987b; Beris and Edwards, 1994]. These pre-averaged models are easy to solve using the typical numerical techniques, and are applicable to chain liquids at low field strength. However, their descriptions of the rheological behavior of polymer chains tend to break down once the field strength drives the fluid beyond the linear viscoelastic regime.

## **2.2 Experimental methods on individual chain dynamics**

Until recently, light scattering and birefringence experiments [Fuller, 1995] were used for analyzing the orientational and configurational changes of polymer chains undergoing flow. However, these types of experimentation were unable to track configurational changes of individual polymer chains. Consequently, these measurement techniques were restricted to examining bulk fluid properties, and cannot distinguish between phenomena that occur over disparate timescales; however, this does not mean that the dynamics of individual chain molecules do not affect the observed birefringence and light scattering patterns.

Relatively recent direct visualization of individual polymer chains using video microscopy offers the possibility to explore the motions of individual chain molecules undergoing flow [Teixeira *et al.*, 2005, 2007; Smith and Chu, 1998; Smith *et al.*, 1999; LeDuc *et al.*, 1999; Schroeder *et al.*, 2005; Robertson and Smith, 2007]. These initial

studies have seriously called into question many of the assumptions used to model polymer flow dynamics. Smith *et al.* [Smith *et al.*,1999] and LeDuc *et al.* [LeDuc *et al.*, 1999] simultaneously examined dilute solutions of DNA, in which the dynamics of individual, labeled chains were visualized under shear in the flow-vorticity plane using video microscopy. These results demonstrated that the flexible polymer chains experienced both deformation and tumbling under shear, as functions of the Weissenberg number ( $Wi = \tau_R \dot{\gamma}$ ). Schroeder *et al.* [Schroeder *et al.*, 2005] and Teixeira *et al.* [Teixiera *et al.*, 2005, 2007] visualized and tracked individual configurational changes of fluorescently-labeled DNA solutions under steady shear flow in the flow-gradient plane for concentrations ranging from dilute to highly entangled. These experiments again demonstrated the tumbling and stretching dynamics of individual chains, which depended on both  $Wi$  and concentration, but the evidence was more direct since the visualization was carried out in the flow-gradient plane. They also demonstrated a clear *quasi-periodic* tumbling of the individual DNA molecules in dilute solution at high  $Wi$ , with a characteristic frequency for this rotation that scaled sublinearly with shear rate as  $Wi^{0.62}$ . For concentrated DNA solutions, two distinct timescales were observed: the first associated with the chain retraction dynamics (the short timescale), and the second possibly related to the dynamics of constraint release and contour length fluctuations (the long timescale). The probability distribution of chain extension broadened dramatically at high  $Wi$  from its approximately Gaussian shape at low  $Wi$ , which is not typical of pre-averaged bulk rheological theory. Robertson and Smith (2007) used optical tweezers to measure the

intermolecular forces acting on a single DNA chain as exerted by the surrounding entangled molecules, and found three distinct timescales: the short timescale was determined as close to the theoretical value of the Rouse time, the long timescale was associated with the disengagement time of reptation theory, and the intermediate timescale was speculated to be a second reptative process that was correlated with the dynamics of the effective reptation tube under shear.

Despite the numerous successes of single-chain microscopy to date, experimentation alone cannot resolve all of the outstanding issues that perplex rheologists at high  $Wi$ . The primary limitation of these experiments is the small number of molecules that can be effectively tracked simultaneously, which is especially true of dense polymer melts. A further limitation lies in the small number of flow geometries that lend themselves to direct visualization; even in steady shear flow, it is difficult to view all flow planes within the sample using the same apparatus.

### **2.3 Computer simulations of individual chain dynamics**

Atomistic simulation of polymeric liquids offers a complementary perspective of chain dynamics under flow. Most nonequilibrium flow simulations to date have focused on the bulk rheological and structural properties of both atomistic [Moore *et al.*, 2000; Baig *et al.*, 2006b; Mavrantzas and Theodorou, 1998; Mavrantzas and Öttinger, 2002; Todd and Daivis, 1998] and coarse-grained (bead-rod and bead-spring chains) [Kröger *et al.*, 1993; Kröger and Hess, 2000; Öttinger, 1996; Doyle *et al.*,



1997; Venkataramani *et al.*, 2008] liquids. Although much new insight has been garnered from these studies, possibly this focus on bulk behavior at macroscopic length and time scales has resulted in overlooking key microscopic information concerning the molecular-scale origin of the bulk rheological and structural properties. Indeed, it has sometimes led to inadequate explanations of observed bulk-scale phenomena [Kim *et al.* (2009)], as described below.

The primary advantage of simulation over experiment is that every chain within the sample can be examined individually, not only those which were optically labeled and under view in the experimental apparatus. This allows much more detailed information to be gleaned from the simulation with respect to the experiment, as statistically meaningful correlations can be established via averaging of the dynamical behavior of each individual chain. Also, simulations are readily amenable to topological analysis, extending equilibrium properties such as tube diameter, primitive path length, and number of entanglements to nonequilibrium flow situations. Certainly, bulk-averaged properties, such as the conformation tensor, can still be calculated, but now with the ability to examine the effects of short timescale individual chain dynamics upon them. Ultimately, more and better information at the microscopic scale should lead to better rheological and structural models of polymeric liquids under flow.

## Chapter III Simulation Methodology

### 3.1 Nonequilibrium molecular dynamics simulation

The *NVT* NEMD simulations of the atomistic dense polyethylene liquids were carried out using the *p*-SLLOD equations of motion [Edwards and Dressler, 2001] with the Nosé-Hoover thermostat [Evans and Morriss, 1990] for arbitrary homogeneous flows. These equations of motion with the Nosé-Hoover thermostat are

$$\begin{aligned}\dot{\mathbf{q}}_{ia} &= \frac{\mathbf{p}_{ia}}{m_{ia}} + \mathbf{q}_{ia} \cdot \nabla \mathbf{u} \ , \\ \dot{\mathbf{p}}_{ia} &= \mathbf{F}_{ia} - \mathbf{p}_{ia} \cdot \nabla \mathbf{u} - m_{ia} \mathbf{q}_{ia} \cdot \nabla \mathbf{u} \cdot \nabla \mathbf{u} - \zeta \mathbf{p}_{ia} \ .\end{aligned}\tag{1}$$

In these equations,  $m_{ia}$  is the mass of a<sup>th</sup> atom in  $i^{\text{th}}$  molecule. The  $\mathbf{p}_{ia}$ ,  $\mathbf{q}_{ia}$ , and  $\mathbf{F}_{ia}$  are the momentum, position, and force vector of a<sup>th</sup> atom in  $i^{\text{th}}$  molecule, respectively. The  $\nabla \mathbf{u}$  is the velocity gradient tensor. (For a recent discussion of the relative merits of the SLLOD and *p*-SLLOD algorithms, see Refs. [Edwards *et al.*, 2005, 2006; Daivis and Todd, 2006]. In shear flow, the *p*-SLLOD equations of motion are identical to the SLLOD equations of motion [Edwards and Dressler, 2001] because the term  $m_{ia} \mathbf{q}_{ia} \cdot \nabla \mathbf{u} \cdot \nabla \mathbf{u}$  vanishes since

$$\nabla \mathbf{u} = \begin{pmatrix} 0 & 0 & 0 \\ \dot{\gamma} & 0 & 0 \\ 0 & 0 & 0 \end{pmatrix} \ ,\tag{2}$$

where  $\dot{\gamma}$  is the applied shear rate. For planar elongational flow,

$$\nabla \mathbf{u} = \begin{pmatrix} \dot{\varepsilon} & 0 & 0 \\ 0 & -\dot{\varepsilon} & 0 \\ 0 & 0 & 0 \end{pmatrix}, \quad (3)$$

where  $\dot{\varepsilon}$  is the applied elongational strain rate. The other terms appearing in Eq. (1) are defined as

$$\begin{aligned} \dot{\zeta} &= \frac{P_\zeta}{Q}, \\ \dot{P}_\zeta &= \sum_i \sum_a \frac{\mathbf{p}_{ia}^2}{m_{ia}} - DNk_B T, \\ Q &= DNk_B T \tau^2. \end{aligned} \quad (4)$$

The  $N$ ,  $V$ , and  $T$  are total number of atoms, volume of system, and absolute temperature, respectively. The  $k_B$  and  $D$  denote the Boltzmann constant and the dimensionality of the system, respectively. The  $\zeta$  and  $p_\zeta$  represent the coordinate- and momentum-like variables of the Nosé-Hoover thermostat. The  $Q$  represents the inertia mass of the Nosé-Hoover thermostat, which depends on a characteristic time scale of the system,  $\tau$ .

For PEF, we applied the Kraynik-Reinelt Boundary Condition (KRBC) [Kraynik and Reinelt, 1992]. From prior studies [Todd and Daivis, 2000; Baig *et al.*, 2005b], the Hencky strain value was set at  $\varepsilon_p \approx 0.9624$ , the initial orientation angle of

the simulation box was chosen as  $\theta_0 = 31.718^\circ$ , and the time period for the KRBC application,  $t_p$ , was determined from  $\varepsilon_p = \dot{\varepsilon} t_p$ .

The  $p$ -SLLOD equations of motion with the Nosé-Hoover thermostat were integrated using the reversible Reference System Propagator Algorithm ( $r$ -RESPA) with two time scales, as developed by Tuckerman *et al.* (1992) and applied by Cui. *et al.* (1996). The long time scale was 2.35fs under shear flow and 2.26fs under PEF, which was used for the intermolecular interactions. In general, the short time scale was 0.235 under shear and 0.226fs under PEF, which was used for intramolecular interactions such as bond-stretching, bond-bending, and bond-torsional interactions. However, we used 0.452fs as a short time scale for  $C_{50}H_{102}$ ,  $C_{78}H_{158}$ , and  $C_{128}H_{258}$  under shear flow.

In previous work on elongational flow [Baig *et al.*, 2005b, 2006b], the Siepman-Karaboni-Smit (SKS) united-atom model for linear alkanes [Siepman *et al.*, 1993] was applied to shear and PEF. However, the rigid bond between adjacent atoms in the original model was replaced with a harmonic potential function to relieve issues related to stiff integrations at small timescales, as described below. For the intramolecular atomic interactions, the LJ potential was assumed:

$$V_{LJ}(r) = 4\varepsilon_{ij} \left[ \left( \frac{\sigma_{ij}}{r} \right)^{12} - \left( \frac{\sigma_{ij}}{r} \right)^6 \right] . \quad (5)$$

Only atoms that were separated by more than three bonds were considered for the intramolecular LJ interaction energy. A cut-off distance,  $r_c$ , of  $2.5\sigma_{CH_2}$  (9.825 Å)

was employed for the LJ potential, beyond which the potential energy was assumed to vanish. (Neither a shift of the LJ potential nor a finite-size correction employing the pair correlation function would have effects of practical importance on the results for the LJ energy and pressure contributions, to be presented below.) The parameters  $\varepsilon_{CH_2}/k_B$  and  $\varepsilon_{CH_3}/k_B$  were 47K and 114K, respectively. The parameters  $\sigma_{CH_2}$  and  $\sigma_{CH_3}$  were 3.93 Å each. The parameters  $\varepsilon_{ij}$  and  $\sigma_{ij}$  were estimated using Berthelot mixing rules through the expressions

$$\varepsilon_{ij} = (\varepsilon_i \varepsilon_j)^{1/2}, \quad \sigma_{ij} = (\sigma_i + \sigma_j)/2 \quad . \quad (6)$$

The bond-stretching interaction is governed by harmonic potential function,

$$V_{str}(l) = \frac{1}{2} k_{str} (l - l_{eq})^2 \quad , \quad (7)$$

where the equilibrium length was  $l_{eq} = 1.54 \text{ \AA}$  and the bond-stretching constant was  $k_{str}/k_B = 452,900 \text{ K/\AA}^2$ . The bond-bending interaction was described by a harmonic potential,

$$V_{ben}(\theta) = \frac{1}{2} k_{ben} (\theta - \theta_{eq})^2 \quad . \quad (8)$$

The equilibrium angle in this expression was  $\theta_{eq} = 114^\circ$ , and the bond-bending constant was  $k_{ben}/k_B = 62,500 \text{ K/rad}^2$ . The bond-torsional interaction was

$$V_{tor}(\phi) = \sum_{m=0}^3 a_m (\cos \phi)^m \quad . \quad (9)$$

This function was developed by Jorgensen *et al.* (1984). The parameters  $a_0/k_B$ ,  $a_1/k_B$ ,  $a_2/k_B$ , and  $a_3/k_B$  in this equation are 1010 K, 2019 K, 136.4 K, and 3165 K, respectively.

The state points of the simulated liquids are summarized in Table 3.1.1. The characteristic properties of these liquids, such as density, temperature, and relaxation (Rouse) time, are essentially the same as in the previous studies of PEF [Baig *et al.*, 2005b, 2006b]. The densities of each alkane are  $\rho = 0.7728 \text{ g/cm}^3$  for  $\text{C}_{24}\text{H}_{50}$ ,  $\rho = 0.7426 \text{ g/cm}^3$  for  $\text{C}_{50}\text{H}_{102}$ ,  $\rho = 0.7640 \text{ g/cm}^3$  for  $\text{C}_{78}\text{H}_{158}$ , and  $\rho = 0.7754 \text{ g/cm}^3$  for  $\text{C}_{128}\text{H}_{258}$ . The simulations were conducted at the temperature of 450K, with the exception of  $\text{C}_{24}\text{H}_{50}$ , which was conducted at 333K under both shear and PEF. From the previous studies [Baig *et al.*, 2005b, 2006], the longest rotational relaxation time was 617ps for  $\text{C}_{24}\text{H}_{50}$ , 500ps for  $\text{C}_{50}\text{H}_{102}$ , 1,450ps for  $\text{C}_{78}\text{H}_{158}$ , and 5,500ps for  $\text{C}_{128}\text{H}_{258}$ . (Later, it was determined that the longest rotational relaxation time was 2,300ps for  $\text{C}_{78}\text{H}_{158}$  using the KWW method [Williams and Watts, 1970; Williams *et al.*, 1971; Tsolou and Mavrantzas, 2005; Deschenes and Vanden Bout, 2001]. Here, we retain the previous relaxation time of  $\text{C}_{78}\text{H}_{158}$  for internal consistency.)

The fully-stretched chain lengths, with respect to all bond torsion angles assuming the *trans*-conformation, were 29.7Å for  $\text{C}_{24}\text{H}_{50}$ , 63.3Å for  $\text{C}_{50}\text{H}_{102}$ , 99.4Å for  $\text{C}_{78}\text{H}_{158}$ , and 164Å for  $\text{C}_{128}\text{H}_{258}$ . This length is very important to consider when setting the box length in the flow direction. A cubic box was used for  $\text{C}_{24}\text{H}_{50}$  since this chain length was fairly small. For the other chain lengths, however, non-cubic boxes with the long axes of the boxes in the direction of flow were used and such

TABLE 3.1.1. State points of linear polyethylene chain liquids. (Here, we retain the previous relaxation time of  $C_{78}H_{158}$  for internal consistency.)

Polymer		$C_{24}H_{50}$	$C_{50}H_{102}$	$C_{78}H_{158}$	$C_{128}H_{258}$
Temperature (K)		333	450	450	450
Density ( $g/cm^3$ )		0.7728	0.7426	0.7640	0.7754
Longest rotational relaxation time (ps)		617	500	1450	5500
P	No. of molecules	100	96	192	416
	No. of interaction sites	2,400	4,800	14,976	53,248
	E X	41.72	65.45	100.50	166.00
F	Box length ( $\text{\AA}$ )	Y	41.72	65.45	100.50
		Z	41.72	35.18	45.20
P	No. of molecules	100	120	160	256
	No. of interaction sites	2,400	6,000	12,480	32,768
	C X	41.72	93.02	130.50	212.70
F	Box length( $\text{\AA}$ )	Y	41.72	45.00	54.00
		Z	41.72	45.00	54.00

long axes were approximately 10% longer than the fully-stretched length of each chain. As discussed previously [Baig *et al.*, 2006b], this was necessary to avoid artificially induced system-size effects, which could be introduced by periodicity issues associated with any given chain being stretched out of both ends of the simulation box. In the two directions perpendicular to the direction of flow, there was no need to use an extended box dimension; consequently, the orthogonal axes of the simulation box are much shorter than the long axes to reduce the computational requirements of the simulations.

For shear flow, the simulated ranges for dimensionless shear rates  $\dot{\gamma}^* \equiv \dot{\gamma} t_{ref}$  with  $t_{ref} = (m\sigma^2 / \varepsilon)^{1/2}$  were  $0.0005 \leq \dot{\gamma}^* \leq 1.0$  for  $C_{24}H_{50}$ ,  $0.001 \leq \dot{\gamma}^* \leq 1.0$  for  $C_{50}H_{102}$ ,  $0.0002 \leq \dot{\gamma}^* \leq 1.0$  for  $C_{78}H_{158}$ , and  $0.0001 \leq \dot{\gamma}^* \leq 1.0$  for  $C_{128}H_{258}$ . For PEF, the equivalent ranges for  $\dot{\varepsilon}^* \equiv \dot{\varepsilon} t_{ref}$  were  $0.0005 \leq \dot{\varepsilon}^* \leq 1.0$  for  $C_{24}H_{50}$ ,  $0.001 \leq \dot{\varepsilon}^* \leq 0.2$  for  $C_{50}H_{102}$ ,  $0.0002 \leq \dot{\varepsilon}^* \leq 0.2$  for  $C_{78}H_{158}$ , and  $0.0001 \leq \dot{\varepsilon}^* \leq 0.2$  for  $C_{128}H_{258}$ .

The rheological characteristic functions of the liquids were calculated using standard procedures in NEMD simulations [Evans and Morriss, 1990]. For homogeneous systems, the microscopic expression of the pressure tensor,  $\Pi$ , which was developed by Irving and Kirkwood (1984), is

$$\Pi = \left\langle \frac{1}{V} \sum_i \sum_a \left( \frac{\mathbf{p}_{ia} \mathbf{p}_{ia}}{m_{ia}} + \mathbf{q}_{ia} \mathbf{F}_{ia} \right) \right\rangle . \quad (10)$$

The viscous stress tensor is defined in terms of the pressure tensor  $\Pi$  as



$$\boldsymbol{\sigma} = \Pi - p\boldsymbol{\delta}. \quad (11)$$

Here,  $p$  is the thermodynamic pressure, and  $\boldsymbol{\delta}$  is the unit tensor. The mean pressure,  $(\text{tr}\Pi)/3$ , is equal to the hydrostatic pressure when  $\boldsymbol{\sigma}$  vanishes [Aris, 1986]. The shear viscosity is defined as

$$\eta = -\frac{\sigma_{xy}}{\dot{\gamma}}, \quad (12)$$

where  $x$  is the direction of flow and  $y$  is the gradient direction. Similarly, the first elongational viscosity and the second elongational viscosity are defined as

$$\eta_1 = \frac{\sigma_{yy} - \sigma_{xx}}{4\dot{\epsilon}}, \quad \eta_2 = \frac{\sigma_{yy} - \sigma_{zz}}{2\dot{\epsilon}}. \quad (13)$$

Here,  $x$  is the extension direction,  $y$  is the compression direction, and  $z$  is the neutral direction.

In order to examine the entanglement properties of these polyethylene liquids, both steady-state and transient system configurations at various strain rates and time values were obtained—see Table 3.1.2. For steady-state properties, configurational data were collected after steady state had been achieved, with each configuration approximately one Rouse time apart, so as to ensure configurational independence. The only exception to this rule was for  $\text{C}_{128}\text{H}_{258}$ , where computational requirements limited us to obtaining configuration only every 0.1 Rouse times. Enough configurations were stored to generate average quantities with reasonable statistical uncertainties. Except for  $\text{C}_{24}\text{H}_{50}$ , configurations at four strain rate values for all liquids in both shear and PEF were collected. In all cases, the first strain rate value was always the equilibrium case. The other three values lay within the nonlinear

TABLE 3.1.2. The number of configurations for  $C_{24}H_{50}$ ,  $C_{50}H_{102}$ ,  $C_{78}H_{158}$ , and  $C_{128}H_{258}$  under planar Couette flow and planar elongational flow. Dimensionless strain rates are given in LJ units, introduced before Eq. (10).

0.2		30		50							
		$C_{24}H_{50}$		$C_{50}H_{102}$		$C_{78}H_{158}$		$C_{128}H_{258}$			
0.5		30									
Strain	No. of configs	Strain	No. of configs	Strain	No. of configs	Strain	No. of configs	Strain	No. of configs		
0.8	50										
rate	rate		rate		rate		rate		rate		
(LJu)	Shear	PEF	(LJu)	Shear	PEF	(LJu)	Shear	PEF	(LJu)	Shear	PEF
0	50	--	0	50	--	0	49	--	0	20	--
0.004	50	50	0.004	50	50	0.001	50	38	0.0004	21	10
0.01	30	30	0.08	50	50	0.08	50	40	0.08	21	16
0.02	30	30	0.2		50	0.2		20	0.2		17
0.04	30	30	0.8	50		0.8	44		0.8	19	
0.05	30										
0.08	50	50									
0.1	30										

(strain-rate thinning) viscosity region, as determined from the known Rouse times of these liquids [Baig *et al.*, 2005b, 2006b]: 617ps for C<sub>24</sub>H<sub>50</sub>, 500ps for C<sub>50</sub>H<sub>102</sub>, 1,450ps for C<sub>78</sub>H<sub>158</sub>, and 5,500ps for C<sub>128</sub>H<sub>258</sub>. (Note that the Rouse time for C<sub>24</sub>H<sub>50</sub> is out of proportion with those of the longer-chain liquids due to the fact that it was simulated at the lower temperature of 333K versus 450K, as mentioned earlier, since C<sub>24</sub>H<sub>50</sub> is a vapor at 450K.) For each liquid, the critical shear rate for the onset of shear-thinning behavior occurs near to the reciprocal of the Rouse time. The specific values of strain rate examined for each liquid under both shear and PEF are tabulated in Table 3.1.2. Additionally, 1000 configurations were produced under start-up conditions for C<sub>24</sub>H<sub>50</sub> and C<sub>78</sub>H<sub>158</sub> under shear and PEF at their highest dimensionless strain rate values to analyze the transient behavior. The configurations of C<sub>24</sub>H<sub>50</sub> were saved in 2.352ps intervals. For C<sub>78</sub>H<sub>158</sub>, the configurations were saved every 1.176ps under shear and 0.294ps under PEF.

### 3.2 Brownian dynamics simulation of a bead-rod chain

The atomistic system was coarse-grained to a bead-rod chain with the same contour length and relaxation time as the atomistic systems. Usually such a procedure is accomplished by setting the rod length equal to the Kuhn length, which is  $k \equiv \langle R_{ete}^2 \rangle / R_{max}$ . In this case, this amounts to about 15 Å. However, given the rotational characteristic of the PE chains to be discussed shortly, this rod length was determined to be too long to capture the rotational dynamics at high  $Wi$ . Therefore

we chose a rod length of  $4.5 \text{ \AA}$  using  $\langle R_{ete}^2 \rangle^{1/2} / \sqrt{n}$  so that 23 rods and 24 beads quantified the proper chain length of  $99.45 \text{ \AA}$ . This corresponds to an infinitely dilute (free-draining) polymer solution at its theta point. Our purpose, then, is to compare the dense liquid chain dynamics to those of a freely-draining chain in the absence of neighboring chains.

The Brownian dynamics (BD) simulations of the coarse-grained, bead-rod chain liquids were carried out under shear flow to assess the differences between individual molecular dynamics in dense liquids as opposed to dilute solutions. In these simulations, there were three external forces acting on the beads, which satisfy the equation

$$\mathbf{F}_i^H + \mathbf{F}_i^C + \mathbf{F}_i^B = 0, \quad i = 1, 2, \dots, N_k \quad . \quad (14)$$

The  $\mathbf{F}_i^H$ ,  $\mathbf{F}_i^C$ , and  $\mathbf{F}_i^B$  represent the hydrodynamic drag force, the constraint force, and the Brownian force at the  $i$ -th bead, respectively. The hydrodynamic drag force is described by Stokesian drag acting on the beads,

$$\mathbf{F}_i^H = -\zeta (\dot{\mathbf{r}}_i - \mathbf{v}_i^\infty) \quad , \quad (15)$$

where the  $\zeta$  denotes the drag coefficient. The  $\dot{\mathbf{r}}_i$  and  $\mathbf{v}_i^\infty$  are the velocity of the bead and streaming velocity profile at bead  $i$ , respectively. The constraint force that maintains constant bond length ( $a$ ) between adjacent beads is

$$\begin{aligned}\mathbf{F}_i^C &= T_i \mathbf{u}_i - T_{i-1} \mathbf{u}_{i-1} \quad , \\ \mathbf{u}_i &= (\mathbf{r}_{i+1} - \mathbf{r}_i) / a \quad .\end{aligned}\tag{16}$$

The  $T_i$  represents tension between the beads and the  $\mathbf{u}_i$  refers to the orientation of rod  $i$ . The Brownian force that describes collisions between neighboring beads is

$$\begin{aligned}\langle \mathbf{F}_i^B(t) \rangle &= 0 \quad , \\ \langle \mathbf{F}_i^B(t) \mathbf{F}_j^B(t + \Delta t) \rangle &= 2k_B T \zeta \delta_{ij} \delta(\Delta t) \approx \frac{2k_B T \zeta \delta_{ij}}{\Delta t} \quad .\end{aligned}\tag{17}$$

The  $\delta$  represents the Dirac delta function and the  $\delta_{ij}$  refers to the unit tensor.

The set of evolution equations for the position vectors of beads are obtained by combining Eqs. (15), (16), (17) with (14), and integration subject to the constraints

$$d\mathbf{r}_i = \left[ \mathbf{v}_i^\infty + \frac{\mathbf{F}_i^C}{\zeta} \right] dt + \sqrt{\frac{2k_B T}{\zeta}} d\mathbf{W}_i, \quad i = 1, 2, \dots, N_k \quad ,\tag{18}$$

$$(\mathbf{r}_{i+1} - \mathbf{r}_i) \cdot (\mathbf{r}_{i+1} - \mathbf{r}_i) - a^2 = \phi^2, \quad i = 1, 2, \dots, N_k - 1 \quad ,$$

using the iterative technique developed by Liu (1989). The  $d\mathbf{W}_i$  is a Wiener process and the  $\phi^2$  is the specific tolerance.

### 3.3 Brownian dynamics simulation of a bead-spring chain

#### 3.3.1 Model development

In NEMD simulations of shear flow, Section 4.1-2, the test liquid C<sub>78</sub>H<sub>158</sub> was conjectured to form tube-like structures composed of highly extended molecules,

through which other molecules rotated in hairpin configurations, as had also been observed in experiments of dilute DNA/water solutions [Teixeira *et al.*, 2005, 2007]. Chapter 4.3 will confirm this hypothesis, revealing definite correlations and timescales associated with tumbling events of individual molecules passing through tube-like structures of highly extended molecules. In light of this new evidence, it is possible that a realistic model of these linear, short-chain, unentangled molecular systems could be expressed in terms of a test chain placed in a mean-field that quantified the surrounding tube-like structure of highly extended chains through an anisotropic diffusion tensor, in which the diffusivity coefficient parallel to the chain or segmental backbone was greater than the coefficient perpendicular to the chain backbone.

### 3.3.2 Bead-spring model

The linear C<sub>78</sub>H<sub>158</sub> chain is modeled as a bead-spring chain. The 16 beads and 15 springs per chain were chosen as a good representation of the C<sub>78</sub>H<sub>158</sub> chain based on previous experience [Somasi *et al.*, 2002; Venkataramani *et al.*, 2008]. The bead-spring chain model consists of  $N$  (16) identical spherical beads connected by  $N-1$  (15) finitely extensible nonlinear elastic (FENE) springs. The FENE spring force law for each spring ( $\mathbf{F}_i^S$ ) is written as

$$F_{\alpha,i}^S = K h_i Q_{\alpha}^i, \quad h_i = \frac{1}{1 - |Q^i|^2 / b_s^2}, \quad i = 1, 2, \dots, N-1, \quad (19)$$

where the  $K$  and  $\mathbf{Q}^i$  denote the elastic spring constant and the connector vector of the  $i$ -th spring, respectively. The  $b_s$  represents the maximum extensibility of all springs. The  $h_i$  determines the specific form of elasticity inherent to the spring; when  $h_i=1$ , for example, the force law devolves into the linear Hookean spring. Note that Greek indices refer to the components of a Cartesian coordinate system and that the Einstein convention is assumed.

The fully-stretched length of the bead-spring chain is matched with the linear C<sub>78</sub>H<sub>158</sub> chain and the maximum extensibility of the spring ( $b_s$ ) is calculated using

$$b_m = \frac{3 \times R_{max}^2}{\langle R^2 \rangle_{eq}} = \frac{3 \times 9890(\text{\AA})^2}{1492(\text{\AA})^2} \approx 20 \quad ,$$

$$b_s = b_m / N^2 \approx 0.08889 \quad , \quad (20)$$

where  $R_{max}$  refers to the fully-stretched, end-to-end length of linear C<sub>78</sub>H<sub>158</sub>. The  $b_m$  and  $b_s$  denote the maximum extensibility of the entire molecule and each spring, respectively. The bead-spring model also possesses the same longest relaxation time as C<sub>78</sub>H<sub>158</sub> used in the NEMD simulations

For the unentangled liquids and semi-dilute solutions under consideration, a mean-field assumption is assumed to describe the effects of the oriented surrounding molecules on a test chain with the properties set forth above. This mean field is expressed through an anisotropic diffusion tensor,

$$\zeta_{\alpha\beta,i}^{-1} = \zeta_0^{-1} \left[ \alpha \delta_{\alpha\beta} + (1-\alpha) \tilde{Q}_\alpha^i \tilde{Q}_\beta^i \right] \quad , \quad (21)$$

where  $\delta_{\alpha\beta}$  denotes the unit tensor,  $\tilde{Q}_\alpha^i \equiv \sqrt{k_B T / K} Q_\alpha^i$  and  $\zeta_0^{-1}$  is the reciprocal of a frictional drag coefficient, assumed to be the same for each of the identical beads. The dimensionless parameter  $\alpha$  quantifies the influences on an individual chain from its surrounding chains, which are represented within the mean-field *ansatz* via the degree of anisotropy in the diffusion matrix. Note that this form of the diffusion tensor recovers the isotropic case when  $\alpha = 1$ .

### 3.3.3 Mesoscopic level of description

According to kinetic theory of polymeric liquids [Bird *et al.*, 1987b], three external forces act on each bead of a bead-spring model; the hydrodynamic drag force,  $\mathbf{F}_i^H$ , the effective spring force,  $\mathbf{F}_i^E$ , and the Brownian force,  $\mathbf{F}_i^B$ . Therefore, a force balance on the beads may be expressed as

$$\mathbf{F}_{\alpha,i}^H + \mathbf{F}_{\alpha,i}^E + \mathbf{F}_{\alpha,i}^B = 0 \quad , \quad i = 1, 2, \dots, N \quad , \quad (22)$$

where  $N$  is the total number of beads. Notice, as is usually the case, that we have neglected inertial contributions. In Eq. (22), the hydrodynamic drag force on each bead ( $\mathbf{F}_i^H$ ) is quantified by Stokes's law, which is expressed as

$$\mathbf{F}_{\alpha,i}^H = -\zeta_{\alpha\beta}^i (\dot{r}_\beta^i - v_\beta^i) \quad . \quad (23)$$

The  $\dot{r}_\beta^i$  and  $v_\beta^i (= v_\beta^0 + \kappa_{\beta\alpha} r_\alpha^i)$  denote components of the velocity and streaming velocity profile of the  $i$ -th bead, respectively, where  $\kappa_{\beta\alpha}$  is a component of the



transpose of the velocity gradient tensor. The  $\zeta_{\alpha\beta}^i$  represents an anisotropic friction matrix, which is the inverse of an anisotropic diffusion matrix. The effective spring force on bead  $i$  (the  $F_i^E$  in Eq. (23)) is expressed as

$$\mathbf{F}_{\alpha,i}^E = -\frac{\partial\phi}{\partial r_\alpha^i} . \quad (24)$$

where  $\phi$  denotes spring potential energy. The Brownian force on each bead is taken as

$$\mathbf{F}_{\alpha,i}^B = -k_B T \frac{\partial}{\partial r_\alpha^i} \ln \Psi , \quad (25)$$

where  $k_B$  and  $T$  denote the Boltzmann constant and temperature, respectively. The  $\Psi(\{\mathbf{r}^i\}, t)$  represents the configurational distribution function. By substituting Eqs. (23), and (25) into (22), and rearranging the equation, one obtains the equations of motion for the position vectors, which are

$$\dot{r}_\alpha^i = v_\alpha^0 + \kappa_{\alpha\beta} r_\beta^i - \zeta_{\alpha\beta,i}^{-1} \left[ F_{\beta,i}^E + \frac{k_B T}{\Psi} \frac{\partial \Psi}{\partial r_\beta^i} \right] . \quad (26)$$

From kinetic theory, the continuity equation of the distribution function  $\Psi(\{\mathbf{r}^i\}, t)$  is expressed as

$$\frac{\partial \Psi}{\partial t} = -\sum_{i=1}^N \frac{\partial}{\partial r_\alpha^i} (\dot{r}_\alpha^i \Psi) . \quad (27)$$

Therefore, the diffusion equation for  $\Psi(\{\mathbf{r}^i\}, t)$  can be obtained by inserting Eq. (26) into Eq. (27), which results in the expression

$$\frac{\partial \Psi}{\partial t} = -\sum_{i=1}^N \frac{\partial}{\partial r_\alpha^i} \left\{ \left( v_\alpha^0 + \kappa_{\alpha\beta} r_\beta^i - \zeta_{\alpha\beta,i}^{-1} F_{\beta,i}^E \right) \Psi - k_B T \zeta_{\alpha\beta,i}^{-1} \frac{\partial \Psi}{\partial r_\beta^i} \right\} . \quad (28)$$

For present purposes, this deterministic diffusion equation for the probability distribution function is rewritten in terms of a stochastic differential equation (SDE), which can then be split into a coupled set of evolution equations for the position vectors. The specific form of the diffusion equation for the distribution function is converted into the corresponding form of a SDE according to [Öttinger, 1996]

$$\frac{\partial \Psi}{\partial t} = - \sum_{i=1}^N \left\{ \frac{\partial}{\partial r_\alpha^i} [C_\alpha^i \Psi] + \frac{1}{2} \frac{\partial}{\partial r_\alpha^i} \frac{\partial}{\partial r_\beta^i} [\zeta_{\alpha\beta,i}^{-1} \Psi] \right\} \quad \rightarrow \quad dr_\alpha^i = C_\alpha^i dt + B_{\gamma\alpha}^i dW_\gamma^i \quad (29)$$

where  $\mathbf{W}$  represents the Wiener process.  $\mathbf{B}$  is the ‘square root’ of  $\zeta_{\alpha\beta,i}^{-1} (= B_{\alpha\gamma}^i B_{\gamma\beta}^i)$ , and is chosen as a lower triangular 3×3 matrix using Cholesky decomposition, which satisfies

$$\mathbf{B}^i \cdot (\mathbf{B}^i)^T = \begin{bmatrix} B_{11}^i & 0 & 0 \\ B_{21}^i & B_{22}^i & 0 \\ B_{31}^i & B_{32}^i & B_{33}^i \end{bmatrix} \cdot \begin{bmatrix} B_{11}^i & B_{12}^i & B_{13}^i \\ 0 & B_{22}^i & B_{23}^i \\ 0 & 0 & B_{33}^i \end{bmatrix} = \zeta_{\alpha\beta,i}^{-1} \quad (30)$$

Hence, Eq. (28) should be rearranged to have the specific form of configurational distribution as in Eq. (29) at mesoscopic level,

$$\frac{\partial \Psi}{\partial t} = - \sum_{i=1}^N \left[ \frac{\partial}{\partial r_\alpha^i} \left\{ \left( v_\alpha^0 + \kappa_{\alpha\beta} r_\beta^i - \zeta_{\alpha\beta,i}^{-1} F_{\beta,i}^E + k_B T \frac{\partial \zeta_{\alpha\beta,i}^{-1}}{\partial r_\beta^i} \right) \Psi \right\} \right] + k_B T \sum_{i=1}^N \frac{\partial}{\partial r_\alpha^i} \frac{\partial}{\partial r_\beta^i} (\zeta_{\alpha\beta,i}^{-1} \Psi) \quad (31)$$

Then one can obtain a SDE for the position vectors using Eqs. (29) and (30),

$$dr_\alpha^i = \left( v_\alpha^0 + \kappa_{\alpha\beta} r_\beta^i - \zeta_{\alpha\beta,i}^{-1} F_{\beta,i}^E + k_B T \frac{\partial \zeta_{\alpha\beta,i}^{-1}}{\partial r_\beta^i} \right) dt + B_{\alpha\beta}^i dW_\beta^i \quad (32)$$

$$\zeta_{\alpha\beta,i}^{-1} F_{\beta,i}^E = \begin{cases} \zeta_{\alpha\beta,1}^{-1} F_{\alpha,1}^S & \text{if } i = 1 \\ \zeta_{\alpha\beta,i}^{-1} F_{\alpha,i}^S - \zeta_{\alpha\beta,i-1}^{-1} F_{\alpha,i-1}^S & \text{if } 1 < i < N \\ -\zeta_{\alpha\beta,N-1}^{-1} F_{\alpha,N-1}^S & \text{if } i = N \end{cases}, \quad (33)$$

where  $F_i^S$  is the spring force associated with spring  $i$ .

Since the anisotropic diffusion matrix and stress tensor depend on the connector vector between adjacent beads, it is convenient to express the equation of motion using this vector. From definition of the connector vector ( $\mathbf{Q}^i = \mathbf{r}^{i+1} - \mathbf{r}^i$ ) with Eqs. (32) and (33), the SDE for the evolution of a connector vector can be obtained by

$$dQ_\alpha^i = \left( \kappa_{\alpha\beta} Q_\beta^i - \sum_{k=1}^{N-1} A_{ik} \left[ \zeta_{\alpha\beta,k}^{-1} F_{\beta,k}^S + k_B T \frac{\partial \zeta_{\alpha\beta,k}^{-1}}{\partial Q_\beta^k} \right] \right) dt + B_{\alpha\beta}^i (dW_\beta^{i+1} - dW_\beta^i), \quad (34)$$

$$\text{where } A_{ik} = \begin{cases} 2 & \text{if } |i-k|=0 \\ -1 & \text{if } |i-k|=1 \\ 0 & \text{otherwise} \end{cases}.$$

The  $A_{ik}$  are the elements of the Rouse matrix [Rouse, 1953]. Equation (34) can be made dimensionless with the transformations

$$Q_\alpha = \sqrt{\frac{k_B T}{K}} \tilde{Q}_\alpha, \quad t = \frac{L}{V_c} \tilde{t}, \quad \tau_R = \frac{\zeta_0}{4K} = \tilde{\tau}_R \frac{L}{V_c}, \quad Wi = \dot{\gamma} \tau_R = \frac{V_c}{L} \tau_R, \quad dW_\alpha^i = \sqrt{dt} d\tilde{W}_\alpha^i$$

$$\zeta_{\alpha\beta}^{-1} = \zeta_0^{-1} \tilde{\zeta}_{\alpha\beta}^{-1}, \quad \kappa_{\alpha\beta} = \frac{V_c}{L} \tilde{\kappa}_{\alpha\beta}, \quad F_\beta = \sqrt{K k_B T} \tilde{F}_\beta, \quad B_{\alpha\beta} = \sqrt{2 k_B T \zeta_0^{-1}} \tilde{B}_{\alpha\beta}. \quad (35)$$

Note that the terms with a tilde are dimensionless. The  $Wi$  is the Weissenberg number and  $\tau_R$  is the Rouse time. The  $V_c$  is an arbitrary velocity scale and  $L$  is an arbitrary length scale. As a result, the dimensionless equation for  $dQ_\alpha^i$  is

$$d\tilde{Q}_\alpha^i = \left( \tilde{\kappa}_{\alpha\beta} \tilde{Q}_\beta^i - \frac{1}{4Wi} \sum_{k=1}^{N-1} A_{ik} \left[ \tilde{\zeta}_{\alpha\beta,k}^{-1} \tilde{F}_{\beta,k}^S + \frac{\partial \tilde{\zeta}_{\alpha\beta,k}^{-1}}{\partial \tilde{Q}_\beta^k} \right] \right) d\tilde{t} + \frac{1}{\sqrt{2Wi}} \tilde{B}_{\alpha\beta}^i (d\tilde{W}_\beta^{i+1} - d\tilde{W}_\beta^i). \quad (36)$$

Finally, we obtain the stochastic evolution equation of the connector vector by substituting the FENE spring force law and the anisotropic diffusion matrix into Eq. (36),

$$d\tilde{Q}_\alpha^i = \left( \tilde{\kappa}_{\alpha\beta} \tilde{Q}_\beta^i - \frac{1}{4Wi} \sum_{k=1}^{N-1} A_{ik} \left\{ h_k \left[ \alpha + (1-\alpha) \left( \tilde{Q}_\beta^k \right)^2 \right] \tilde{Q}_\alpha^k + 2(1-\alpha) \tilde{Q}_\alpha^k \right\} \right) d\tilde{t} + \frac{1}{\sqrt{2Wi}} \tilde{B}_{\alpha\beta}^i (d\tilde{W}_\beta^{i+1} - d\tilde{W}_\beta^i). \quad (37)$$

### 3.3.4 Continuum level of description

One can express Eq. (26) in terms of  $\mathbf{Q}^i$  and  $\psi(\{\mathbf{Q}^{N-1}\}, t)$

$$\frac{\partial \psi}{\partial t} = - \sum_{i=1}^{N-1} \frac{\partial}{\partial Q_\alpha^i} \left\{ \kappa_{\alpha\beta} Q_\beta^i \psi - \sum_{k=1}^{N-1} A_{ik} \zeta_{\alpha\beta,k}^{-1} \left[ F_{\beta,k}^S \psi + k_B T \frac{\partial \psi}{\partial Q_\beta^k} \right] \right\}. \quad (38)$$

At the continuum level, the diffusion equation of the distribution function was further coarse-grained through pre-averaging. By multiplying  $Q_\alpha^i Q_\beta^i$  on each side of Eq. (38) and then integrating over all the configuration space, one can derive the equation of change for  $\langle Q_\alpha^i Q_\beta^i \rangle$ , which is written as

$$\begin{aligned} \frac{\partial}{\partial t} \langle \mathcal{Q}_\alpha^i \mathcal{Q}_\beta^i \rangle &= \kappa_{\alpha\varepsilon} \langle \mathcal{Q}_\beta^i \mathcal{Q}_\varepsilon^i \rangle + \kappa_{\beta\varepsilon} \langle \mathcal{Q}_\alpha^i \mathcal{Q}_\varepsilon^i \rangle + \\ &\sum_{k=1}^{N-1} A_{ik} \left[ 2k_B T \left\langle \frac{\partial}{\partial \mathcal{Q}_\varepsilon^k} \zeta_{\alpha\varepsilon,k}^{-1} \mathcal{Q}_\beta^k \right\rangle + 2k_B T \left\langle \frac{\partial}{\partial \mathcal{Q}_\varepsilon^k} \zeta_{\beta\varepsilon,k}^{-1} \mathcal{Q}_\alpha^k \right\rangle - 2 \langle \zeta_{\alpha\varepsilon,k}^{-1} \mathcal{Q}_\beta^k F_{\alpha,k}^S \rangle - 2 \langle \zeta_{\beta\varepsilon,k}^{-1} \mathcal{Q}_\alpha^k F_{\beta,k}^S \rangle \right], \end{aligned} \quad (39)$$

for  $i = 1, 2, \dots, N-1$ . Here, the definition of the average property,  $\langle E \rangle = \int E \psi d\mathbf{Q}^i$ , is used. In this study, the upper convected time derivative is defined by

$$\frac{D}{Dt} \langle \mathcal{Q}_\alpha^i \mathcal{Q}_\beta^i \rangle = \frac{\partial}{\partial t} \langle \mathcal{Q}_\alpha^i \mathcal{Q}_\beta^i \rangle - \kappa_{\alpha\varepsilon} \langle \mathcal{Q}_\beta^i \mathcal{Q}_\varepsilon^i \rangle - \kappa_{\beta\varepsilon} \langle \mathcal{Q}_\alpha^i \mathcal{Q}_\varepsilon^i \rangle. \quad (40)$$

Thus, Eq. (39) can be also written as

$$\begin{aligned} \frac{D}{Dt} \langle \mathcal{Q}_\alpha^i \mathcal{Q}_\beta^i \rangle &= \sum_{k=1}^{N-1} A_{ik} \left[ 2k_B T \left\langle \frac{\partial}{\partial \mathcal{Q}_\varepsilon^k} \zeta_{\alpha\varepsilon,k}^{-1} \mathcal{Q}_\beta^k \right\rangle + 2k_B T \left\langle \frac{\partial}{\partial \mathcal{Q}_\varepsilon^k} \zeta_{\beta\varepsilon,k}^{-1} \mathcal{Q}_\alpha^k \right\rangle \right. \\ &\left. - 2 \langle \zeta_{\alpha\varepsilon,k}^{-1} \mathcal{Q}_\beta^k F_{\alpha,k}^S \rangle - 2 \langle \zeta_{\beta\varepsilon,k}^{-1} \mathcal{Q}_\alpha^k F_{\beta,k}^S \rangle \right]. \end{aligned} \quad (41)$$

Eq. (41) can be also expressed in dimensionless form using the transformations of Eq. (35),

$$\begin{aligned} \frac{D}{D\tilde{t}} \langle \tilde{\mathcal{Q}}_\alpha^i \tilde{\mathcal{Q}}_\beta^i \rangle &= \sum_{k=1}^{N-1} A_{ik} \left[ \frac{1}{2} \left\langle \frac{\partial}{\partial \tilde{\mathcal{Q}}_\varepsilon^k} \tilde{\zeta}_{\alpha\varepsilon,k}^{-1} \tilde{\mathcal{Q}}_\beta^k \right\rangle + \frac{1}{2} \left\langle \frac{\partial}{\partial \tilde{\mathcal{Q}}_\varepsilon^k} \tilde{\zeta}_{\beta\varepsilon,k}^{-1} \tilde{\mathcal{Q}}_\alpha^k \right\rangle \right. \\ &\left. - \frac{1}{2} \langle \tilde{\zeta}_{\alpha\varepsilon,k}^{-1} \tilde{\mathcal{Q}}_\beta^k \tilde{F}_{\alpha,k}^S \rangle - \frac{1}{2} \langle \tilde{\zeta}_{\beta\varepsilon,k}^{-1} \tilde{\mathcal{Q}}_\alpha^k \tilde{F}_{\beta,k}^S \rangle \right]. \end{aligned} \quad (42)$$

Introducing the FENE spring force law and the anisotropic diffusion matrix into Eqn. (42) gives

$$\frac{D}{D\tilde{t}} \langle \tilde{\mathcal{Q}}_\alpha^i \tilde{\mathcal{Q}}_\beta^i \rangle = \sum_{k=1}^{N-1} A_{ik} \left[ -h_k (1-\alpha) \langle \tilde{\mathcal{Q}}_\varepsilon^k \tilde{\mathcal{Q}}_\varepsilon^k \tilde{\mathcal{Q}}_\alpha^k \tilde{\mathcal{Q}}_\beta^k \rangle \right]$$

$$-h_k \alpha \langle \tilde{\mathcal{Q}}_\alpha^k \tilde{\mathcal{Q}}_\beta^k \rangle + 3(1-\alpha) \langle \tilde{\mathcal{Q}}_\alpha^k \tilde{\mathcal{Q}}_\beta^k \rangle + \alpha \delta_{\alpha\beta} \Big]. \quad (43)$$

In Eq. (43), the fourth-rank tensor can be written in terms of second-rank tensors using the closure approximation proposed by Doi (1981), which has been shown to satisfy time-structure invariance by Edwards and Öttinger (1997):

$$\langle \tilde{\mathcal{Q}}_\varepsilon^k \tilde{\mathcal{Q}}_\varepsilon^k \tilde{\mathcal{Q}}_\alpha^k \tilde{\mathcal{Q}}_\beta^k \rangle \Rightarrow \langle \tilde{\mathcal{Q}}_\varepsilon^k \tilde{\mathcal{Q}}_\varepsilon^k \rangle \langle \tilde{\mathcal{Q}}_\alpha^k \tilde{\mathcal{Q}}_\beta^k \rangle \Rightarrow \left( \tilde{\mathcal{Q}}_\varepsilon^k \right)^2 \langle \tilde{\mathcal{Q}}_\alpha^k \tilde{\mathcal{Q}}_\beta^k \rangle \quad (44)$$

Finally, the constitutive equation at the continuum level is obtained as

$$\frac{D}{D\tilde{t}} \langle \tilde{\mathcal{Q}}_\alpha^i \tilde{\mathcal{Q}}_\beta^i \rangle = \sum_{k=1}^{N-1} A_{ik} \left\{ -h_k \left[ (1-\alpha) \left( \tilde{\mathcal{Q}}_\varepsilon^k \right)^2 + \alpha \right] \langle \tilde{\mathcal{Q}}_\alpha^k \tilde{\mathcal{Q}}_\beta^k \rangle + 3(1-\alpha) \langle \tilde{\mathcal{Q}}_\alpha^k \tilde{\mathcal{Q}}_\beta^k \rangle + \alpha \delta_{\alpha\beta} \right\}. \quad (45)$$

Note that Eq. (43) should recover typical FENE dumbbell model for  $\alpha=1$  and  $N=2$ ,

$$\begin{aligned} \frac{D}{D\tilde{t}} \tilde{C}_{\alpha\beta} &= -h \left[ (1-\alpha) \text{tr} \tilde{C} + \alpha \right] \tilde{C}_{\alpha\beta} + 3(1-\alpha) \tilde{C}_{\alpha\beta} + \alpha \delta_{\alpha\beta}, \\ &= -h \tilde{C}_{\alpha\beta} + \delta_{\alpha\beta}, \end{aligned} \quad (46)$$

$$\tilde{C}_{\alpha\beta} = \langle \tilde{\mathcal{R}}_\alpha \tilde{\mathcal{R}}_\beta \rangle, \quad \tilde{\mathcal{R}}_\alpha = \sum_{i=1}^{N-1} \tilde{\mathcal{Q}}_\alpha^i = r_\alpha^N - r_\alpha^1, \quad (47)$$

$$\text{when } N=2, \quad \tilde{C}_{\alpha\beta} = \langle \tilde{\mathcal{R}}_\alpha \tilde{\mathcal{R}}_\beta \rangle = \langle \tilde{\mathcal{Q}}_\alpha \tilde{\mathcal{Q}}_\beta \rangle,$$

where  $\tilde{r}_\alpha^i$  denotes the dimensionless position vector of  $i$ -th bead and the  $\tilde{C}_{\alpha\beta}$  denotes dimensionless conformation tensor.

### 3.3.5 Rheological and structural properties

The stress tensor is given by Kramers' expression [Bird, 1987], and written in dimensionless form according to the transformations of Eq. (35),

$$\tilde{\sigma}_{\alpha\beta} = \sum_{i=1}^{N-1} h_i \langle \tilde{Q}_\alpha^i \tilde{Q}_\beta^i \rangle - \delta_{\alpha\beta}. \quad (48)$$

In this study, the rheological material function plays an important role in comparing results from each level of description. The viscosity and the normal stress coefficients are defined by

$$\eta = \frac{\tilde{\sigma}_{xy}}{\tilde{\gamma}}, \quad (49)$$

$$\Psi_1 = \frac{\tilde{\sigma}_{xx} - \tilde{\sigma}_{yy}}{\tilde{\gamma}^2}, \quad (50)$$

$$\Psi_2 = \frac{\tilde{\sigma}_{yy} - \tilde{\sigma}_{zz}}{\tilde{\gamma}^2}. \quad (51)$$

The average conformational changes of the chain under shear flow can be expressed using various properties such as the conformation tensor, radius of gyration, orientation angle, and so on. These properties can be defined as follows. The radius of gyration tensor is defined as

$$\tilde{G}_{\alpha\beta} = \frac{1}{N} \sum_{i=1}^N (\tilde{r}_\alpha^i - \tilde{r}_\alpha^c)(\tilde{r}_\beta^i - \tilde{r}_\beta^c), \quad (52)$$

where the position vector of the center of mass is given by,

$$\tilde{r}_\gamma^c = \frac{1}{N} \sum_{i=1}^N \tilde{r}_\gamma^i. \quad (53)$$

The molecular configuration thickness of the bead-spring chain is computed using the radius of gyration tensor with orthogonal components

$$\delta_x = \sqrt{\tilde{G}_{xx}}, \quad \delta_y = \sqrt{\tilde{G}_{yy}}, \quad \delta_z = \sqrt{\tilde{G}_{zz}}. \quad (54)$$

The orientation angle ( $\theta$ ) also can be calculated using the radius of gyration tensor [Hess, 1987; Kroger, 2005; Thomas *et al.*, 2009],

$$\tan(2\theta) = \frac{2\tilde{G}_{xy}}{\tilde{G}_{xx} - \tilde{G}_{yy}}. \quad (55)$$

### 3.4 Topological Z-code algorithm

Quantities characterizing the entanglement network have been obtained from configurational snapshots by using the geometric Z-code [Vladkov and Barrat, 2006; Kröger, 2005], which efficiently produces results in agreement with its dynamical counterpart, as demonstrated and discussed in detail in Shanbhag and Kröger (2006). The Z-code had been applied in Foteinopoulou *et al.* (2006) to identify entanglements and to quantify entanglement statistics in polyethylene melts. The method adopted in our ‘topological’ analysis solves the problem of the shortest multiple disconnected path, in the sense of a minimum Euclidean length subject to excluded volume (uncrossability of primitive paths) and constraints arising from the initial state (fixed chain end coordinates). In contrast to dynamical counterparts, the Z-code does not lose entanglements during ‘relaxation,’ and it has many common features with an alternate implementation of the same geometric idea--the so called CReTA package



[Tzoumanekas and Theodorou, 2006]. Details about the  $Z$ -code can be found in the literature. [Vladkov and Barrat, 2006; Kröger, 2005]. When applied to a polymeric configuration, it returns the instantaneous configuration of the complete entanglement network, from which various quantities such as network anisotropy, contour length, stiffness, mesh size, number of knots, and further characteristics, can be evaluated.

For the purpose of the present manuscript, we evaluated the lengths of primitive paths,  $L_{pp}$ , defined as the contour length of the whole entanglement network (shortest disconnected path) divided by the number of polymer chains. From this length, together with the assumption of random walk statistics for the primitive path, one usually defines a ‘number of entanglements’ via  $Z_{coil} = L_{pp}^2 / \langle R_{ete}^2 \rangle - 1$ , where  $\langle R_{ete}^2 \rangle$  denotes the mean squared end-to-end distance, and a ‘tube radius’,  $a_{pp} = \langle R_{ete}^2 \rangle / Z_{coil}$ . As the entanglement network becomes anisotropic under flow conditions,  $L_{pp}$ , rather than  $Z_{coil}$  or  $a_{pp}$ , contains the most relevant information for the reason that the above assumption is generally invalid, in particular under nonequilibrium conditions [Kröger, 2004, 2005; Tzoumanekas and Theodorou, 2006]. The development of the geometric algorithms makes it possible to investigate the dynamics of the entanglement network, as demonstrated in this manuscript. This is made possible since the analysis of many configurations can typically be completed within a few seconds on a laptop computer, as compared to several days for a single configuration not two years ago.

### 3.5 Brightness distribution for configurations of chain molecules

The dynamics of individual DNA molecules have been observed under shear using video fluorescence microscopy during the past decade [Smith and Chu, 1998; Smith *et al.*, 1999; LeDuc *et al.*, 1999; Teixeira *et al.*, 2005; Schroeder *et al.*, 2005; Robertson and Smith, 2007]. In this technique, the internal configuration of the chain is related to the brightness of the signal as measured under a microscope since the individual DNA molecules are fluorescently marked. In other words, the brightness changes according to the configurational distribution of chains at a specific spatial location. For example, the coiled configuration appears brighter than other conformations because the radius of gyration of the chain is smaller, thus the fluorescently labeled atoms are more densely packed.

In a similar vein to the experimental brightness measurements, the same idea has been applied to simulation data to classify numerous configurations of chain molecules and to track the configurational changes of specific molecules as a function of  $Wi$  [Venkataramani *et al.*, 2008]. The analysis presented below follows exactly the scheme of Venkataramani *et al.* (2008), and will not be explained here. Figure 3.4.1 displays the configuration classes of the chain molecules considered in this work: they are, in order of increasing magnitude of the end-to-end vector, coil, fold, dumbbell, kink, half-dumbbell, and stretched.

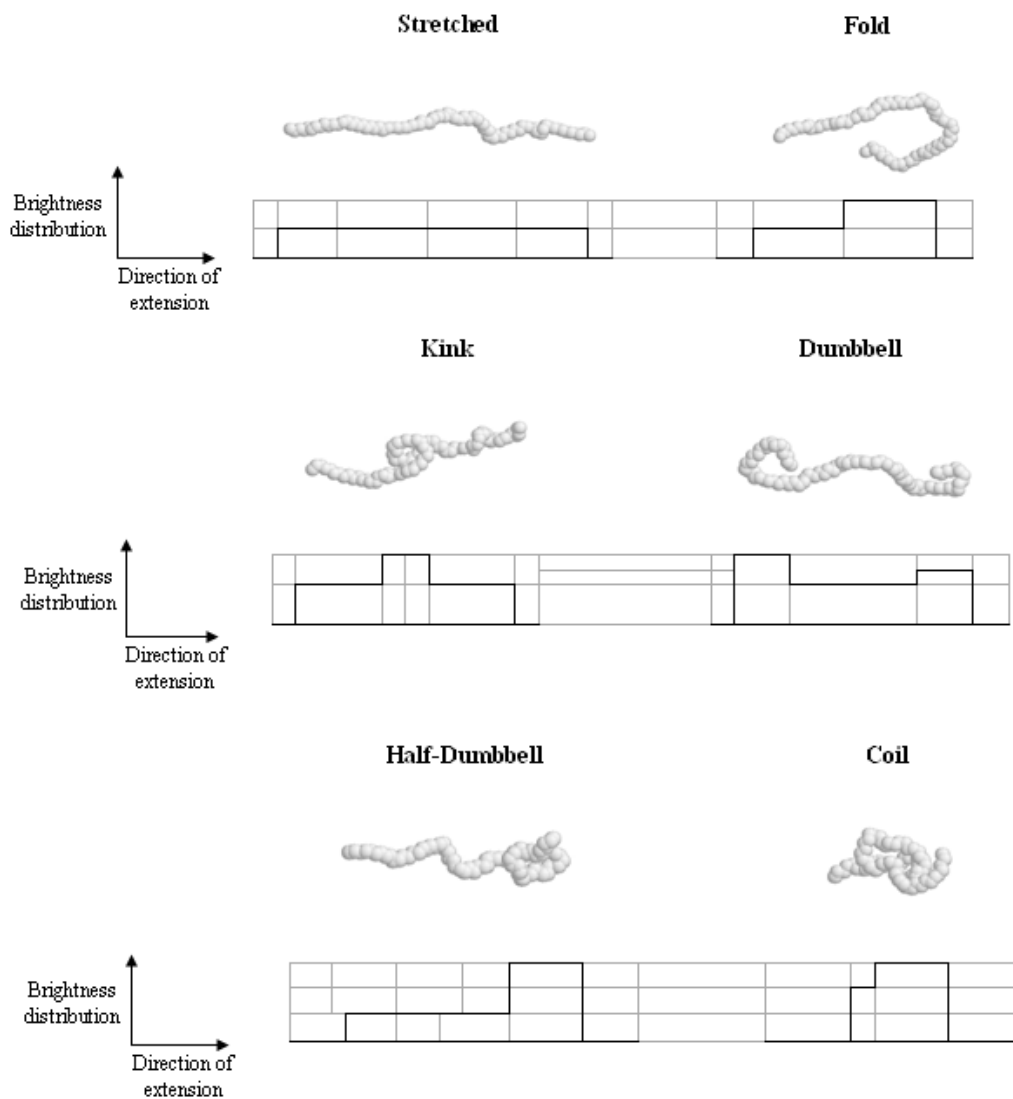


Fig. 3.4.1. Representative configuration classes of chain molecules as defined by the brightness distribution of Venkataramani *et al.* (2008).

## Chapter IV Results and discussion

### 4.1 Rheological and entanglement characteristics of linear-chain polyethylene liquids in shear and planar elongational flows at the atomistic level using nonequilibrium molecular dynamics simulation

In Fig. 4.1.1, the viscosities are displayed as functions of strain rate for the polyethylene liquids, as in Refs. [Cui *et al.*, 1996; Baig *et al.*, 2005b, 2006a, 2006b,]. Note that  $\eta_2$  is not displayed, for conciseness, since the results are qualitatively similar to those of  $\eta_1$ , and since they may be found in Refs. [Baig *et al.* 2005b, 2006a]. Statistical uncertainties were calculated using Eq. (28) of Ref. [Flyvbjerg and Petersen, 1989]. The values of the shear viscosity at various shear rates are tabulated in Table 4.1.1. Similar tables for the elongational viscosities can be found in Refs. [Baig *et al.*, 2005b, 2006b]. As evident, all of the viscosities decrease as the strain rate increases. In other words, shear- and tension-thinning behavior is observed for all four polyethylene melts. Furthermore, the shear- and tension-thinning behaviors are more pronounced for the longer chains in both shear and PEF. It was observed in Refs. [Baig *et al.* 2005b, 2006b] that the zero shear-rate viscosity was approximately equal to the zero elongation-rate viscosity for short-chain n-alkanes in both shear and PEF, in accordance with Trouton's ratio. Here, the applicability of this rule to linear short-chain polyethylenes is also observed in both shear and PEF. Both viscosities were estimated based on the plateau values in Fig. 4.1.1. The zero shear-rate viscosities of

the linear short-chain polyethylenes are  $\eta_{C_{50}H_{102}} = 1.96 \pm 0.1$  cp,  $\eta_{C_{128}H_{258}} = 10.04 \pm 1.25$  cp, and  $\eta_{C_{78}H_{158}} = 4.77 \pm 0.25$  cp, and the zero strain-rate viscosities (both  $\eta_1$ ,  $\eta_2$ ) are  $\eta_{C_{50}H_{102}} = 2.2 \pm 0.4$  cp,  $\eta_{C_{78}H_{158}} = 5.0 \pm 0.8$  cp, and  $\eta_{C_{128}H_{258}} = 10.7 \pm 2.8$  cp. The power-law indices ( $\eta_{shear} \propto \dot{\gamma}^b$ ,  $\eta_{elong} \propto \dot{\epsilon}^b$ ) for all polyethylene melts were also calculated. It is typical that the experimental value of  $b$  lies within the range of [-0.4,-0.9] for polymeric liquids. From Fig. 4.1.1, the 5 highest strain rate values were selected to regress the power-law index. The values of  $b$  for the polyethylene melts under shear flow are  $-0.39 \pm 0.01$  for  $C_{24}H_{50}$ ,  $-0.34 \pm 0.01$  for  $C_{50}H_{102}$ ,  $-0.35 \pm 0.01$  for  $C_{78}H_{158}$ , and  $-0.34 \pm 0.01$  for  $C_{128}H_{258}$ . These values are close to those of the prior analysis of Moore *et al.* ( $b = -0.35$ ) [Moore *et al.*, 2000]. The  $b$  values of the polyethylene liquids under PEF for  $\eta_1$  are  $-0.37 \pm 0.01$  for  $C_{50}H_{102}$ ,  $-0.42 \pm 0.01$  for  $C_{78}H_{158}$ , and  $-0.46 \pm 0.02$  for  $C_{128}H_{258}$ , from the previous study [Baig *et al.*, 2006b]. While the slope of  $\eta_1$  increases as the chain length increases under PEF, the slope of  $\eta$  looks to be insensitive to the chain length at high shear rate values.

The shear-thinning behavior arises due the relative stress relief offered to the liquids as the molecules stretch and align at a small angle with respect to the flow direction at high rates of shear [Bird *et al.*, 1987; Morrison, 2001]. In elongational flow, the chains continue to stretch at the highest strain rates we could simulate, and thus the longer chains continue to display a greater degree of tension-thinning—see Fig. 4.1.2, herein, and Table II of Ref. [Baig *et al.*, 2006b].

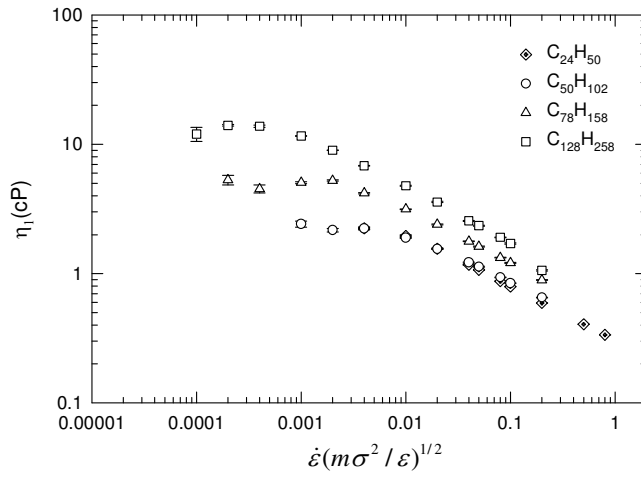
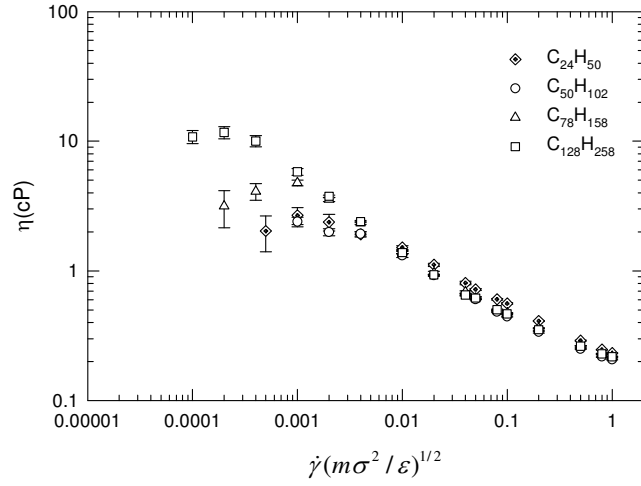


Fig. 4.1.1. Comparison of  $\eta$  and  $\eta_1$  for polyethylene melts as functions of strain rate.

TABLE 4.1.1 Shear viscosities  $\eta$  as functions of dimensionless shear rate for  $C_{50}H_{102}$ ,  $C_{78}H_{158}$ , and  $C_{128}H_{258}$ . The numbers in parentheses represent the statistical uncertainties in the least significant digits calculated using Eq. (28) of [Flyvbjerg and Petersen,1989].

$\dot{\gamma}^*$ (LJu)	$C_{50}H_{102}$		$C_{78}H_{158}$		$C_{128}H_{258}$	
	$\eta$ (cp)	Run (ns)	$\eta$ (cp)	Run (ns)	$\eta$ (cp)	Run (ns)
0.0001					10.814 (1257)	30.39
0.0002			3.160 (1005)	16.46	11.702 (1257)	28.09
0.0004			4.108 (604)	14.11	10.045 (1006)	25.89
0.001	2.393 (201)	11.76	4.772 (251)	11.76	5.804 (352)	23.25
0.002	1.992 (126)	9.15	3.549 (126)	10.58	3.765 (75)	22.13
0.004	1.930 (75)	8.23	2.339 (63)	9.40	2.399 (45)	13.85
0.01	1.315 (45)	5.88	1.400 (40)	5.88	1.383 (25)	5.88
0.02	0.923 (18)	4.70	0.964 (30)	4.68	0.933 (9)	4.57
0.04	0.655 (13)	3.05	0.689 (13)	3.52	0.653 (10)	3.48
0.05	0.604 (7)	2.95	0.616 (10)	3.52	0.618 (15)	3.35
0.08	0.482 (6)	2.82	0.498 (6)	2.52	0.501 (8)	2.77
0.1	0.443 (4)	2.82	0.473 (5)	2.82	0.466 (5)	2.75
0.2	0.338 (5)	2.35	0.361 (5)	2.35	0.352 (8)	2.12
0.5	0.250 (2)	2.35	0.262 (4)	2.35	0.262 (3)	2.35
0.8	0.218 (2)	2.35	0.229 (2)	2.15	0.229 (2)	2.31
1	0.207 (2)	2.35	0.218 (2)	2.02	0.217 (2)	2.24

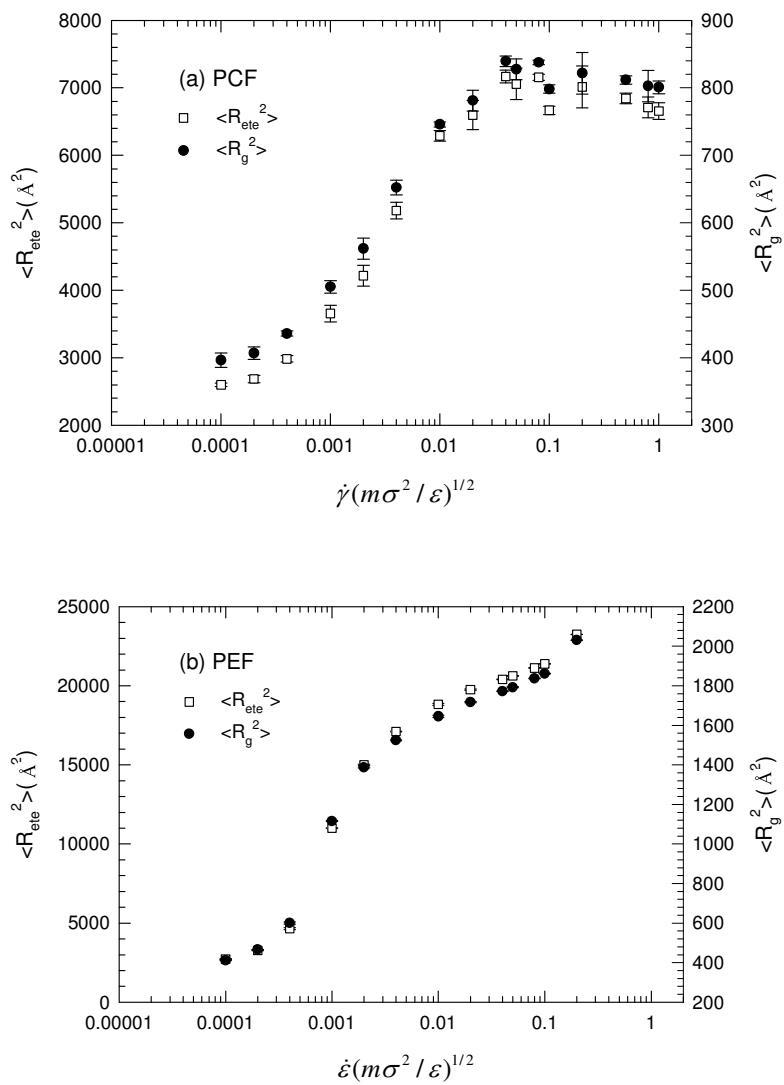


Fig. 4.1.2. The mean-square chain end-to-end distance,  $\langle R_{ete}^2 \rangle$ , and the mean square chain radius of gyration,  $\langle R_g^2 \rangle$ , for  $C_{128}H_{258}$  under shear and PEF as functions of strain rate.



TABLE 4.1.2 The mean-square, end-to-end distance of chains and the mean-square radius of gyration of chains as functions of dimensionless shear rate for  $C_{50}H_{102}$ ,  $C_{78}H_{158}$ , and  $C_{128}H_{258}$ . The numbers in parentheses represent the statistical uncertainties in the least significant digits calculated using Eq. (28) of [Flyvbjerg and Petersen,1989].

$\dot{\gamma}^*$ (LJu)	$C_{50}H_{102}$		$C_{78}H_{158}$		$C_{128}H_{258}$	
	$\langle R_{ete}^2 \rangle$ ( $\text{\AA}^2$ )	$\langle R_g^2 \rangle$ ( $\text{\AA}^2$ )	$\langle R_{ete}^2 \rangle$ ( $\text{\AA}^2$ )	$\langle R_g^2 \rangle$ ( $\text{\AA}^2$ )	$\langle R_{ete}^2 \rangle$ ( $\text{\AA}^2$ )	$\langle R_g^2 \rangle$ ( $\text{\AA}^2$ )
0	883 (9)	123 (1)	1492 (25)	218 (3)	2566 (20)	389 (2)
0.0001					2598 (25)	396 (11)
0.0002			1480 (22)	218 (1)	2686 (54)	407 (9)
0.0004			1472 (31)	217 (3)	2985 (46)	436 (4)
0.001	916 (9)	125 (1)	1628 (26)	229 (2)	3656 (124)	505 (9)
0.002	925 (8)	126 (1)	1729 (39)	241 (4)	4217 (154)	562 (15)
0.004	956 (14)	129 (1)	2073 (54)	270 (4)	5180 (124)	652 (11)
0.01	1065 (23)	137 (2)	2447 (77)	302 (6)	6288 (77)	746 (4)
0.02	1164 (29)	145 (2)	2726 (93)	324 (8)	6596 (216)	781 (15)
0.04	1289 (23)	154 (2)	2932 (54)	341 (5)	7168 (93)	839 (8)
0.05	1278 (17)	153 (1)	2855 (54)	335 (5)	7058 (232)	827 (15)
0.08	1306 (31)	154 (2)	2974 (62)	345 (5)	7155 (46)	837 (3)
0.1	1357 (17)	158 (1)	2978 (62)	345 (6)	6667 (62)	798 (6)
0.2	1343 (15)	158 (1)	2900 (54)	339 (6)	7013 (309)	822 (31)
0.5	1283 (19)	152 (2)	2750 (39)	327 (2)	6842 (77)	812 (6)
0.8	1289 (17)	152 (2)	2784 (46)	329 (4)	6709 (154)	803 (23)
1	1274 (14)	151 (1)	2787 (31)	329 (3)	6655 (124)	801 (9)

In Fig. 4.1.2, which offers data for  $C_{128}H_{258}$ , the mean-square of chain end-to-end vector,  $\langle R_{ete}^2 \rangle$ , continues to increase at high strain rates, indicating that the chains are elongating more and more as the strain rate increases. However, for shear flow, at the highest shear rates simulated, Fig. 4.1.2 and Table 4.1.2 demonstrate that the chains are substantially elongated, and approach a high shear-rate maximum-extension region at the same rate, independent of chain length. Fig. 4.1.3 displays some sample configurations from the simulations of  $C_{128}H_{258}$  under equilibrium, shear, and PEF conditions. Note that the upper simulation boxes display the entire number of chains in the systems, whereas the lower boxes only display ten randomly selected chains, rendering the remainder invisible. From these snapshots, some observations become evident which are directly compatible with the information apparent in Fig. 4.1.2. At equilibrium, the chains maintain their random coil configurations, whereas under flow, they become stretched and oriented on average relative to the flow field. In PEF, the chains stretch substantially in the direction of flow, assuming intramolecular configurations that are very similar to those in polyethylene crystalline structures [Ionescu *et al.*, 2006]. Occasionally, a molecule will rotate within the elongational flow field, as the chain will fold back on itself and switch chain-end orientation in much the same way that a snake changes its direction by  $180^\circ$ . In shear flow, the chains continuously rotate, being only on average stretched and aligned with respect to the shear field. At low shear rates, the chains rotate spherically, similarly to basketballs. At high shear rates, the chains rotate in the snake-like fashion, maintaining rather highly elongated conformations at the extremes.

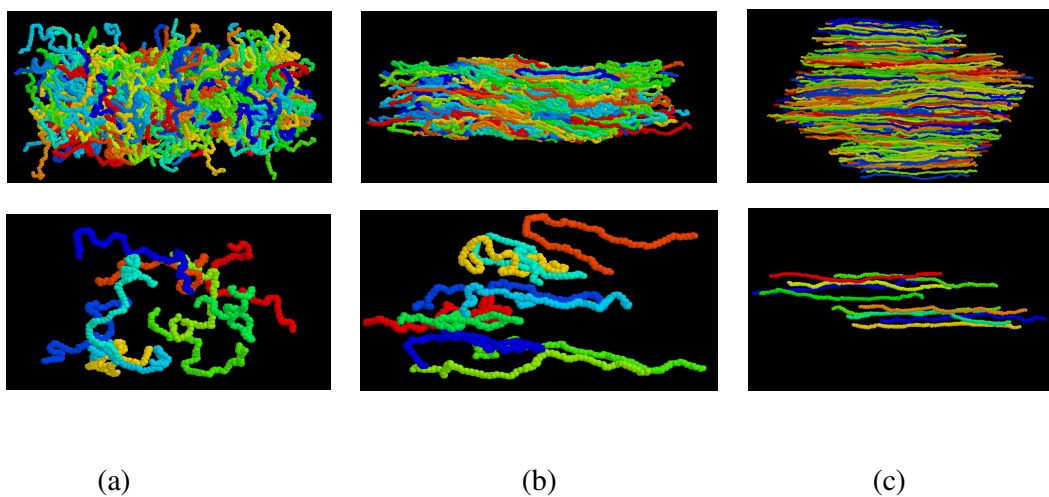


Fig. 4.1.3. Snapshots of molecular configurations under equilibrium (a), shear flow at the highest shear rate simulated,  $\dot{\gamma}^* = 0.8$  (b), and PEF at the highest strain rate simulated,  $\dot{\epsilon}^* = 0.2$  (c) for  $C_{128}H_{258}$ .

The stress tensor consists of two contributions from a microscopic viewpoint, the kinetic and potential, see Eq. (10). Since the kinetic part is mandated by the system temperature, the potential part plays a dominant role in determining the mean pressure for all dense liquids (the opposite is true for gases), cf. Refs. [Kröger *et al.*, 1993; Baig *et al.*, 2005b, 2006b]. Consequently, the intermolecular interaction energy of the system should possess a qualitative similarity with the potential part of the pressure tensor. Therefore, the features of the pressure profiles with respect to strain rate in comparison to the profiles of the intermolecular LJ (potential) energy were investigated. The mean pressure is graphed as a function of strain rate in Fig. 4.1.4, and the intermolecular LJ energy is displayed in Fig. 4.1.5. The qualitative behavior of the mean pressure is very similar between shear and PEF: after the initial Newtonian plateau at low shear rates, the mean pressure decreases at intermediate values of the strain rate, although more substantially under PEF, and then increases sharply for high strain rates. For  $C_{24}H_{50}$  at the highest value of strain rate in PEF, there appears to be a plateau or maximum forming in the mean pressure profile. The stress decreases at intermediate strain rates because the chain molecules are extending and reorienting rapidly in this regime (see Fig. 4.1.2), which manifests as an extreme degree of strain-rate thinning not only in the viscosities, but also in the diagonal components of the stress tensor. For instance, in shear flow, it has been demonstrated that the first normal stress coefficient (which is related to the diagonal components of the pressure tensor) shear thins to a very high extent throughout this shear rate regime [Baig *et al.*, 2006b]. Once a critical shear rate is achieved where the chain extension

begins to decrease with increasing shear rate—see the maximum in Fig. 4.1.2a, and the point where the slope decreases dramatically in Fig. 4.1.2b—there is a minimum in the mean pressure profiles. Subsequently, the mean pressure increases rather dramatically with increasing strain rate.

To investigate the potential contribution to the mean pressure, the intermolecular LJ potential energy per united atom is plotted as a function of strain rate in Fig. 4.1.5. (The reason that the  $C_{24}H_{50}$  intermolecular LJ energy is so much lower than the other three is because this simulation was at a lower value of the temperature.) As evident, the overall shapes of these energy curves are very similar to those of the mean pressure. The intermolecular LJ energy decreases with increasing strain rate at low values, and then it reaches a minimum value at intermediate strain rates. At high strain rates, it increases, and for  $C_{24}H_{50}$  and  $C_{128}H_{258}$  under PEF, it exhibits a precipitous drop at extremely high strain rates. These phenomena can be explained by consideration of two competing effects, chain orientational effects and Brownian-type collision effects, each manifesting in a different strain rate regime. At low strain rates, the torsion angles of the chains assume more *trans*-conformations with increasing strain rate. This increases the interaction area between neighboring molecules, and decreases the intermolecular LJ energy. As the strain rate increases into the regime of high values, chain rotation and tumbling for shear and molecular collisions for elongational flow (atomic interactions, which push the molecules apart) play a more important role, eventually dominating over the chain extension effects. The intermolecular LJ energy therefore increases with strain rate. For  $C_{24}H_{50}$  and

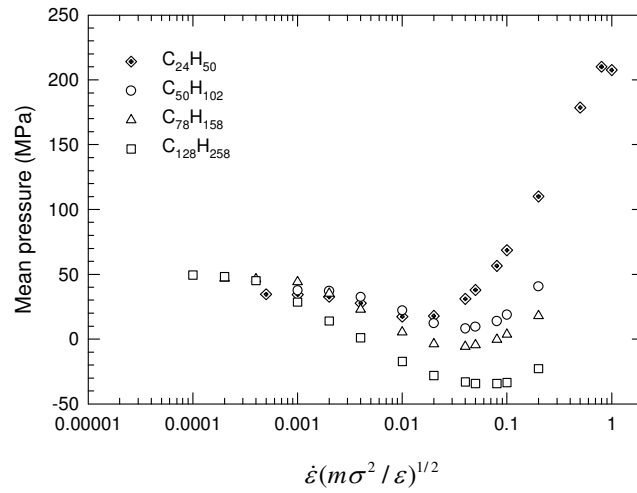
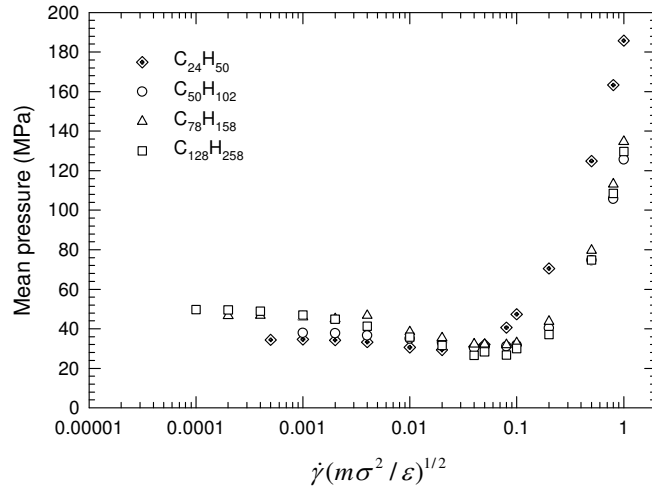


Fig. 4.1.4. Comparison of mean pressure for polyethylene melts as a function of strain rate.

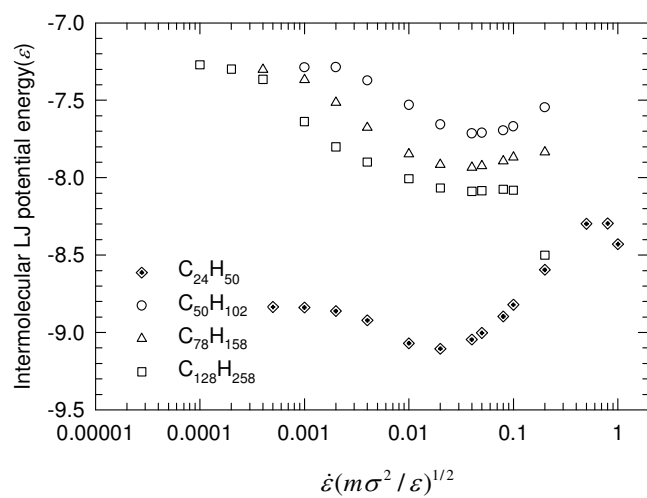
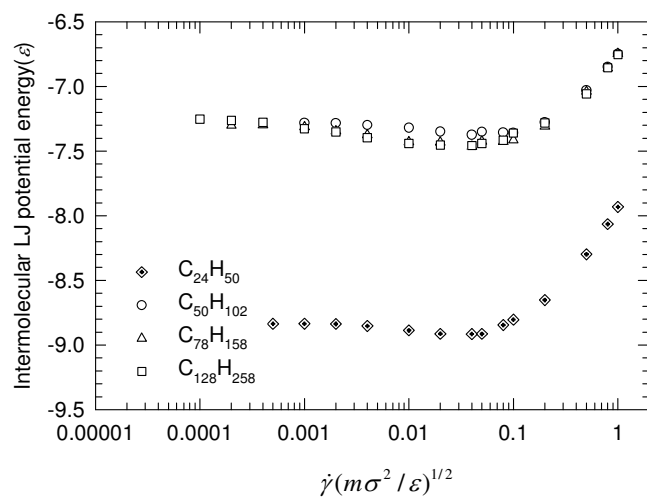


Fig. 4.1.5. The intermolecular LJ potential energy per united atom vs. strain rate.

$C_{128}H_{258}$  under PEF at the highest values of strain rate simulated, the intermolecular LJ energy begins to decrease again. It was speculated in Refs. [Baig *et al.*, 2005b, 2006b] that this behavior was due to the chains achieving full extension only at the very highest strain rates: once the chains are fully extended, the collisional effect is reduced since the fully stretched chains are not as sterically capable of having such strong collisional effects when they are all aligned in the flow direction. Hence atoms on different aligned molecules cannot move perpendicular to the molecular axis as readily to interact with atoms on neighboring chains. This explanation is consistent with the shear results of Fig. 4.1.5a, where no maximum appears in the intermolecular LJ energy at extremely high shear rates: in shear flow, the chains are not nearly as extended at high strain rates as they are in PEF—compare the ordinate scales in Figs. 4.1.2a and 4.1.2b.

Since  $\langle R_{ete}^2 \rangle$  and the mean-square chain radius of gyration,  $\langle R_g^2 \rangle$ , are closely related to the molecular conformations of the chains [Bird *et al.*, 1987; Kröger, 2005], each can provide clues as to the dynamics of the polyethylene liquids under flow. For  $C_{128}H_{258}$  under PEF, both  $\langle R_{ete}^2 \rangle$  and  $\langle R_g^2 \rangle$  increase rapidly at low elongation rates due to alignment and extension of the chains within the elongational field—see Fig. 4.1.2. At high elongation rates, the slopes of the  $\langle R_{ete}^2 \rangle$  and  $\langle R_g^2 \rangle$  profiles decrease significantly due to the increasing effect of intermolecular collisions. Under shear flow, the magnitudes of  $\langle R_{ete}^2 \rangle$  and  $\langle R_g^2 \rangle$  for  $C_{128}H_{258}$  also increase at low shear rates due to alignment and extension of the chains under the imposed shear field.



After that, however, these quantities attain their maximum values and slightly decrease at high shear rates due to chain rotation and tumbling.

This overall qualitative behavior of  $\langle R_g^2 \rangle$  under shear flow is very similar to that of  $C_{100}H_{202}$  reported by Moore *et al.* (2000). It can be explained by examining the bond-torsional and bond-stretching energies of Figs. 4.1.6a and 4.1.7a under shear flow. At the same critical value of the shear rate where the maximum occurs in  $\langle R_{etc}^2 \rangle$  and  $\langle R_g^2 \rangle$ , the bond-torsional energy begins to increase substantially. This is due to the increasingly significant role of chain rotation and tumbling. At the same time, the bond-stretching energy begins to decrease significantly, since the collisions require adjacent atoms in the same chain to synchronize their oscillations in the more fully extended chain conformation, thus lowering the amplitude of the vibrations and decreasing the bond-stretching energy. In other words, the chains become stiff, at least segmentally, at high shear rates, and thus the bonds cannot fluctuate far from their equilibrium bond lengths. Hence the molecular rotation becomes more difficult, and the local chain stiffness results in more snake-like rotational chain conformations.

The chain flexibility can be further examined as a function of strain rate in both shear and PEF, as in Fig. 4.1.6. As stated above, the bond-torsional interactions govern the global chain flexibility, whereas the bond-bending and bond-stretching interactions determine the short-range local chain flexibility. The behavior of the liquids under PEF is different than that of shear, which was described in the preceding paragraph. The bond-torsional energy decreases at low strain rates due to chain

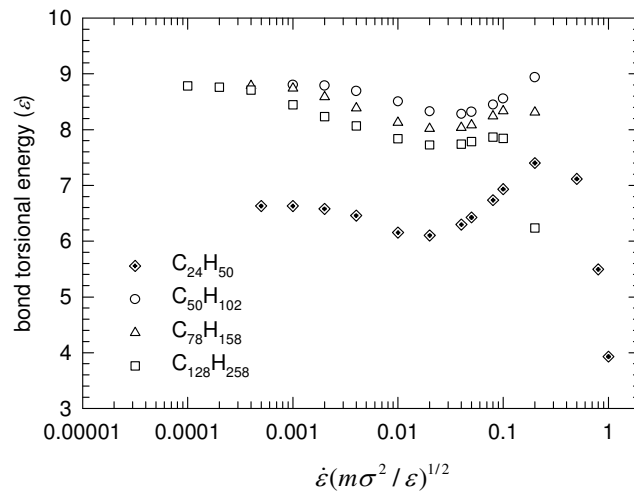
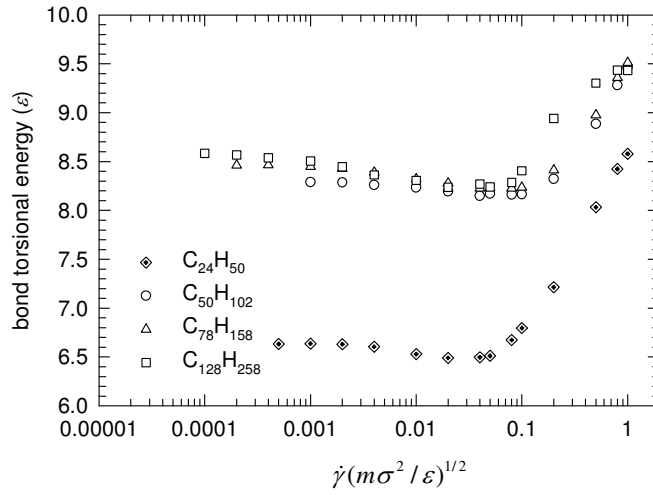


Fig. 4.1.6. The bond-torsional energy per mode vs. the strain rate.

alignment with the flow field, and then reaches a minimum value at intermediate strain rates for all polyethylene melts. This minimum value also is explained by the balance of the competing effects of chain alignment molecular collision for PEF. After a rather small increase in the torsional energy, as in shear, however, there occurs a dramatic drop at high strain rates for  $C_{24}H_{50}$  and  $C_{128}H_{258}$  under PEF. This is due to the reduction in the torsional energy required once the chains have become fully extended under PEF in their all *trans*-conformations, thus approaching the minimum energy condition. Under shear flow, the molecules never even approximate fully extended chains, partially due to their ongoing rotation, thus explaining the continuous increase in the bond-torsional energy in this flow field.

The bond-stretching interactions also contribute to the short-range local chain flexibility. The bond-stretching energy per mode as a function of strain rate is depicted in Fig. 4.1.7. After a region of remaining constant at low strain rates, the bond-stretching energy decreases monotonically as the strain rate increases, exhibiting a sudden drop in energy at high strain rates for each polyethylene melt. This sudden drop of the bond-stretching energy is understood by considering the chain flexibility, as in the previous articles [Baig *et al.*, 2005b, 2006b]. At high strain rates, the chains become stiff due to the sharp free energy difference between the all *trans*-conformational state and other states with lesser degrees of extension. Therefore, the intramolecular atomistic neighbors can only fluctuate to a small degree from their equilibrium bond lengths, as discussed earlier.

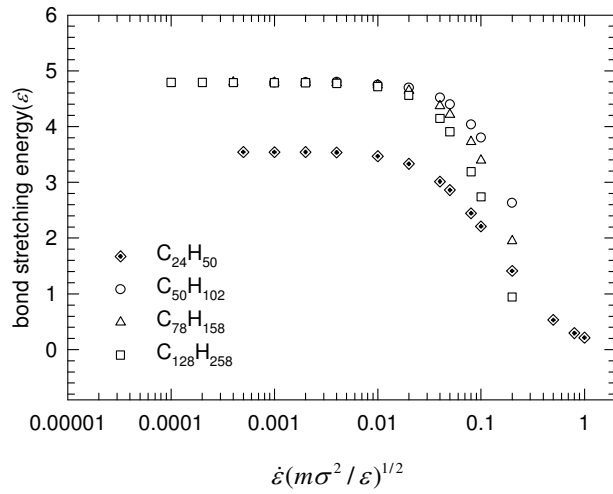
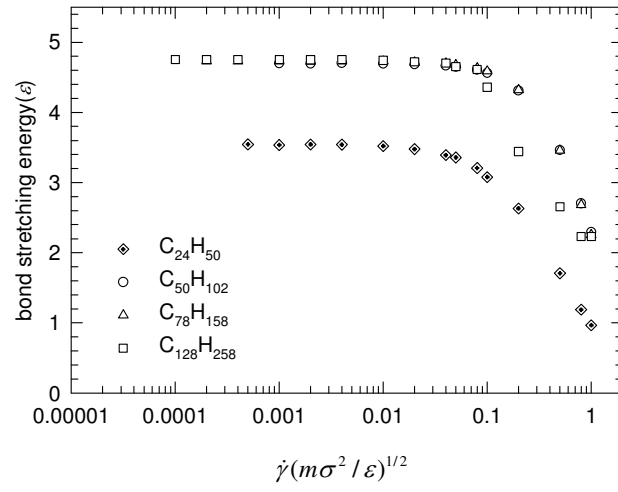


Fig. 4.1.7. The bond-stretching energy vs. the strain rate.

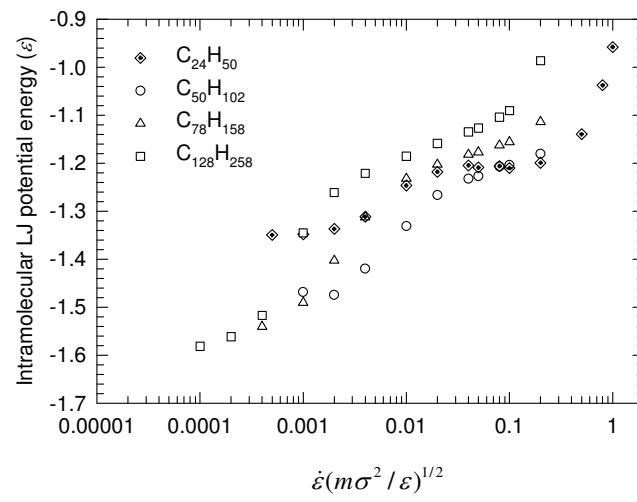
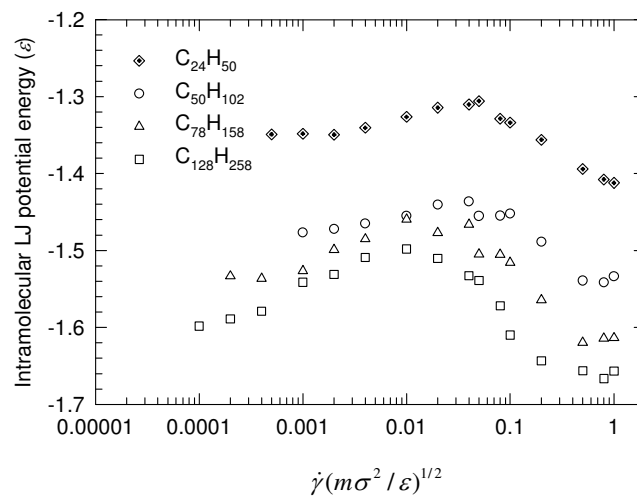


Fig. 4.1.8. The intramolecular LJ potential energy per (mode - 4) as a function of strain rate.

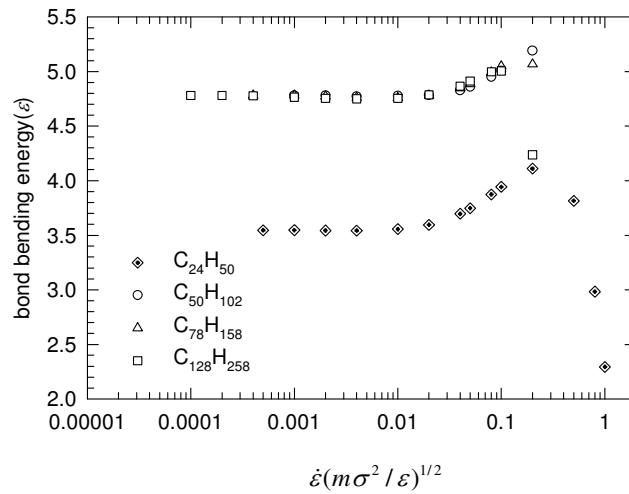
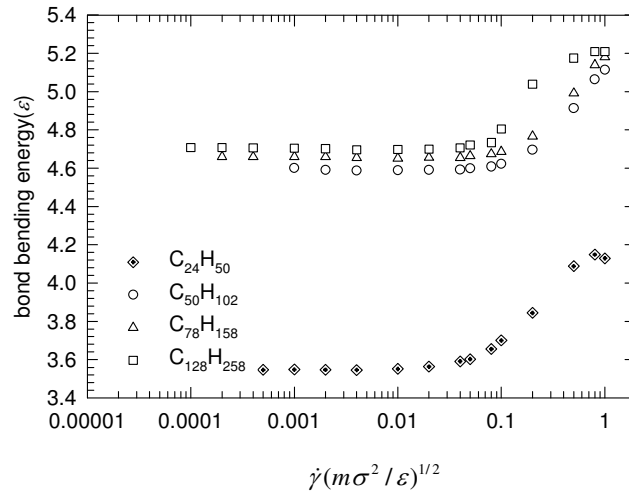


Fig. 4.1.9. The bond-bending energy per mode vs. the strain rate.

To augment our understanding of the intramolecular structure, the intramolecular LJ potential energy per mode versus strain rate was investigated using Fig. 4.1.8. As the flow strength increases, the chains will align on an averaged basis and extend to a greater degree. Therefore, the distance between neighboring atoms is longer than in the undeformed equilibrium state. This longer length between each atom causes the intramolecular LJ potential energy to increase; i.e., to become less negative. There appears to be a direct correlation between the intramolecular LJ energy and  $\langle R_{etc}^2 \rangle$ ,  $\langle R_g^2 \rangle$  for both shear and PEF. Under PEF, the chains continue to increase in length for all strain rates, and so the LJ energy continuously increases as well. Under shear, there is a maximum in the LJ profile that roughly corresponds to the critical shear rate where the chains attain their maximum extensions. As chain rotation and tumbling effects begin to dominate at high shear rates, the LJ energy decreases due to hairpin like rotational cycles, where neighboring atoms are actually closer together than under equilibrium conditions.

The bond-bending interactions also contribute to the short-range chain flexibility. The bond-bending energy per mode is depicted as a function of strain rate in Fig. 4.1.9. The overall behavior of the bond-bending energy is qualitatively similar to the bond-torsional energy displayed in Fig. 4.1.6. In shear, the bond-bending energy begins to increase at intermediate shear rate values due to the increasing extension of the chains into more *trans*-conformations. As more bonded atoms adopt *trans*-conformations, the bond-bending energy necessarily increases. Under PEF, however, again, the dramatic drop in the interaction energy, similarly to the bond-torsional

energy profiles, is observed. Again, this is due to a decrease in chain flexibility in the all *trans*-conformation, as the bond angles fluctuate to a smaller degree around their equilibrium values.

The flow-induced topological changes of the entanglement network accompanying the rheological and energetic/entropic behavior have been analyzed as well. Fig. 4.1.10 depicts a representative time-dependent variation of the contour length of an entanglement network divided by the number of chains (often called ‘primitive path length’),  $L_{pp}$ , during start up of flow for  $C_{78}H_{158}$ . This quantity exhibits an overshoot in concert with a stress overshoot during the onset of shear flow, and a monotonic increase toward its steady-state value under elongational flow. Note that the steady-state value of  $L_{pp}$  is much higher under PEF than shear, as intuitively expected—see Fig. 4.1.2. The elongational behavior is also rather intuitive; the chains extend monotonically after start-up toward their steady-state conformations. The damped oscillatory shear behavior is caused by the same physical mechanism that leads to a shear stress overshoot upon start-up of flow, and mirrors the behavior of the conformation tensor. If the time scale of the applied shear rate is large relative to the rotational relaxation time of the liquid (low shear rates), then the chains respond rapidly to the imposed flow field. Hence the convection term dominates the  $L_{pp}$  response. This produces a monotonic increase in  $L_{pp}$  toward its steady-state value, similarly to the extensional flow case of Fig. 4.1.10b. However, when the time scale of the shear flow is less than the fluid’s rotational relaxation time (high shear rates), the



relaxation term dominates the response of  $L_{pp}$  at long times until the attainment of steady state. This leads to the complex oscillatory behavior displayed on Fig. 4.1.10a:  $L_{pp}$  can be expressed in qualitative fashion by the functional form  $L_{pp} = f(t)\exp(-t/\lambda)$ , where  $f(t)$  is some monotonically increasing function of time. Therefore, at relatively small values of time,  $f(t)$  dominates the behavior of  $L_{pp}$ , whereas when  $t \rightarrow \lambda$ , the exponential relaxation term begins to affect the behavior. Hence the chains are over extended at low times due to the imposed shear field, and then relax to the steady-state conformations at long times. In the oscillatory behavior of Fig. 4.1.10a, this relaxational process results not only in overshoots, but undershoots as well, indicating that  $L_{pp}$  is a fairly dynamic system property.

Since these systems are not well entangled even in the equilibrium state, it is not possible to draw conclusions about the time-dependent behavior of ‘entanglement’ points, but the non-affine behavior of  $L_{pp}$  vs. time, as shown in Fig. 4.1.10, is certainly not a signature of low molecular weight polymers only. It is further evident from the data shown that the relaxation times characterizing the rheological and conformational properties have counterparts in the configurational properties (the entanglement network), and that the topological constraints imposed by the network will dominate conformational relaxation processes as soon as we exceed a critical molecular weight. Since the analysis of the statistical properties of entanglement networks scales (only) linearly with the system size, the current work provides reference data and some first

impressions about the dynamical behavior of the flow-induced network, which may be considered, from a thermodynamic perspective, as a relevant and slow variable for the theoretical description of polymer melts.

The steady-state values for various strain rates and chain lengths are presented in Figs. 4.1.11 and 4.1.12 for  $L_{pp}$ , as well as for the ‘number of entanglements,’  $Z_{coil}$ , and the ‘tube diameter,’  $a_{pp}$ , cf. Figs. 4.1.13-15. Each property was determined from single-chain averages, and each, except  $L_{pp}$ , was subjected to assumptions concerning the shortest path statistics. The variations of  $L_{pp}$  and  $a_{pp}$  with strain rate are qualitatively similar, and mirror the behaviors of the intramolecular LJ energy and  $\langle R_{ete}^2 \rangle$ --compare Figs. 4.1.11 and 4.1.14 with Figs. 4.1.2 and 4.1.8. Under shear, the contour length attains a maximum at the same value of shear rate where  $\langle R_{ete}^2 \rangle$  and the intramolecular LJ energy attain their maximum values. It thus seems reasonable to assert that the contour length increases at low shear rates where the intramolecular LJ energy decreases in strength, and decreases as this energy increases at higher shear rates, as discussed above. In PEF, the contour length increases monotonically with chain extension, as intuitively expected. The increasing tube diameter, evident in Fig. 4.1.14b, may be associated with the ordering of chains, which allows the maximization of the intermolecular distances along the primitive paths. As an additional interesting point, which may be entirely coincidental, the maxima under shear for both contour length and tube diameter correlate very closely with the critical shear rate at which the

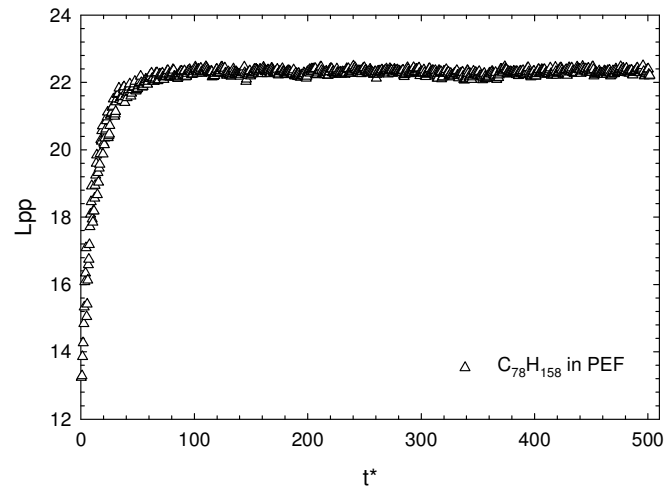
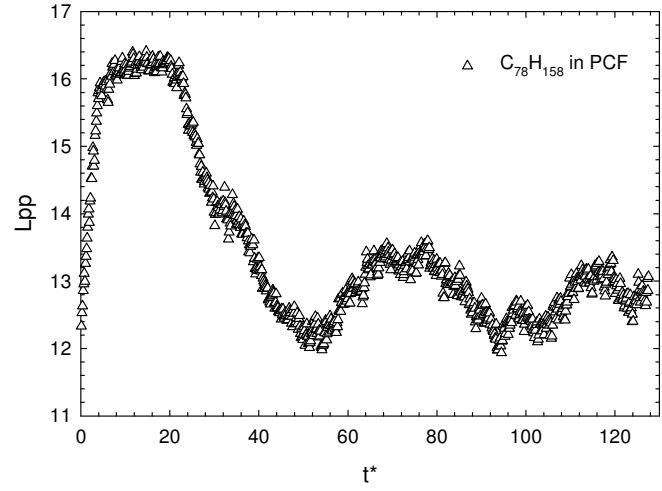


Fig. 4.1.10. Contour length of the primitive path,  $L_{pp}$  vs. time after start-up of flow for  $C_{78}H_{158}$ .

stress-optical relationship began to fail in a previous molecular dynamics study of polyethylene chains [Baig *et al.*, 2007]. A weak decrease of the value for the tube diameter at the largest elongation rate, and thus a weak maximum in Fig. 4.1.2b, may be observed if we would allow for density changes; the system tends to crystallize at about the largest simulated rate under constant pressure conditions, cf. [Ionescu *et al.*, 2006].

The ‘number of entanglements’  $Z_{coil}$  monotonically decreases with strain rate in both shear and PEF, as displayed in Fig. 4.1.13. This is very reasonable in that one would expect that  $Z_{coil}$  would decrease as the chains uncoil during extension. In shear, this decrease appears to be almost linear in shear rate, with a rather low value of the slope. This slow decrease is associated with the relatively low extension of the chains in shear flow, as well as their rotational motion. Although the chains extend more on average with increasing shear rate, thus reducing  $Z_{coil}$ , the rotation of the molecules tends to favor entanglement formation. This explains the slow decrease of  $Z_{coil}$  under shear when compared to PEF. Under PEF, the chains are readily extended, even at low strain rates, and so a dramatic drop, associated with disentanglement events, occurs in the value of  $Z_{coil}$  at low values of strain rate. For higher strain rates,  $Z_{coil}$  attains a plateau of very small magnitude, since further chain extension cannot produce any additional reduction in  $Z_{coil}$ . The decreasing  $Z_{coil}$  not only characterizes a loss of chain flexibility, but also the loss of ‘knot’ formation, albeit incomplete at the largest chain lengths.

It is also interesting to examine the behavior of contour length and tube diameter as functions of chain length under shear and PEF, as depicted in Figs. 4.1.12 and 4.1.15. As intuitively expected, both quantities increase monotonically with chain length under all conditions examined. For the contour length, the increase with chain length is much more dramatic under PEF than shear (see the respective ordinate scales in Fig. 4.1.12), which is again expected from the greater degree of extension in this flow field. The tube diameter displays similar qualitative behavior, and again increases much more dramatically in PEF than shear, due to the greater degree of chain alignment.

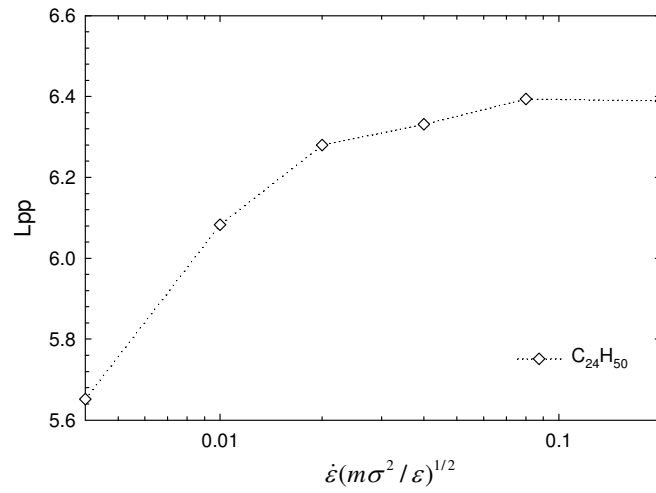
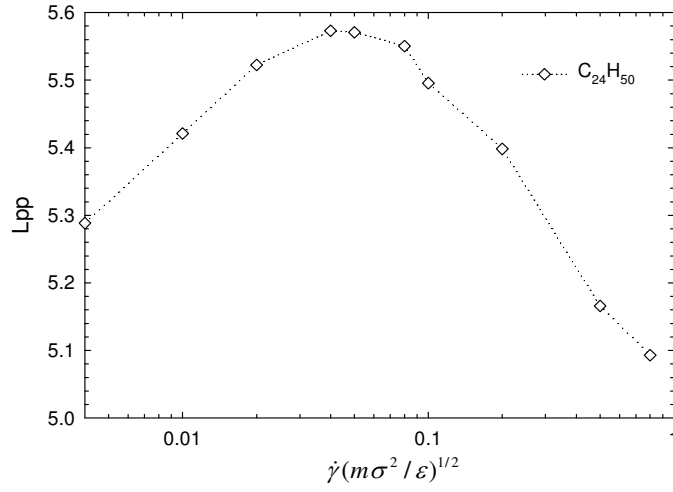


Fig. 4.1.11. Stationary values for  $L_{pp}$  vs. strain rate for  $C_{24}H_{50}$ .

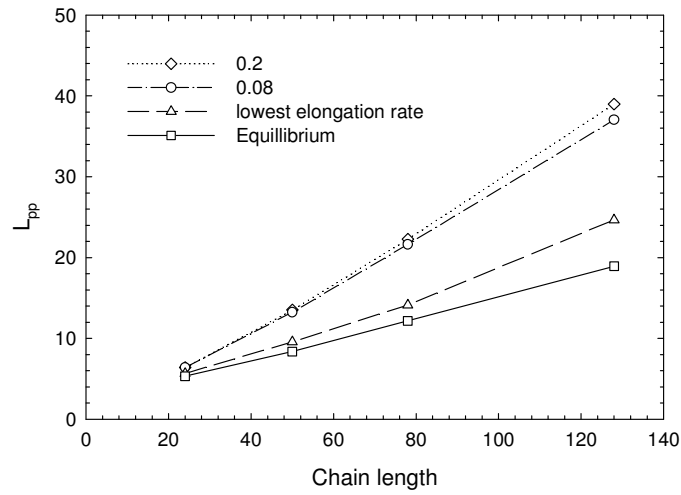
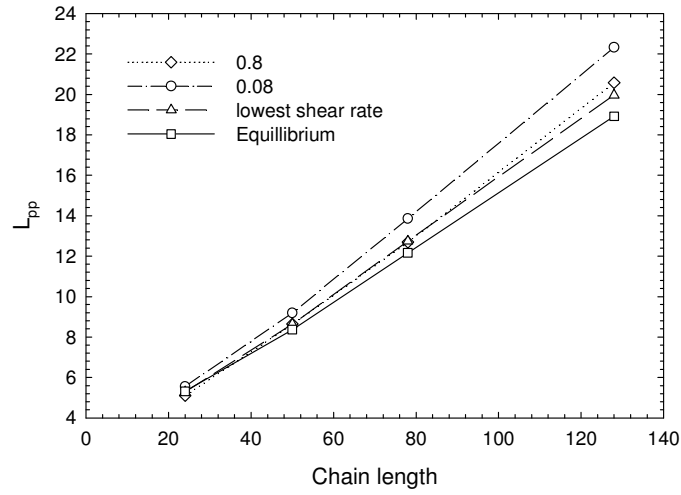


Fig. 4.1.12.  $L_{pp}$  vs. molecular weight for various strain rates.

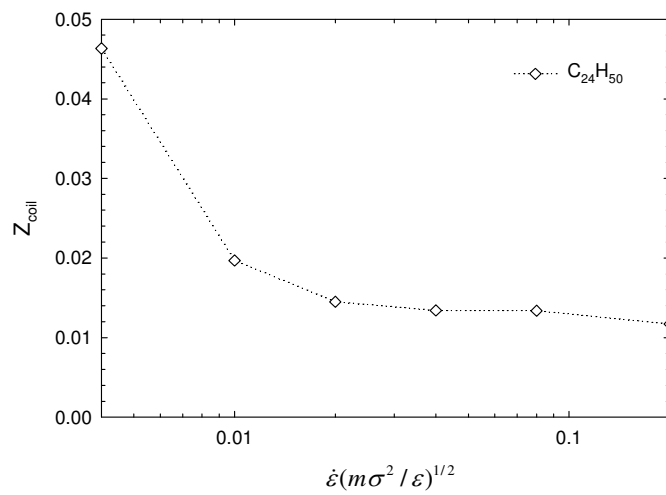
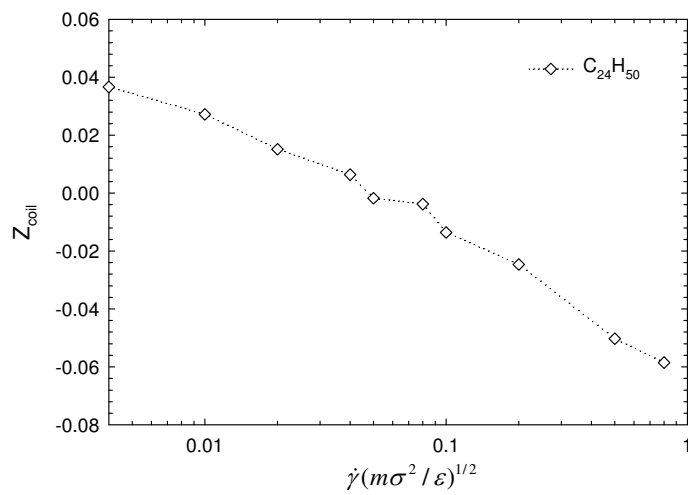


Fig. 4.1.13. 'Number of entanglements'  $Z_{coil}$  (assuming equilibrium statistics) vs. strain rate for  $C_{24}H_{50}$ .



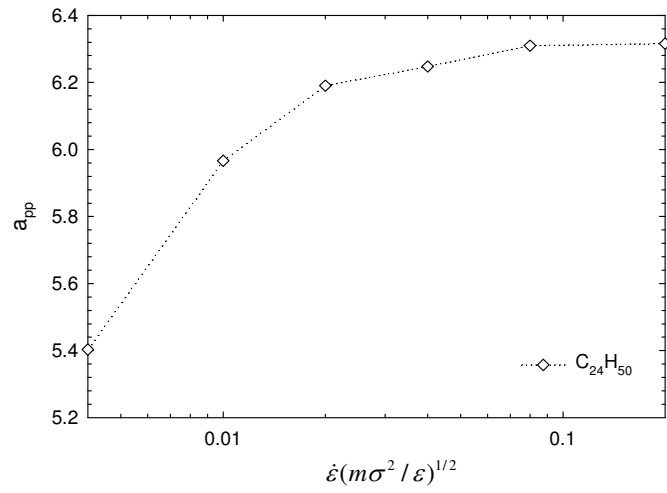
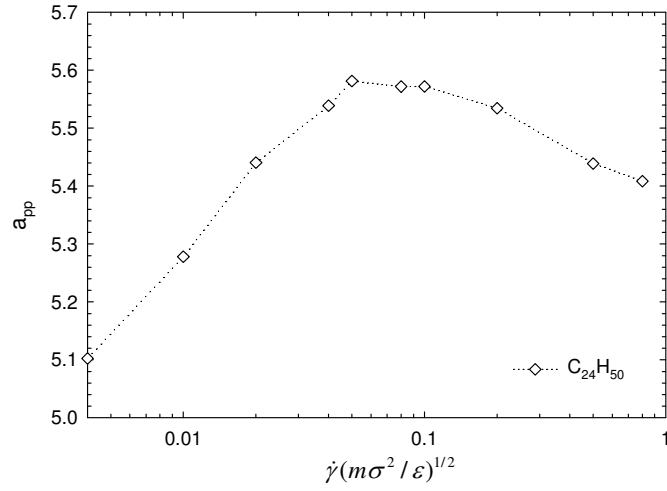


Fig. 4.1.14. 'Tube diameter'  $a_{pp}$  (assuming equilibrium statistics) vs. strain rate for  $C_{24}H_{50}$ .

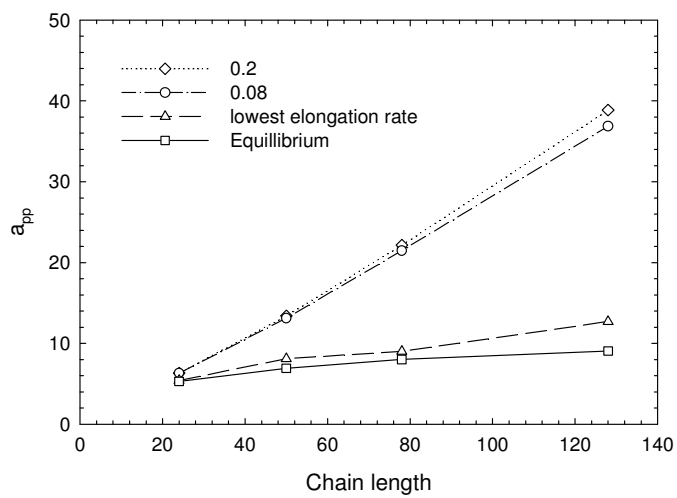
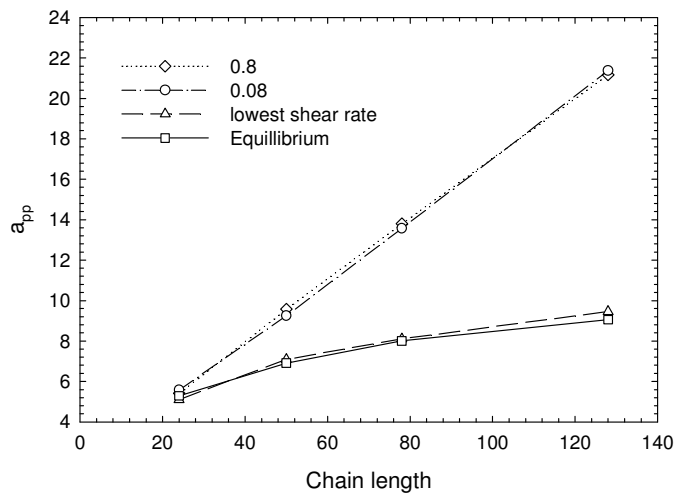
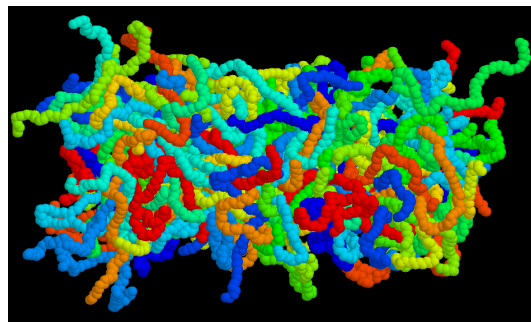


Fig. 4.1.15. Tube diameter  $a_{pp}$  vs. molecular weight for various strain rates.

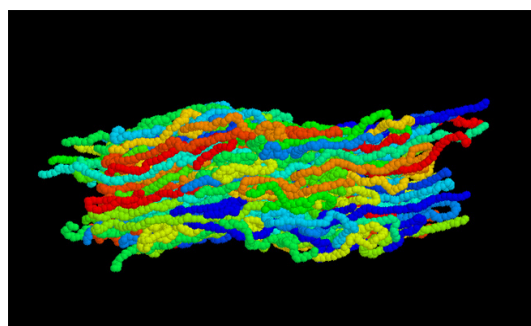
## 4.2 Visualization of conformational changes of linear short-chain polyethylenes under shear and planar elongational flows

Snapshots of  $C_{78}H_{158}$  under equilibrium, steady-state shear at a reduced shear rate of 0.8, and steady-state elongational flow at a reduced strain rate of 0.2 are displayed in Fig. 4.2.1. These values were so chosen for two reasons. First, they were the maximum values for each flow type which could be safely simulated without observing system size effects or thermostat artifacts. Second, these values correspond to equivalent rates of deformation, as quantified through use of the second invariant of the deformation rate tensor for an incompressible fluid,  $\text{tr}(\mathbf{D} \cdot \mathbf{D})$  [Bird *et al.*, 1987]. Here,  $\mathbf{D}$  is the symmetric contribution to the velocity gradient tensor, so that  $\text{tr}(\mathbf{D} \cdot \mathbf{D})$  for elongational flow at a given value of  $\dot{\epsilon}$  is four times larger than  $\text{tr}(\mathbf{D} \cdot \mathbf{D})$  for shear flow at an equivalent value of  $\dot{\gamma}$ ; i.e.,  $\text{tr}(\mathbf{D} \cdot \mathbf{D}) = \dot{\gamma}^2/2$  and  $2\dot{\epsilon}^2$ .

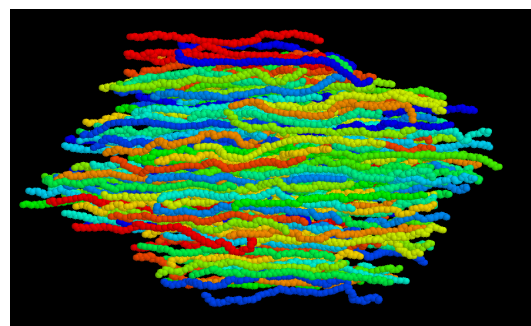
In Fig. 4.2.1, it is evident that the structure and orientation of  $C_{78}H_{158}$  is substantially different under the three conditions. In Fig. 4.2.2(c), 4.2.3(c), and 4.2.4(c), the same snapshots are displayed rendering all but ten random chains invisible, so that a greater degree of clarity is achieved with respect to the individual molecular structure. In Figure 4.2.2, snapshots of each of the four liquids ( $C_{24}H_{50}$ ,  $C_{50}H_{102}$ ,  $C_{78}H_{158}$ , and  $C_{128}H_{258}$ ) are displayed at equilibrium. Figs. 4.2.3 and 4.2.4 display a random ten chains for the same fluids under steady-state shear and steady-state elongation, respectively.



(a)



(b)



(c)

Fig. 4.2.1. All chains of  $C_{78}H_{158}$  at equilibrium (a), reduced shear rate of 0.8 (b), and elongation rate of 0.2 (c).

The following trends are evident from Fig. 4.2.2. Under equilibrium conditions, the chains are randomly oriented, in terms of an end-to-end vector drawn between the beads on the chain ends. This vector obeys a well-defined Gaussian distribution characterizing its magnitude and direction. The mean-square of the chain end-to-end vector,  $\langle R_{ete}^2 \rangle$ , quantifies the average conformation of the ensemble of chains. For example, the quantity  $\langle R_{ete}^2 \rangle^{1/2}$  of C<sub>128</sub>H<sub>258</sub> under equilibrium conditions is 50.66 Å, whereas the length of the fully stretched chain in the *all-trans*-conformation is 164 Å. As chain length increases, the magnitude of the root mean square, end-to-end vector,  $\langle R_{ete}^2 \rangle^{1/2}$ , increases according to the well-known scaling factor of  $\sqrt{n}$  [Treloar, 1975; Doi and Edwards, 1986],  $n$  being the number of bonds in a single chain (see Table 4.2.1); however, the orientation of the chains remains random. Also, although the molecules are relatively uncoiled at low chain lengths, as the molecular weight of the compound increases, the chains increasingly assume random coil conformations. The ratio of  $\langle R_{ete}^2 \rangle$  with respect to the mean square of the radius of gyration,  $R_g$ , decreases toward the theoretical value of six for long polymer chains; however, it will not plateau at this value until  $n \approx 140$  [Foteinopoulou *et al.*, 2006]. The step length,  $\frac{\langle R_{ete}^2 \rangle^{1/2}}{\sqrt{n}}$ , increases from 4.21 Å to 4.50 Å as the chain length increases, indicating a fairly flexible chain.

The orientations and conformations of the chains are determined by entropic considerations alone. Increasing the chain length renders accessible many more possible chain conformations, thus increasing the intrachain entropy. The entropy increases with increasing chain length according to the expression [Treloar 1975; Doi and Edwards, 1986]

$$S = c - k_B b^2 \langle R_{ete}^2 \rangle, \quad (56)$$

where  $c$  is an arbitrary constant,  $b^2 = 3/(2nl^2)$ , and  $l$  represents the bond length.

Values of topological characteristic indicators such as shortest primitive length, tube diameter, etc. are displayed in Table 4.2.2 at equilibrium. The least primitive path displays its minimal value (with respect to an applied flow field) for all chain lengths, as does the tube diameter.  $L_{pp}$  is generally greater than or equal to the value of  $\langle R_{ete}^2 \rangle^{1/2}$  for each chain, since the end-to-end vector only quantifies the distance between the chain ends. As the chain length increases, the chains assume more randomly coiled configurations, and consequently the difference between these two quantities magnifies; i.e.,  $L_{pp}$  grows faster than  $\langle R_{ete}^2 \rangle^{1/2}$ . For the shorter chains, the tube diameter is of the same order as the primitive path length; this is because of the relatively extended chain configurations, which are relatively stiff at low values of  $n$ . It seems reasonable that these shorter chain liquids would not form the tortuous, tube network structures of the longer chain liquids, which have greater entropic degrees of freedom for configurational changes. Therefore, the tube diameter decreases relative to the contour length as the chain length increases.

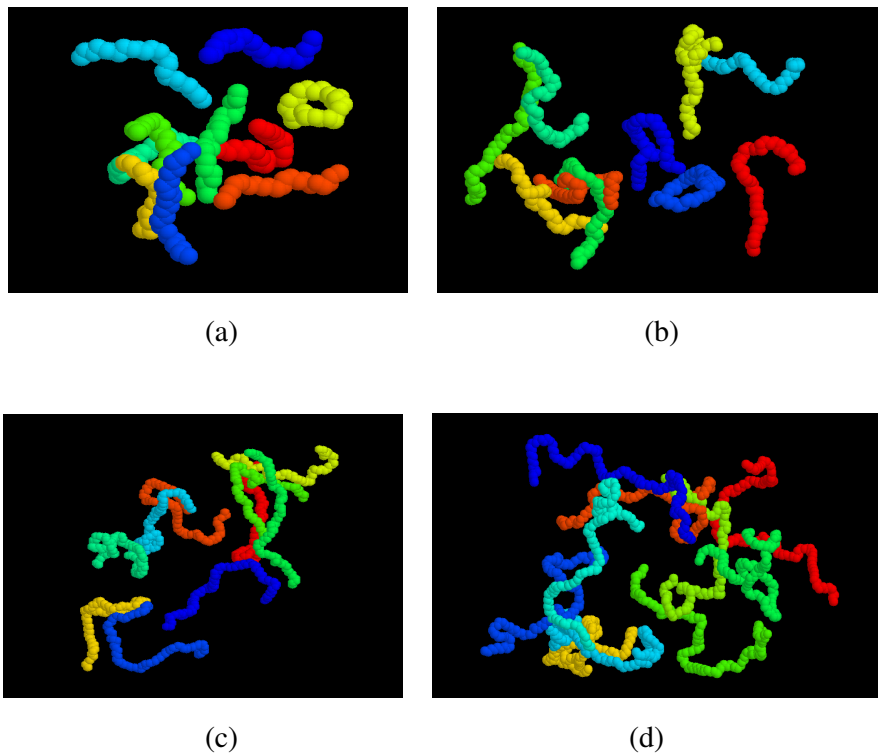


Fig. 4.2.2. Ten random chains of  $C_{24}H_{50}$  (a),  $C_{50}H_{102}$  (b),  $C_{78}H_{158}$  (c), and  $C_{128}H_{258}$  (d) at equilibrium.

Table 4.2.1 Statistical measures of polymer configurations for all four liquids at equilibrium, in shear, and in PEF. Note that all liquids were simulated at 450 K, except for C<sub>24</sub>H<sub>50</sub>, which was simulated at 333 K.

Liquid	$\langle R_{ete}^2 \rangle^{1/2}$	$\langle R_{ete}^2 \rangle^{1/2}$	$\langle R_{ete}^2 \rangle^{1/2}$	$\langle R_{ete}^2 \rangle^{1/2}$	$\langle R_{ete}^2 \rangle / \langle R_g^2 \rangle$	Step Length
	(Å)	(Å)	(Å)	(Å)		(Å)
	Equilibrium	Shear(0.8)	PEF(0.2)	Full extension	Equilibrium	Equilibrium
C <sub>24</sub> H <sub>50</sub>	20.20	23.13	25.06	29.7	8.44	4.21
C <sub>50</sub> H <sub>102</sub>	29.72	35.90	52.92	63.3	7.18	4.25
C <sub>78</sub> H <sub>158</sub>	38.63	52.76	87.19	99.4	6.84	4.40
C <sub>128</sub> H <sub>258</sub>	50.66	81.91	149.48	164.0	6.60	4.50



Table 4.2.2 Topological characteristic quantities at equilibrium for each liquid: contour length, tube diameter, and number of entanglements [Section 4.1; Foteinopoulou *et al.*, 2006].

Liquid	$L_{pp}$ (Å)	$a_{pp}$ (Å)	$Z_{coil}$
$C_{24}H_{50}$	20.4	16.7	0.04
$C_{50}H_{102}$	30.2	22.5	0.9
$C_{78}H_{158}$	41.1	28.2	1.6
$C_{128}H_{258}$	58.9	35.2	2.5

However, the shorter chain liquids form tube arrays more readily than the longer chain liquids, since they are relatively more extended than the longer chains and exhibit fewer entanglements. This explains why  $a_{pp}$  decreases with diminishing chain length, whereas the density increases.  $Z_{coil}$  increases steadily with chain length, as one would intuitively expect, and for long enough chains this increase is approximately linear [Foteinopoulou *et al.*, 2006].

In Fig. 4.2.3, snapshots of the ten random chains for each liquid under steady-state shear are displayed at a reduced shear rate of 0.8. In these figures, flow is in the horizontal direction and the gradient of velocity is in the vertical direction. By comparing Fig. 4.2.2 with Fig. 4.2.3, it is evident that the presence of a strong shear flow distorts the equilibrium configurations of the chains: there is a preferential orientation (on average) of the chains with respect to the flow field, and the chains are more highly extended. With regard to the chain end-to-end vector orientation, it is well known under shear flow that the average orientation decreases from 45 degrees relative to the direction of flow at low shear rates, to only a few degrees north of the flow direction at high shear rates [Baig *et al.*, 2005b; Bird *et al.*, 1987; Morriss *et al.*, 1991]. This high shear rate behavior is fully depicted in the snapshots of Fig. 4.2.3. The orientation angle is generally a function of the shear rate, and decreases as shear rate increases [Baig *et al.*, 2007; Cui *et al.*, 1996; Moore *et al.*, 2000]. For these high strain rates, the preferred orientation angle is very nearly parallel to the direction of flow. For example the C<sub>50</sub>H<sub>102</sub> displays an ensemble average orientation angle of five degrees [Baig *et al.*, 2007].

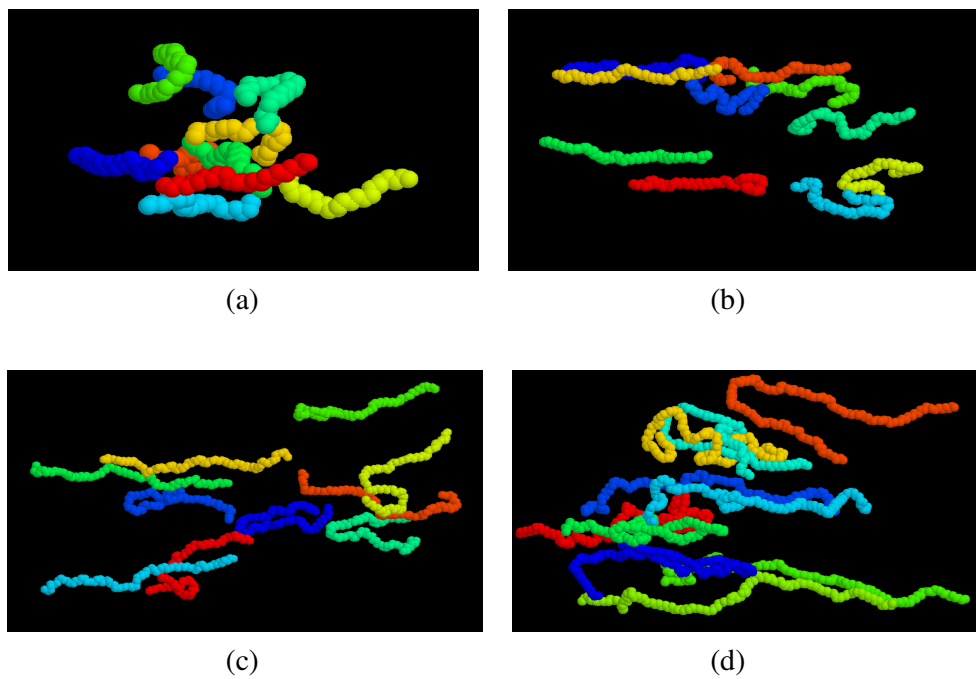


Fig. 4.2.3. Ten random chains of  $C_{24}H_{50}$  (a),  $C_{50}H_{102}$  (b),  $C_{78}H_{158}$  (c), and  $C_{128}H_{258}$  (d) at a reduced shear rate of 0.8.

The configurations of the individual chains have also been altered by the shear flow: the molecules are preferentially stretched in the appropriate direction relative to the direction of flow (see the preceding paragraph). The longer the chain, the greater the degree of extension that manifests. On account of the vorticity of the macroscopic flow field, the molecules quasi-periodically rotate in the clockwise direction, which is also evident in the figure as some molecules are caught in mid rotation. Still, the molecules are not on average even approximately fully extended. For example, the value of  $\langle R_{ete}^2 \rangle^{1/2}$  of  $C_{128}H_{258}$  under shear, 81.91 Å, is larger than the equilibrium value of 50.66 Å, but much smaller than that of the fully *trans*-conformation, 164 Å.

These graphics also provide a visual understanding of polymer shear-thinning behavior under flow. The preferential alignment of the long chains under flow conditions allows greater freedom of motion along the flow direction than is possible in a randomly oriented sample. Thus at low shear rates, the stress scales linearly with the applied strain rate; however, as an increasing number of chains orient preferentially nearly along the flow direction, a relative stress reduction occurs as the chains are able to glide by each other more freely. In previous studies [Baig *et al.*, 2005b, 2006b; See also Section 4.1], it was observed that weakened intramolecular Lennard-Jones interaction energies between chain atoms and stronger intermolecular LJ energies occurred as a result of the chain unfolding (reducing the number of interacting intramolecular pairs) and alignment with other chains (increasing the number of interacting intermolecular pairs). The ten random chains under an elongational flow of

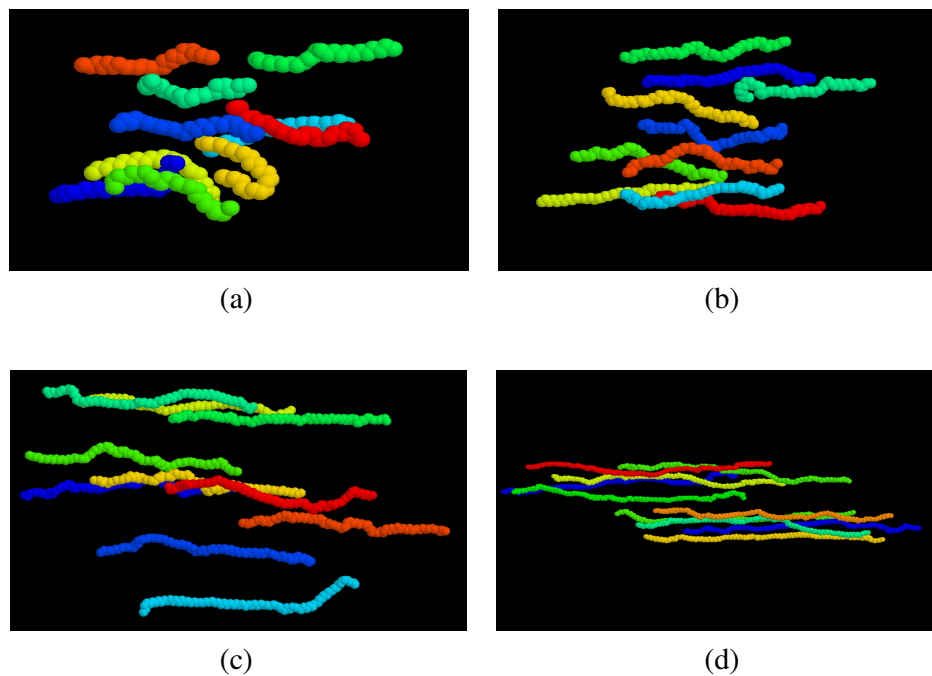


Fig. 4.2.4. Ten random chains of  $C_{24}H_{50}$  (a),  $C_{50}H_{102}$  (b),  $C_{78}H_{158}$  (c), and  $C_{128}H_{258}$  (d) at reduced shear rate of 0.2.

dimensionless strain rate 0.2 are displayed in Fig. 4.2.4. The axis of extension lies in the horizontal direction, and the axis of compression lies in the vertical direction. From Fig. 4.2.4, it is clear that the chains of all four liquids align on average with the axis of extension. However, it is also apparent that the relative degree of extension of the chains increases dramatically with chain length. Since elongational flow is vorticity-free, the occasional rotation of the molecules evident in Fig. 4.2.3 is rarely observed. Also, the degree of orientation (i.e., the number of molecules near to the preferred direction) is substantially greater than in the shear flow, and the preferred direction is always in the direction of extension. As the chain length increases, the chains become virtually fully extended: e.g., the value of  $\langle R_{ete}^2 \rangle^{1/2}$  of C<sub>128</sub>H<sub>258</sub> under PEF, 149.48 Å, is larger than that under shear, 81.91 Å, and approaches that of the fully *trans*-conformation, 164 Å. See Table 4.2.1 for a comparison of various statistical quantities for equilibrium and under shear and PEF for all of the simulated liquids.

Tension-thinning behavior is also observed in these liquids [Baig *et al.*, 2006a]. Fig. 4.2.4 provides qualitative information regarding the relative stress reduction on account of chain alignment in the direction of flow. As was the case with shear-thinning behavior, increasing elongation rate leads to an increase in the number of chains aligned with respect to the direction of flow, which in turn results in a decrease of the relative elongational stress. Even though the quantitative change of the intermolecular and intramolecular energies is very different between shear and PEF,

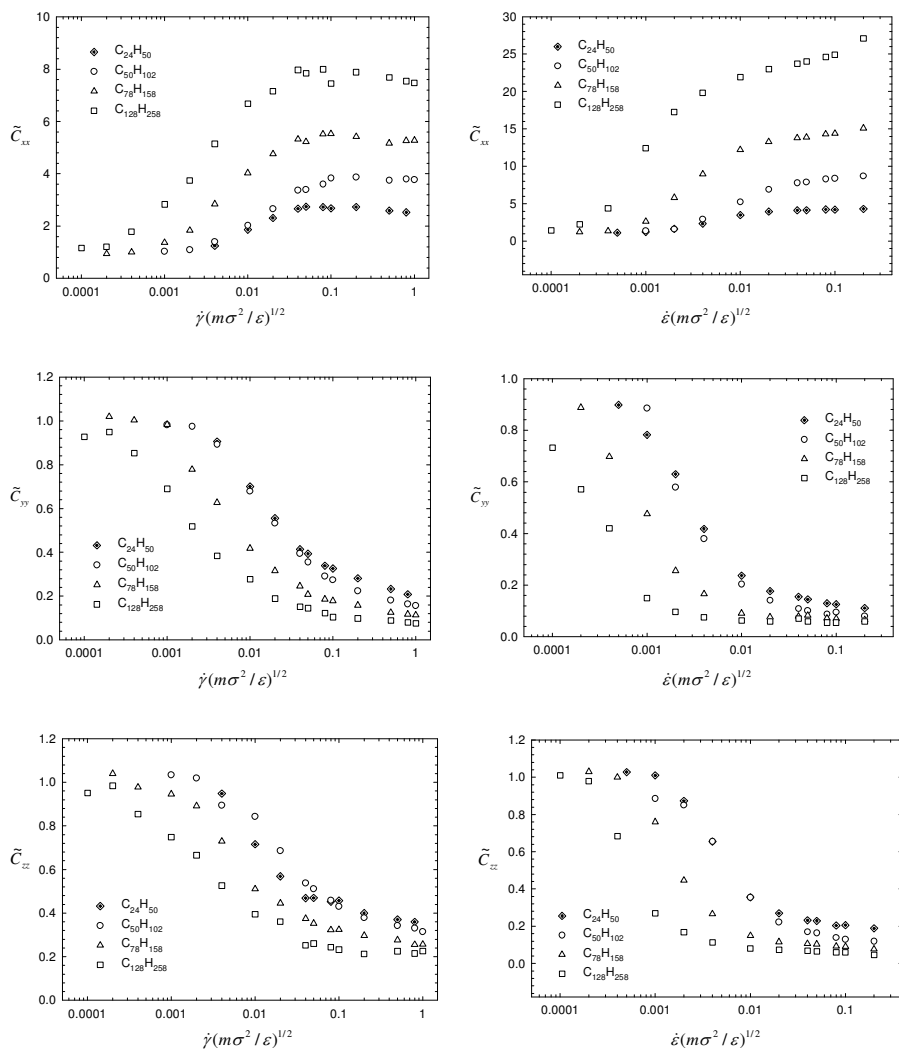


Fig. 4.2.5. Conformation tensor components of  $C_{24}H_{50}$ ,  $C_{50}H_{102}$ ,  $C_{78}H_{158}$ , and  $C_{128}H_{258}$  under shear (left column) and PEF (right column).

the changes of these energies is very similar qualitatively, and the same physical explanations apply to the liquids under PEF.

The average extension of the polyethylene chains can be quantified through the dimensionless conformation tensor defined in Eqn. (47). In Fig. 4.2.5, the diagonal components of the dimensionless conformation tensor are plotted under shear and PEF as functions of strain rate, and the trace is directly related to  $\langle R_{ete}^2 \rangle$ . Here  $x$  is the flow direction,  $y$  is the gradient or compression direction, and  $z$  is the neutral direction. Under quiescent conditions, this tensor is the unit tensor. It is evident from these plots that the chains undergo a dramatic extension in both types of flow at intermediate strain rates, although the degree of extension under PEF is much more severe. Note that in both cases, the molecules extend along the flow direction, and compress along the other two directions increasingly with increasing strain rate. The snapshots of Figs. 4.2.3 and 4.2.4 were taken at the highest values of the strain rates in Fig. 4.2.5.

The distribution of chain conformations and the preferred direction of orientation can be quantified using the Eigenvalues and Eigenvectors of the conformation tensor. In Fig. 4.2.6, the circles and ellipsoids represent the distributions of the chain extensions and orientations about the flow direction at various strain rates. For shear flow, the dimensionless shear rates were 0.0004, 0.08 and 0.8, used and for elongational flow the dimensionless elongation rates were 0.0004, 0.08 and 0.2 used. The first column in both rows is the equilibrium condition. As expected, at equilibrium all Eigenvalues of the conformation tensor are identical, implying an isotropic distribution of chain end-to-end vectors with a well-defined



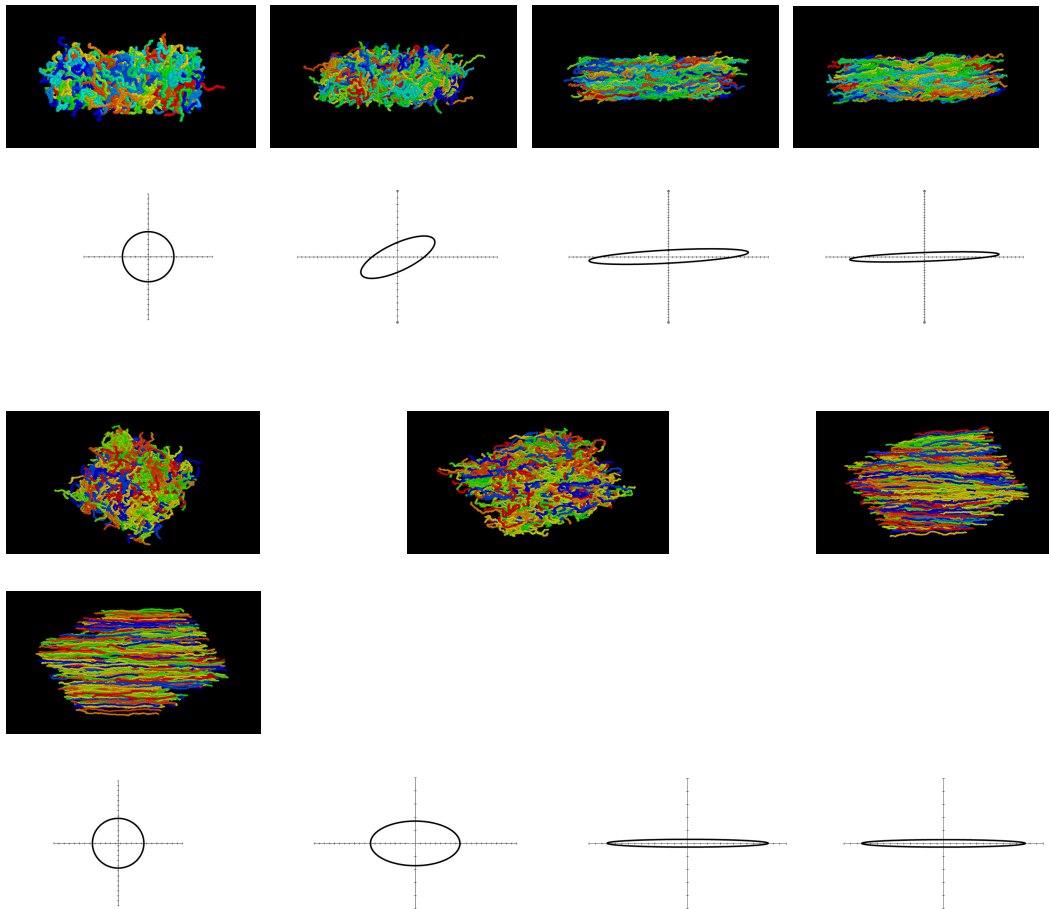


Fig. 4.2.6. Snapshots of the molecular structure under shear (upper row) and PEF (bottom row) and the corresponding distribution functions as determined by the Eigenvalues and Eigenvectors of the conformation tensor. Under shear, the depictions are for reduced shear rates of 0.0, 0.0004, 0.08, and 0.8, respectively. Under PEF, the snapshots are for reduced elongation rates of 0.0, 0.0004, 0.08, and 0.2, respectively.

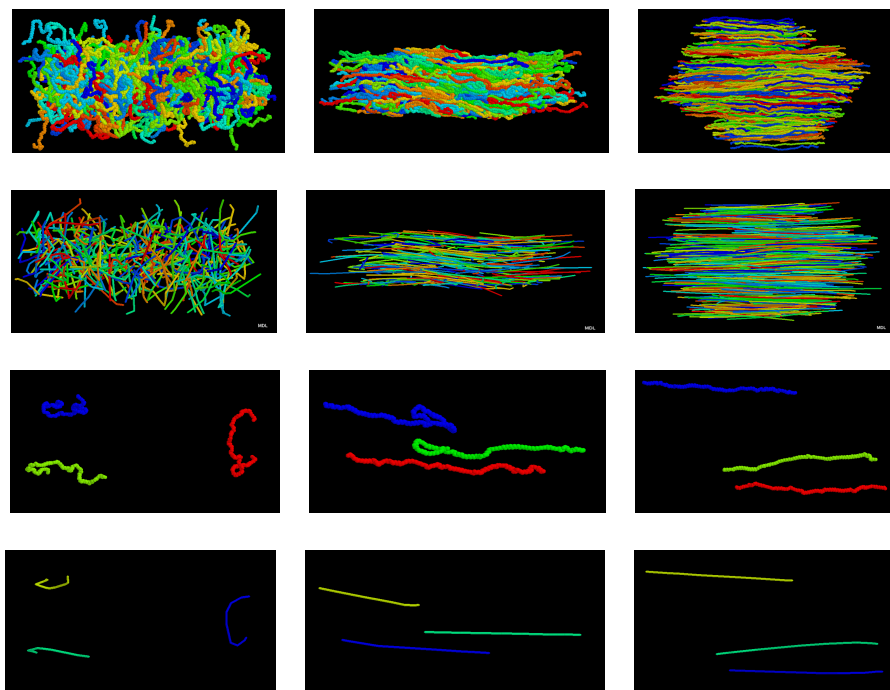


Fig. 4.2.7. Projections of atomistic chain structure of  $C_{128}H_{258}$  onto shortest primitive path. The first column depicts the equilibrium structure, the second column displays the shear structure, and the third column presents the PEF structure. The first row shows the full chain structures corresponding to Fig. 4.2.1. The second row displays the entanglement networks of the three cases. The third and fourth rows depict the same as above but for only three random chains of the overall liquid system presented in the first two rows.

average magnitude. Under shear flow, the distribution narrows and orients toward the flow direction as the shear rate is increased. Notice that the orientation angle decreases with shear rate relative to the direction of flow. Here, the preferred direction of orientation is quantified by the Eigenvector of the primary Eigenvalue. Under PEF, the distribution becomes much narrower than for shear flow, and always points in the flow direction.

In Fig. 4.2.7, the entanglement network of the  $C_{128}H_{258}$  atomistic chain and its shortest primitive path is presented at equilibrium (first column), under shear (second column), and under PEF (third column). The first row is the full atomistic chain system structure, as illustrated in previous figures. The second row presents the full entanglement structure as obtained from the Z-code of Kröger *et al.* (2002, 2005, 2006). The third row depicts three random chains for easy visualization, and the bottom row presents the primitive paths for the same three chains. Note the coarse graining of the atomistic chain with many degrees of freedom onto a chain composed of the primitive paths between entanglements bearing much fewer degrees of freedom. At equilibrium, the primitive path length is relatively large as compared to  $\langle R_{ete}^2 \rangle^{1/2}$ , but this difference diminishes as the chains stretch in response to the imposed flow field. This behavior is depicted in Fig. 4.1.12.

As the strain rate increases, the degree of extension of the chains under both shear and PEF increases, thus raising significantly the length of the shortest primitive path. Indeed, under PEF at a very high strain rate, the primitive path is essentially equivalent to the fully extended chain length. Consequently, the number of

entanglements decreases as the strain rate increases due to the unraveling of the chains, as might be expected, and the reptation tube diameter grow dramatically, as depicted in Fig. 4.1.15. Visually, it is also apparent from the snapshots of Fig. 4.2.7 that the tube length and diameter increase with increasing strain rate, thus allowing easy conceptualization of the strain-thinning behavior observed in these fluids: as the reptation tube lengthens, the chains are able to move axially with greater freedom, which manifests in lower relative stress between the atomistic constituents.

Figs. 4.2.8 and 4.2.9 present the transient behavior of  $C_{50}H_{102}$  under start-up conditions (from equilibrium) of high strain rate shear and PEF (dimensionless shear rate of 0.8 and elongation rate of 0.2). The arrow is an imaginary visualization of the rotational macroscopic flow field, as quantified by the vorticity vector of the shear field,  $\omega = -\frac{1}{2}\nabla \times \mathbf{v}$ , where the vector  $\omega$  quantifies the macroscopic angular velocity. Note that this can be quite different than the rotational rates of the individual atomistic chains. For shear flow, the time interval between each snapshot was 4.62 ps and the total time for one rotation was 36.96 ps. Under PEF, the time interval between each snapshot was 1.616 ps, with the exception of the last one, which was chosen at the starting point of the next applications of the KRBC ( $t_p = 11.319$  ps). The imaginary box depicts the macroscopic behavior of the simulated liquid. It expands in the flow direction at the rate  $x(t) = x \exp(\dot{\epsilon}t)$ , and contracts at the rate of  $y(t) = y \exp(-\dot{\epsilon}t)$ , according to the theory of macroscopic fluid dynamics.

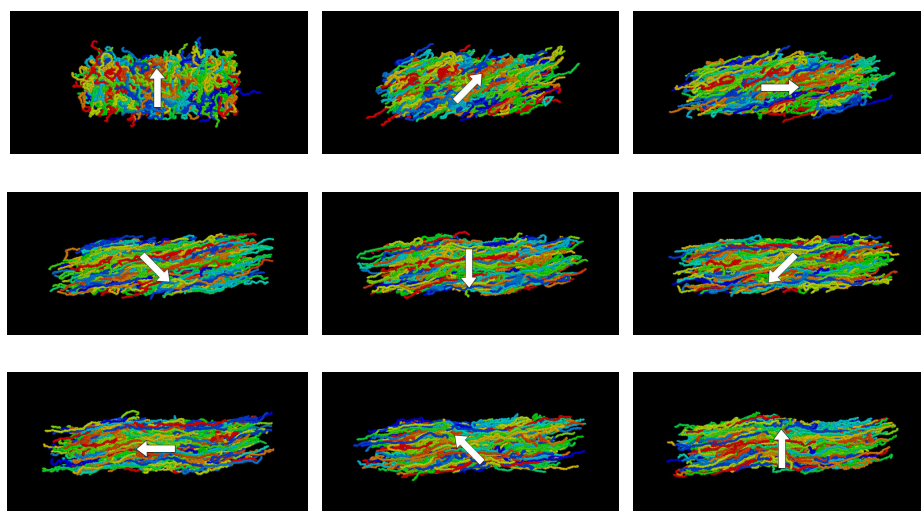


Fig. 4.2.8. Snapshots of the  $C_{50}H_{102}$  liquid undergoing shear at a reduced shear rate of 0.8. The shear flow is applied at time zero, and each successive frame is taken at an interval of 4.62 ps. The superimposed arrow indicates the macroscopic rotation of the fluid.

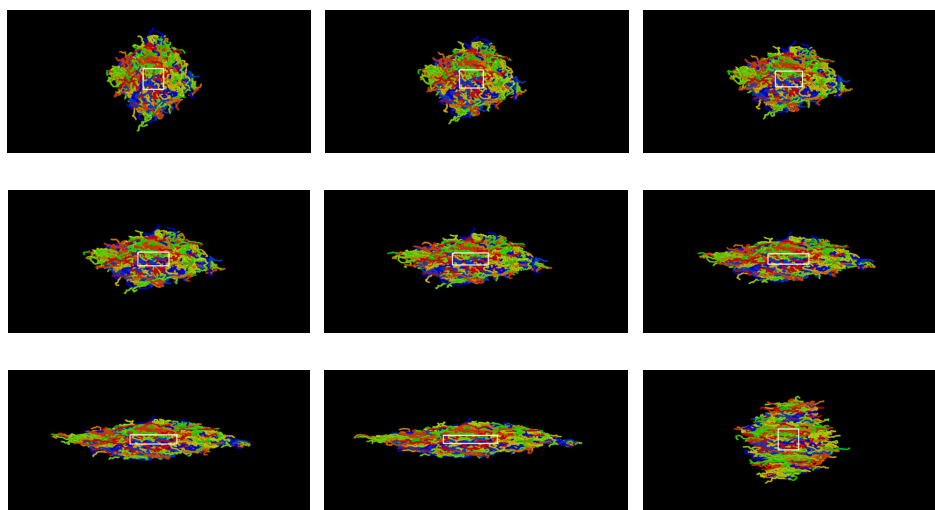


Fig. 4.2.9. Snapshots of the  $C_{50}H_{102}$  liquid undergoing PEF at a reduced strain rate of 0.2. The elongational flow is applied at time zero, and each successive frame is taken at an interval of 1.616 ps. The superimposed box indicates the macroscopic extension of the fluid.

### 4.3 Comparison of single chain dynamics at atomistic and mesoscopic levels

Nonequilibrium molecular dynamics (NEMD) simulations of linear  $C_{78}H_{158}$  liquids were conducted at the fine-grained atomistic level, and the BD simulations were performed using a dilute solution of bead-rod chains, which was generated using the atomistic-scale information via a straightforward coarse-graining procedure in Section 3.2. Note that one can refer to Section 3.1-2 for the details of the NEMD and BD simulations. The atomistic-level simulations allow a direct investigation to be made of the individual chain dynamics of the linear polyethylene chains, and hence into the microscopic origins of macroscopic rheological properties. Comparison between NEMD and BD simulations allows assessment of the differences between the dynamics of individual molecules that constitute dense liquids with respect to the corresponding dynamics of the same chains in dilute solution.

A plot of the mean-squared, end-to-end vector,  $\langle R_{ete}^2 \rangle$ , versus  $Wi$  is displayed in Figure 4.3.1. (Note that the error bars in all cases of the atomistic simulation data presented in the figures below are approximately equal to the sizes of the symbols themselves.) This quantity provides a determination of the absolute extension of the molecules. At low values of  $Wi$ ,  $\langle R_{ete}^2 \rangle$  assumes its quiescent value of  $1500 \text{ \AA}^2$ . As  $Wi$  approaches unity,  $\langle R_{ete}^2 \rangle$  begins to increase as the chain molecules begin to extend due to the hydrodynamic forces imposed by the shear field. In this  $Wi$  regime, the

free energy change of the fluid, relative to its equilibrium value, is dominated by the entropic configurational reduction as the molecules extend, thereby drastically diminishing the number of allowable configurations of the chains' constituent atomic units. Once  $Wi$  increases beyond unity, the nonlinear viscoelastic regime begins, wherein the timescale of the shear flow becomes smaller than the Rouse time. As  $Wi$  increases from a value of 1 to about 40, a very dramatic increase is observed in  $\langle R_{ete}^2 \rangle$ , which has traditionally been used to explain the onset of shear-thinning behavior in polymeric liquids beyond a  $Wi$  of unity; i.e., the deformation and preferential orientation of the chains relative to the flow direction relieves some of the hydrodynamic stress imparted to the molecular segments by the shear field. This result in a value of the shear stress that increases slower than the kinematics of the shear field would suggest.

The  $\langle R_{ete}^2 \rangle$  curve in Figure 4.3.1 begins to approach a maximum at a  $Wi$  value of approximately 50. This behavior is unexpected based upon the predictions of bulk-averaged rheological theories, which mandate that the chain extension should either increase continuously as  $Wi$  is raised, or else reach a plateau value as the chains approach their maximum extensions. The  $\langle R_{ete}^2 \rangle$  decreases substantially after attaining its maximum value of  $3,000\text{\AA}^2$  (corresponding to a value of  $|\mathbf{R}_{ete}|$  of  $55\text{\AA}$ ) at higher  $Wi$ , ultimately saturating at  $Wi$  on the order of 1,000.

The NEMD simulation results for the polyethylene liquid  $C_{78}H_{158}$  can be compared and contrasted to the behavior of the free-draining bead-rod chain at



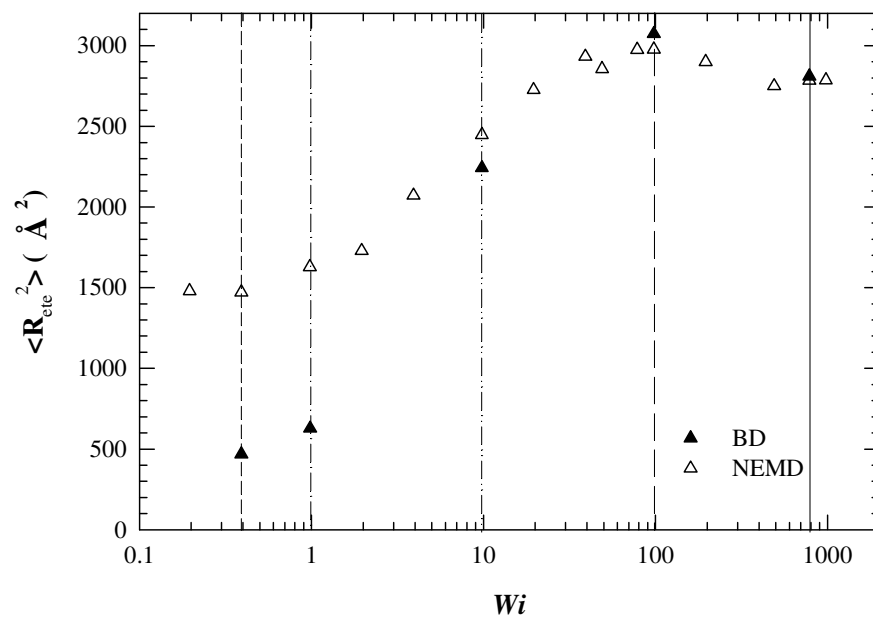


Fig. 4.3.1. The mean-square chain end-to-end distance,  $\langle R_{ete}^2 \rangle$ , for  $C_{78}H_{158}$  as a function of  $Wi$  from the atomistic NEMD (open symbols) and BD (filled symbols) simulations.

corresponding  $Wi$  using Brownian dynamics. In these simulations, five values of  $Wi$  were examined: one in the low  $Wi$  linear viscoelastic regime ( $Wi = 0.4$ ), at the transition to the nonlinear viscoelastic regime ( $Wi = 1$ ), within the  $Wi$  regime where  $|\mathbf{R}_{ete}|$  is increasing dramatically ( $Wi = 10$ ), at the maximum value of  $|\mathbf{R}_{ete}|$  ( $Wi = 100$ ), and at a very high value ( $Wi = 780$ ) after the maximum has been achieved.

Results of the BD simulations are also presented in Figure 4.3.1. At the lowest two values of  $Wi$ , the mean-squared, end-to-end distance is much smaller than the values computed from the NEMD simulations. This is as expected since the freely-jointed bead-rod model does not contain the excluded volume effect associated with the intramolecular potential energy, or any of the other four potential energy contributions either—see previous section. Hence the bead-rod chains are much more tightly coiled on average than those of the NEMD simulations, which are relatively stiff in comparison. A Kuhn step analysis of the polyethylene chains in the dense liquid reveals that 7 rods would be sufficient to describe a coarse-grained version of the PE molecule; however, these rods would have a length of  $15 \text{ \AA}$ , which is too large to catch the fine-scale dynamics of bending that are required to assume the hairpin-like tumbling structures, as described below. (The present chains are too short for this analysis to apply in a strict sense.) Here, 23 rods of length  $4.4 \text{ \AA}$  are used as described in Section 3.2 in order to capture the high shear rate behavior adequately, and the low shear rate behavior is not of direct interest.

For all values of  $Wi$  beyond unity,  $\langle R_{ete}^2 \rangle$  is almost quantitatively the same between the two model liquids. Indeed, the maximum chain extension of the bead-rod chain is the same as that of the atomistic model, and it occurs at the same value of  $Wi$ . It is very curious that these two vastly different models, one for a dense liquid, and one for an infinitely dilute solution, provide the same values of  $\langle R_{ete}^2 \rangle$  for large values of  $Wi$ .

Other research groups have found similar interesting behavior of molecular extension in solutions by comparing data over large variations of concentrations ranging from very dilute to semi-dilute. Hur *et al.* (2001) studied the dynamics of DNA solutions of concentrations ranging from  $10^{-5}c^*$  to  $6c^*$  using fluorescence microscopy and  $c^*$  is defined by a concentration at which polymer coils start to overlap. Their results for the mean fractional extension of the chain molecules indicate that this quantity is independent of concentration when it is normalized by the contour length of the molecule. The value of this extension asymptotes to a value of 0.4 at high  $Wi$ , which is again independent of the solution concentration. This is in contrast to the value of about 0.55 (it is the square of the extensions that appear in Figure 4.3.1) at the maximum chain extension in the NEMD simulations of  $C_{78}H_{158}$ . In the BD simulations of Hur *et al.* (2001) based on a bead-rod and worm-like bead-spring chain, they do not present data of mean-square, end-to-end distance,  $\langle R_{ete}^2 \rangle$ , so no evidence is available to support this conclusion. However, the critical value of  $Wi$  where the two simulation results show evidence of attaining a plateau (BD) or

maximum (NEMD) is roughly the same value of approximately 75. Stoltz *et al.* (2006) also noticed that the fractional chain extension was independent of concentration in BD simulations of a bead-spring model representing DNA solutions at concentrations varying from infinitely dilute to  $2c^*$ .

The seemingly bizarre behavior of  $\langle R_{ete}^2 \rangle$  with  $Wi$  was first observed by Morriss *et al.* (1991) and later by Cui *et al.* (1996) in NEMD simulations of shear flow for liquids of n-alkanes with chain lengths up to 24 carbon atoms. Moore *et al.* (2000) performed NEMD simulations of  $C_{100}H_{202}$  under shear, and observed a limiting plateau value of  $\langle R_{ete}^2 \rangle$  at high values of  $Wi$ . Moore *et al.* explained the maximum by comparing the hydrodynamic pressure of the simulation with the potential LJ energy of intermolecular interactions; i.e., the energetic interactions of united-atoms on separate macromolecules. They hypothesized that it occurred due to a balance between two opposing phenomena generated by the shear field. The expected (from bulk-averaged rheological theories) deformation and orientation of the macromolecules was generated by the hydrodynamic forces at low  $Wi$ ; however, for high values of the shear rate, they argued that the high amount of kinetic energy imparted to the atomic units of the chain molecules induces a randomizing Brownian-like collisional force, which causes the chains to retract from their overly extended configurations. Moore *et al.* based this hypothesis on the simulated behavior of the intermolecular LJ potential energy used in the SKS model. To illustrate this, Figure 4.3.2 reproduces data of Section 4.1 for the intermolecular LJ potential of  $C_{78}H_{158}$ ; the same qualitative

behavior is observed for all short-chain polyethylenes simulated to date. The data displays a clear decrease at low  $Wi$ , followed by a minimum value that corresponds to the value of  $Wi$  where the maximum occurs in Figure 4.3.1. Subsequently, there is a very sharp rise in the LJ potential energy with increasing  $Wi$ . The sign convention of the energetic expressions used herein is standard: the interparticle force is negative for attraction and positive for repulsion. Therefore, the decrease in the potential energy at low  $Wi$  implies a situation in which the extension and preferential orientation of the chain molecules is attractive; i.e., once extended and aligned, the chains are able to pack more closely with each other. At high  $Wi$ , however, the potential energy becomes much more repulsive and thus the atomistic units on different chains must be revisiting their less-extended and less-oriented configurations from low values of  $Wi$ . The hypothesis that these repulsive forces are due to increasingly violent interactions as the kinetic energy of the atomic units is augmented by the increase in the magnitude of the imposed hydrodynamic shear force, is thus a natural deduction from the intermolecular LJ energy data.

Although the data presented thus far seem to support the hypothesis of Moore *et al.* (2000), there are two inconsistencies which call into question this analysis. First, note from Figure 4.3.2 that the values of the intermolecular LJ potential energy in the high  $Wi$  regime are actually smaller in absolute magnitude than the equilibrium value. This implies a more repulsive system configuration than exists under

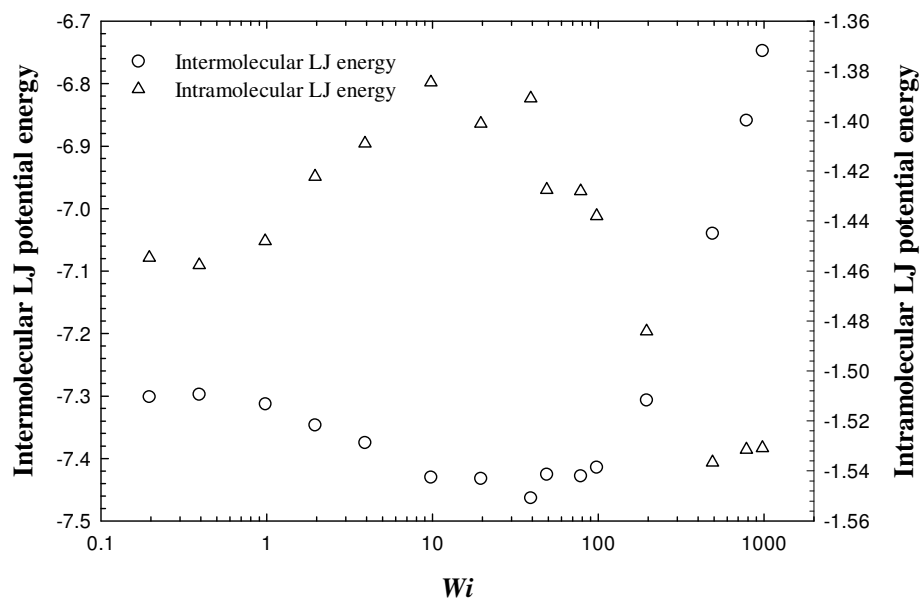


Fig. 4.3.2. The intermolecular and intramolecular Lennard-Jones potential energies as functions of  $Wi$ .

quiescent conditions, and hence implies that the chain-like molecules inhabit configurations that are more entropically favorable than those which exist when there are no hydrodynamic forces within the system. This appears to contradict the principle of maximum entropy within the perspective of Moore *et al.*, since a purely randomizing Brownian-like force could not produce an entropic state higher than that which is present at equilibrium. The second inconsistency can be deduced from the data of Baig *et al.* (2006), who performed NEMD simulations of planar elongational flow of the same short-chain polyethylene as modeled herein. Plots of the intermolecular LJ potential energy versus elongation rate from the cited article display a much more dramatic decrease in this energy for low and intermediate values of elongation rate as the molecules become highly extended and oriented in the direction of flow [Baig *et al.*, 2006b]. At the highest values of elongation rate examined, the LJ energy reaches a plateau value that is much lower than its quiescent value. This plateau occurs as the chains attain their maximum extensions of 99 Å [Baig *et al.*, 2006b]. However, at these high values of elongation rate, the hypothesis of Moore *et al.* still mandates that Brownian-like collisional forces would cause a reduction in the extension and orientation of the chains, which is not observed in the simulation data.

Here, an alternative mechanism is proposed to explain the maximum observed in the  $\langle R_{ete}^2 \rangle$  versus  $Wi$  curve of Figure 4.3.1. It is assumed that the primary contributor to the observed behavior was the development of a significant degree of single-chain rotation or tumbling at high  $Wi$ . Although the system is dominated by the entropic effects at low  $Wi$ , the vorticity imposed by the shear field ultimately

results in molecular chain tumbling events which occur with greater frequency, on average, with increasing  $Wi$ . As the chain tumbles, it assumes a configuration that takes on a hairpin-like structure at high  $Wi$ , which Smith *et al.* (1999) likened to pulling a rope over a pulley. This chain configuration increasingly narrows in width as  $Wi$  increases until the two chain segments (i.e., the two sides of the rope rotating around the pulley) are essentially nearest neighbors. This idea allows a rationalization of the behavior of the intermolecular LJ potential energy in shear and planar elongational flow, which was described above.

Again, the entropic configurational effect dominates the system at low  $Wi$ , which induces more energetically favorable side-to-side interactions between neighboring chains. This is manifested by the decrease in the intermolecular LJ energy for low values of  $Wi$ . However, once the molecules begin to tumble with increasingly hairpin-like configurations at higher  $Wi$ , the intermolecular LJ energy increases dramatically as separate chains are effectively pushed farther away and screened from each other as different segments of the same chain pass by each other during the tumbling event. Note that these hairpin-like configurations are not present at equilibrium, which explains the fact that the intermolecular LJ energy at high  $Wi$  does not assume the equilibrium value.

Further evidence confirming this explanation is provided by examining the behavior of the intramolecular LJ potential energy, which is also displayed in Figure 4.2.3. This energy is associated with the interactions of atoms on the same chain that are separated by more than three bonds. At low values of  $Wi$ , the intramolecular LJ



energy is only marginally higher than its equilibrium value; however, it increases dramatically in the nonlinear viscoelastic regime, when  $Wi > 1$ , and attains a maximum at nearly the same  $Wi$  as apparent from Figure 4.2.1. This is the expected behavior one should observe as the chain molecules extend under shear; i.e., the atoms on the same chain are pushed farther apart, and hence a less negative value of the intramolecular LJ energy. At high  $Wi$ , the energy decreases dramatically, ultimately falling below its equilibrium value. This is consistent with the notion of chain tumbling, since separate segments of the chain move past each other in close proximity. Also, the exclusion of different chains from the immediate vicinity of a tumbling molecule creates a situation in which the intramolecular LJ energy must be lower than the equilibrium condition, since the atomic units of the same chain are closer together at high  $Wi$  during a tumbling event than they are under quiescent conditions. The data for the intramolecular LJ energy under planar elongational flow of Baig *et al.* (2006) displayed a monotonically increasing intramolecular LJ potential energy, which was due to the continuous stretching of the chain molecules in the flow direction.

Dunstan *et al.* (2004) performed steady shearing experiments on semi-dilute solutions of polydiacetylene 4-butoxycarbonylmethylurethane in chloroform. Optically polarized rheometry was performed on the solutions, revealing significant segmental orientation and distortion in the shear-vorticity plane. At low shear rates, the behavior of the molecules was similar to that described above, which is consistent with pre-averaged rheological theories; i.e., the chains extend and orient relative to the

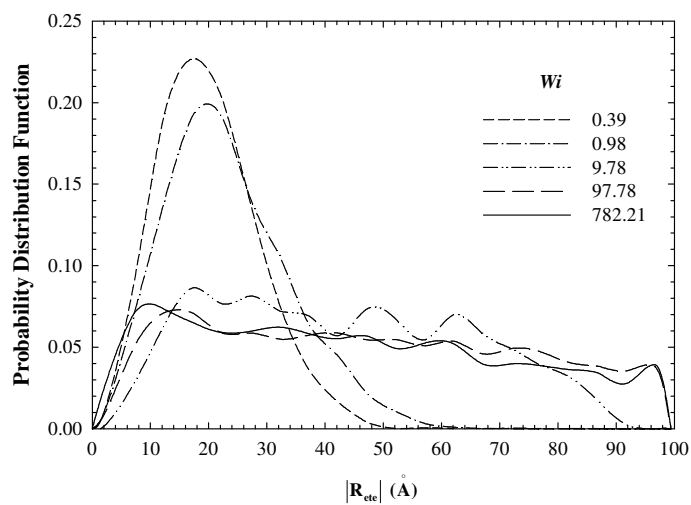
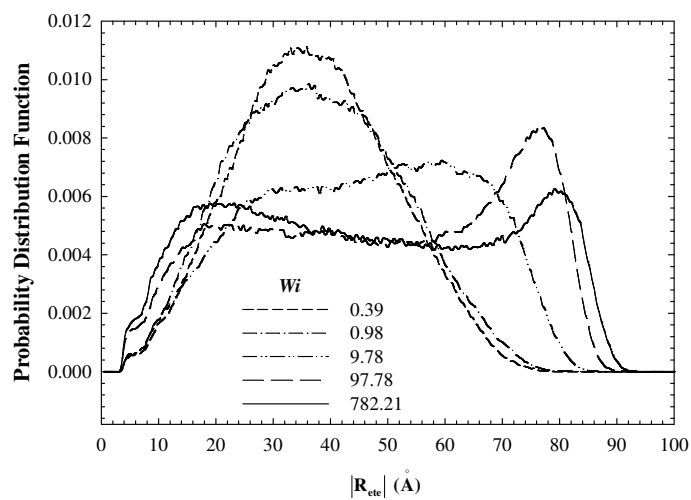


Fig. 4.3.3. Probability distributions of  $|R_{ete}|$  for the five values of  $Wi$  designated by the vertical lines in Figure 4.3.1 as calculated in the NEMD (4.3.3a) and BD (4.3.3b) simulations.

direction of flow. However, at higher shear rates, a maximum occurs in the segmental extension, with a subsequent decrease in this quantity with further increase of shear rate. Dunstan *et al.* describe these high shear chain configurational changes as “balling,” since the chains appear to become less oriented and extended as the shear rate increases beyond the maximum. However, it is evident that this bulk-average rheo-optical measurement might simply be responding to the onset of rotational motion, which reduces the ensemble average of the extension of the end-to-end vectors of the chain molecules. Note that these molecules contain a significant degree of side-chains, which could result in more coiled than hairpin-like rotation at high shear rates beyond the maximum.

Further evidence of chain tumbling is provided by Figure 4.3.3, which displays the probability distribution of finding a chain with an end-to-end vector of a certain magnitude. The distributions at the five values of  $Wi$  presented in this figure correspond to the vertical lines in Figure 4.3.1. These values of  $Wi$  were chosen to depict the behavior in the five regimes of interest: one in the linear viscoelastic regime, one at the transition from linear to nonlinear viscoelasticity, one in the regime of dramatically increasing chain extension, one at the maximum chain extension, and one at very high  $Wi$  beyond the maximum.

According to Figure 4.3.3a of the NEMD simulations, the distribution at the lowest value of  $Wi = 0.39$  displays the expected Gaussian behavior, with the peak centered around a value of  $|\mathbf{R}_{ete}|$  that is very close to the equilibrium value of  $38\text{\AA}$ . As  $Wi$  is increased to unity, the distribution retains its Gaussian character, and the peak

location shifts to higher values of  $|\mathbf{R}_{ete}|$ . This is the expected behavior from a pre-averaged rheological theory. However, at the same time, the peak of the distribution is decreasing in height, and the whole distribution is widening. This behavior has also been observed by Morriss *et al.* (1991), for liquids decane and eicosane. These trends are not expected from pre-averaged theories, and indicate that the degree of alignment around the preferred direction of orientation is diminished by the increasing hydrodynamic shear forces within the liquid. When  $Wi$  ( $> 1$ ) is well within the nonlinear viscoelastic regime, where the average extension of the molecules is increasing rapidly (see Figure 4.3.1), the distribution has widened considerably, and has developed a rudimentary shoulder on its left side. The peak of the distribution has continued to shift to longer values of  $|\mathbf{R}_{ete}|$ , corresponding to the increasing extension of the molecules. For larger values of  $Wi$ , it is apparent that the distributions become inherently bimodal, with a high “stretch” peak at large values of  $|\mathbf{R}_{ete}|$ , and a second “rotational” peak at low  $|\mathbf{R}_{ete}|$ . No hint of a rotation peak appears in the decane simulations of Morriss *et al.* (1991); however, their simulations of the longer molecule eicosane begin to display similar behavior at the highest shear rates

As the degree of chain tumbling increases with  $Wi$ , the average value of  $|\mathbf{R}_{ete}|$  must decrease since this quantity becomes relatively small as the chain ends of the hairpin-like structure pass each other during mid-cycle. Thus on a time-averaged basis, the distribution is smeared to the left side of the stretch peak, and to such an

extent that a second rotational peak develops at high  $Wi$ . Note that the stretch peak at  $Wi = 782$  corresponds to  $|\mathbf{R}_{ete}| \sim 80\text{\AA}$ , which is approaching the maximum extension of  $99\text{\AA}$ . Further note that the rotational peak occurs at  $|\mathbf{R}_{ete}| \sim 20\text{\AA}$ , which is less than the equilibrium value of  $38\text{\AA}$ ; this implies that the chain ends during the tumbling cycle are closer together on average than they are under quiescent conditions since the chain ends are tumbling with the kinked, hairpin-like configurations. At the same time, the overall average of the chain extension is determined from Fig. 4.3.1 as  $|\mathbf{R}_{ete}| \sim 53\text{\AA}$ , which correspond to neither the stretch nor the rotational peak in Fig. 4.3.3a but is very close to the value of at the maximum extension of  $55\text{\AA}$  in Fig. 4.3.1.

Some of the characteristic behavior of the distribution of chain lengths described above has been observed before in experiment. Teixeira *et al.* (2007) observed the widening of the distribution with shear rate in concentrated DNA solutions when individual molecular tumbling events were contributing significantly to the dynamics of the liquid. However, the mean of the distribution continuously shifted to the right, indicating a significant, continuous domination of the probability distribution by its stretching component. Smith *et al.* (1999) also observed this widening of the distribution with shear rate in their dilute DNA solutions; however, one can observe a slight degree of bimodality (which might be due to statistical error) in their distribution at the highest value of  $Wi = 76$ --see their Figure 4 [Smith *et al.* (1999)]. This value of  $Wi$  is approximately the same as that at which the present

simulations begin to reveal a bimodality in the distribution ( $Wi \sim 80$ ), as evident from Figure 4.3.3a.

Figure 4.3.3b displays the corresponding probability distributions as calculated from the BD simulations at the same five values of  $Wi$  as stated above. At the lowest value of  $Wi$ , the distribution is again Gaussian. As  $Wi$  increases, the distribution begins to widen as the transition zone to the nonlinear viscoelastic region is surpassed. For high values of  $Wi$ , the distributions become extremely wide, covering almost the full range of reasonable values of  $|\mathbf{R}_{ete}|$ . Note that the distribution continues to extend to lower values of  $|\mathbf{R}_{ete}|$  with increasing  $Wi$ , as in the NEMD simulations, and that there is a significant probability of finding chain with  $|\mathbf{R}_{ete}|$  values that are lower than the equilibrium value. Although there is no hint of bimodality in these distributions, it is readily apparent that the same physical phenomena are involved in this system: the chain molecules are tumbling between highly stretched and barely extended configurations.

The tumbling dynamics of a single, random individual chain from the NEMD simulation are displayed in Figure 4.3.4a at the highest value of  $Wi = 782$ . The value of  $|\mathbf{R}_{ete}|$  changes dramatically with time, in a quasi-periodic fashion. It oscillates between very extended chain configurations, near the fully extended length of  $99\text{\AA}$ , and very low values that are less than the equilibrium extension of  $38\text{\AA}$ . As demonstrated below, these low values of  $|\mathbf{R}_{ete}|$  correspond to the folded

configurations of the hairpin-like molecular conformations as the chain ends pass each other during a tumbling cycle. Note that  $|\mathbf{R}_{ete}|$  spends more time in the stretched configurations, on average, than it does in folded conformations. Meanwhile, the orientation angle,  $\theta$ , measured with respect to the direction of flow, undergoes dramatic fluctuations that correspond to the changes in the magnitude of the end-to-end vector. Indeed, the orientation angle flips sign at exactly the same times as the minima in the  $|\mathbf{R}_{ete}|$  time variation. This again indicates that the chain ends approach each other very closely during the tumbling cycle. Nevertheless, the orientation angle remains at a small, positive value of approximately 5 degrees, on average, which corresponds very well to the value expected from pre-averaged rheological theories. The fact that the value of  $|\mathbf{R}_{ete}|$  is essentially large on average, and that the value of  $\theta$  attains a value of approximately 5 degrees at high  $Wi$ , explains why the pre-averaged theories give the predictions that they do. It also demonstrates that the pre-averaged theories fail to describe the small timescale tumbling dynamics of the molecules; i.e., they are coarse-grained out of the system description during the averaging process. (Baig and Mavrantzas (2009) also have recently witnessed this in their multiscale simulations.) Note that this molecule spends most of its time with a positive orientation, but once it is tipped into a negative orientation it quickly tumbles back into a positive orientation with the two ends of the chain swapping places. These negative configurational excursions are induced by either hydrodynamic or Brownian forces.

It is possible to speculate concerning the highly elliptical, hairpin-like rotation at high  $Wi$ . When viewed from a perspective involving more than one molecule, i.e., when viewing an individual molecule along with its set of nearest neighbors, it is apparent that a reptative type of dynamical mechanism is in operation, even though the liquid is not even remotely entangled. The rotating molecule is essentially diffusing through tube-like structures that are composed of the highly stretched surrounding molecules. A hydrodynamically-induced Brownian excursion of a stretched chain end into a negative orientation often results in the chain diffusing out of its original tube-like structure into a similar tube below it in the flow-gradient plane. The rotating chain is essentially diffusing from a tube-like structure at a higher velocity into one directly below it with a lower velocity, just as one would expect from a rotating rigid particle suspended in a solvent undergoing shear flow. However, in the present case, the surrounding molecules inhibit the allowable chain configurations during the rotational period to those which are highly elliptical (hairpin-like).

The type of tumbling mechanism just described can, in principle, be very much different than what is observed for a liquid composed of flexible polymer chains suspended in dilute solution, as simulated using Brownian dynamics.  $|\mathbf{R}_{ete}|$  and  $\theta$  for a random chain from the BD simulation at  $Wi = 782$  are plotted versus time in Figure 4.3.4b. It is evident from this figure that the tumbling of the chain molecule is again occurring in a hairpin-like configuration; however, in this case, it is apparent that the time dependence is decidedly periodic in nature, rather than merely quasi-periodic



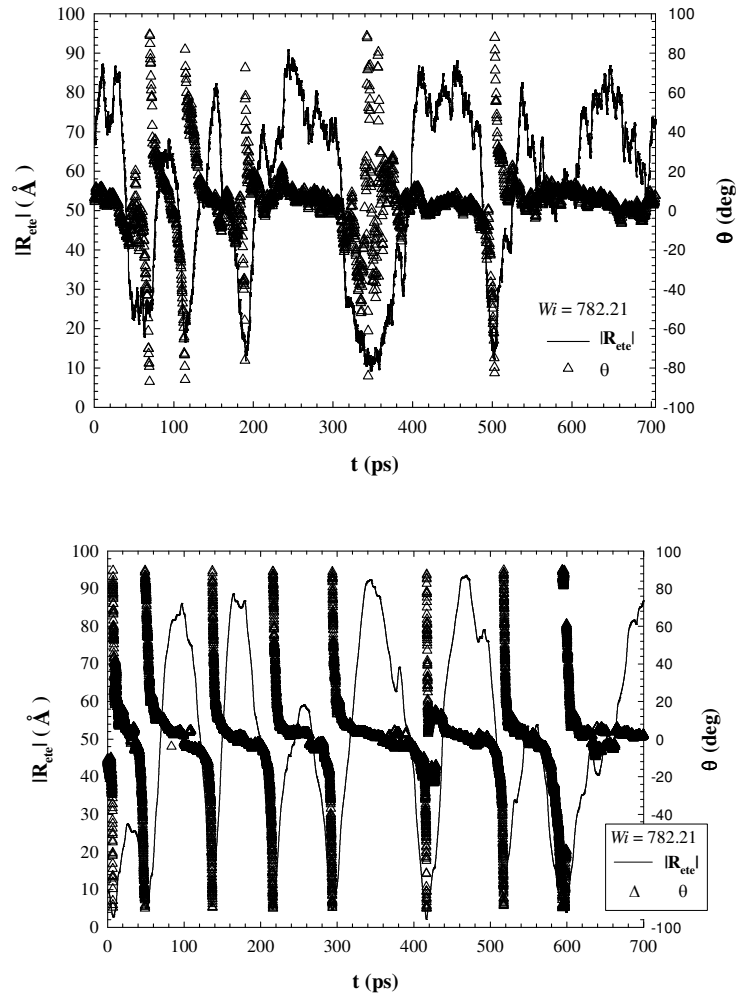


Fig. 4.3.4. The magnitude of end-to-end vector,  $|R_{ete}|$ , and the orientation angle with respect to the flow direction,  $\theta$ , as functions of time for a random chain of the NEMD (4.3.4a) and BD (4.3.4b) simulations.

as in the NEMD simulations of Figure 4.3.4a. This is due to the assumption of the free-draining bead-rod chain in the BD simulations, which eliminates all intermolecular effects that constrain the tumbling motion in the dense liquid of the NEMD simulations.

In Fig. 4.3.5, plots of the components of the radius of gyration tensor vs. time displayed remarkable differences between rotation of the chain molecules in the NEMD and BD simulations. In the dense liquid case, the  $xx$ -component of the gyration tensor fluctuated within a relatively narrow range of values with intermediate extension. However, in the case of the free-draining chains, this component oscillated dramatically between highly extended and very low values, especially at high  $Wi$ . In both cases, the other components did not change much with time although there was a marked difference in the  $yy$ -component of the gyration tensor with the dense liquid attaining a much higher value. This suggests that the chain molecules are rotating with very different configurational motions than is suggested by Figure 4.3.4. In the dense liquid, the chains tumble in a highly extended conformation, as if on a conveyor belt. However, the free-draining chains experience an almost complete retraction or recoil collapse to a configuration that is more tightly coiled than at equilibrium during the nexus of the tumbling cycle. (This is not prohibited because of the neglect of excluded volume effects.) Further evidence of this configurational motion will be discussed below.

Figure 4.3.6 depicts the probability that a specific macromolecule has an orientation angle that is positive or negative. This probability is 0.5 for either positive

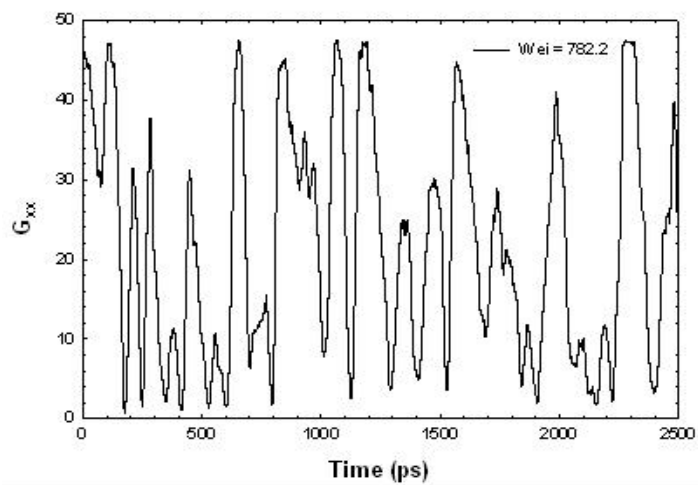
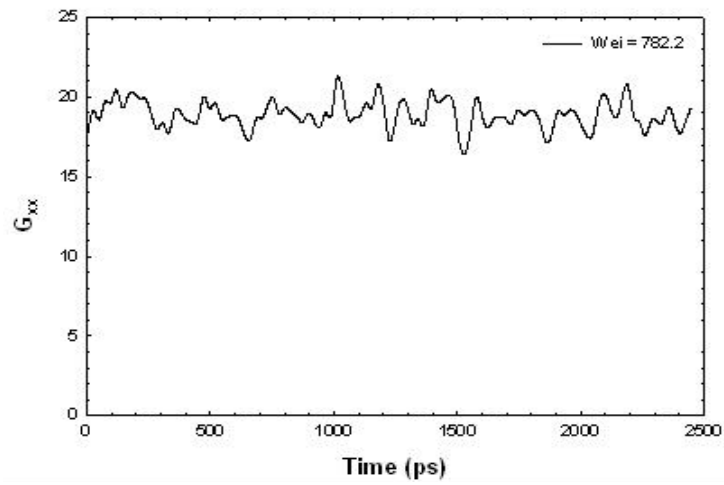


Fig. 4.3.5. The  $xx$  component of radius of gyration of a random single chain as a function of time

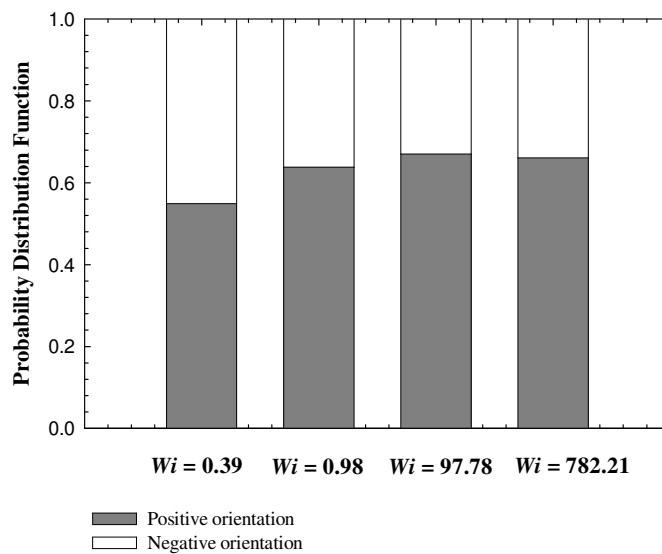


Fig. 4.3.6. Probability distribution of positive and negative end-to-end vector orientations in the dense liquids (NEMD simulations) at four values of  $Wi$ .

or negative orientation under quiescent conditions. At low  $Wi$ , the probability of a positive orientation grows steadily in the regime where the orientation angle is dropping rapidly from the quiescent value of 45 degrees to its high  $Wi$  limit of about 5 degrees. This probability saturates at roughly 0.65 at high  $Wi$ , indicating that the theoretical pre-averaged value of the orientation angle has been attained. This confirms that the individual chain behavior displayed in Figure 4.3.4a is consistent with the pre-averaged theories after the coarse-graining step (the averaging) has been performed.

BD simulations of the free-draining chains exhibited behavior that was quantitatively consistent with that of the NEMD simulations at the lowest two values of  $Wi$ , but the chains had a smaller probability of exhibiting a positive orientation at high  $Wi$  than the NEMD liquids. This is due to the fact that the BD free-draining chains are tumbling with greater frequencies at high  $Wi$ , as expected (compare Figures 4.3.4a and 4.3.4b; also see Figure 4.3.10 below); therefore, on a time-averaged basis, chains spend more time inhabiting the negative quadrants. In the case of the dense liquid, Brownian forces cause the foremost chain end to dip eventually into the fourth quadrant in the gradient plane, thereby inducing a tumbling cycle. This is a less common event in the dense liquid than in the free-draining chain, since the chain end must diffuse around neighboring chains to execute the entry into the fourth quadrant.

Figure 4.3.7 displays data for the probability density function of the possible chain configuration classes at four values of  $Wi$ . The configuration classes are aligned from left to right in order of increasing molecular extension of the end-to-end

vector. As expected, mildly extended configurations dominate the conformational space of the macromolecules at low  $Wi$ . There are relatively few coil configurations relative to folded ones since these molecules are too short in length to allow the occurrence of many tightly coiled conformations, as defined by the brightness distribution described above. For these short-chain liquids, the molecules are relatively stiff, even though much longer polyethylene chains are very flexible; there are only 7 Kuhn segments at equilibrium. This relative stiffness also explains the occurrence of the more highly extended configurations, half dumbbells and stretched, even at this low value of  $Wi$ . However, one must keep in mind that these classifications are based on the brightness distribution defined in the previous section; in this definition, the configurations are based on shape, rather than absolute length. For example, consider two pieces of string with the same length; one is tightly stretched so that the end-to-end vector assumes its maximum value, and the other has a wavy character with a small period and amplitude. Both of these strings will be classified as stretched configurations, even though the second one has a much shorter end-to-end vector than the first.

Increasing  $Wi$  from the linear viscoelastic regime to the transition region ( $Wi \sim 1$ ) reduces the number of chains occupying tightly coiled or folded configurations, and promotes configurations of intermediate extensions. As  $Wi$  increases further into the nonlinear viscoelastic regime, the number of coiled configurations is reduced further, and the probability of highly extended configurations, such as half dumbbells and stretched, is dramatically increased. Even so, the probability of finding a less

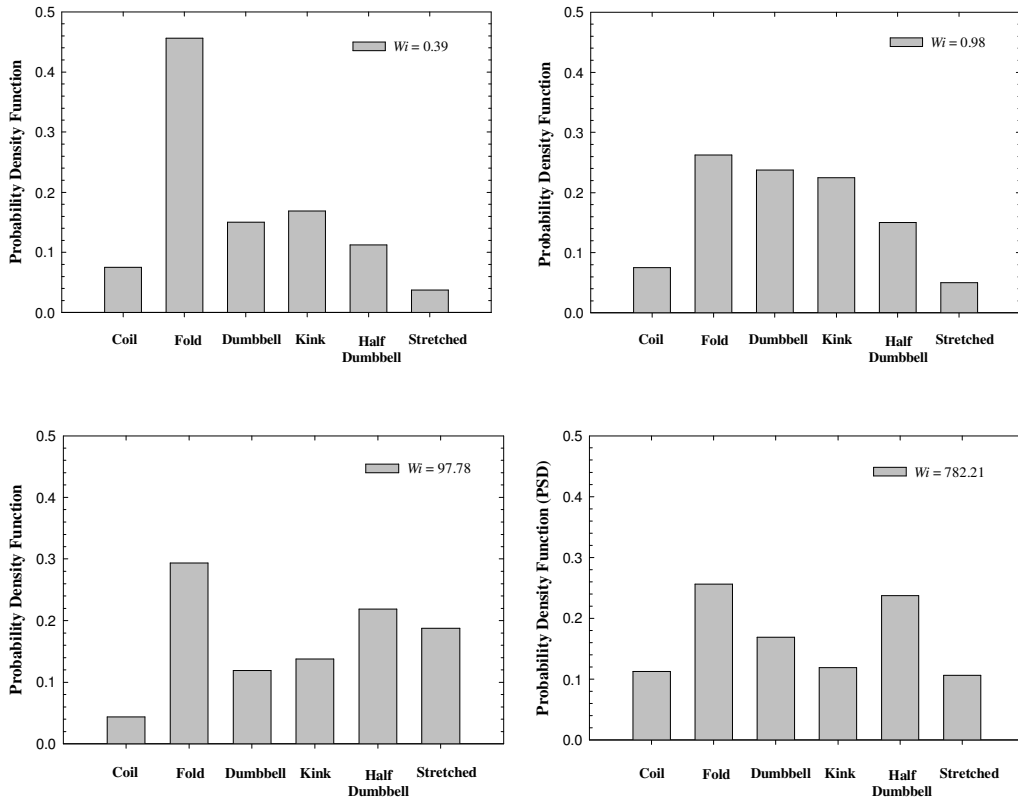


Fig. 4.3.7. Probability distribution of representative chain configuration classes in the dense liquids (NEMD simulations) at four values of  $Wi$ .

extended fold configuration is still significant. This is due to the fact that as the chains are rotating with greater frequency, and in an increasingly elliptical fashion: this demands that the fold configuration becomes more prominent. At very high  $Wi$ , the number of highly extended molecules continues to increase, and the number of folded and coiled configurations remains approximately constant. These trends become more obvious when comparing the plots of  $Wi = 0.39$  and  $Wi = 782$  of Figure 4.3.6: one again observes a rather bimodal distribution of chain configuration classes at high  $Wi$ , whereas it is essentially Gaussian at low  $Wi$ .

Roughly the same qualitative behavior as depicted by Figure 4.3.7 can be seen in the BD simulation data of the 15-segment bead-spring chain model of dilute macromolecular solutions of Venkataramani *et al.* (2008). Furthermore, the new BD simulations reported herein compared favorably with those of the NEMD simulations, except that there were far fewer of the relatively extended half-dumbbell and stretched configurational states near the equilibrium state; this is to be expected since the degree of extension of the chains in this  $Wi$  regime was much smaller than for the dense liquid due to the absence of intramolecular and intermolecular potential energies in the free-draining, bead-rod model—refer to Figure 4.3.1. Furthermore, at high  $Wi$  the free-draining solution showed a much higher percentage of coiled configurations, whereas the dense liquid chains showed a greater percentage of folded conformations. This is due to the differences in the configuration tumbling cycles (extended in the dense liquid, and tightly coiled in the dilute solution), as described above.



In order to analyze further the simulation data,  $|\mathbf{R}_{ete}|$  was split into three regions, relative to the distributions of Figure 4.3.3: in units of Å, region 1, [0,40]; region 2, [40,65]; and region 3, [65-100]. The vertical lines delineate the regimes of interest, which were defined relative to the distributions of the lowest (0.39) and highest (782)  $Wi$  that were simulated. Region 1 contains the rotational peak at high  $Wi$ , and region 3 contains the stretch peak. At low  $Wi$ , regions 1 and 2 each contain about half of the stretch peak.

Figure 4.3.8 displays a histogram of the probability distribution function at the four values of  $Wi$  indicated on the plot for the dense liquid model used in the NEMD simulations. At the lowest value of  $Wi$ , the highest probability lies in region 1, with the remainder in region 2 and practically no molecules in the highly stretched region 3. There is a significant difference in the probabilities of regions 1 and 2 because the separator between these two regions is not centered at the peak—refer to preceding paragraph. At  $Wi = 0.98$ , the probabilities in the first two regions are about equal, which is a result of the fact that the distribution function remains almost Gaussian, but the peak has shifted to a slightly higher value of  $|\mathbf{R}_{ete}|$ , thus making the demarcation line between regions 1 and 2 more nearly centered at the peak. Stretched chain configurations in region 3 also begin to become evident at this value of  $Wi$ . At  $Wi = 97.8$ , all three regions have roughly the same probabilities, with the rotational configurational probability slightly favored; however, the stretch region (3) now has a significant probability of occurrence. As  $Wi$  is increased to 782, the probability of

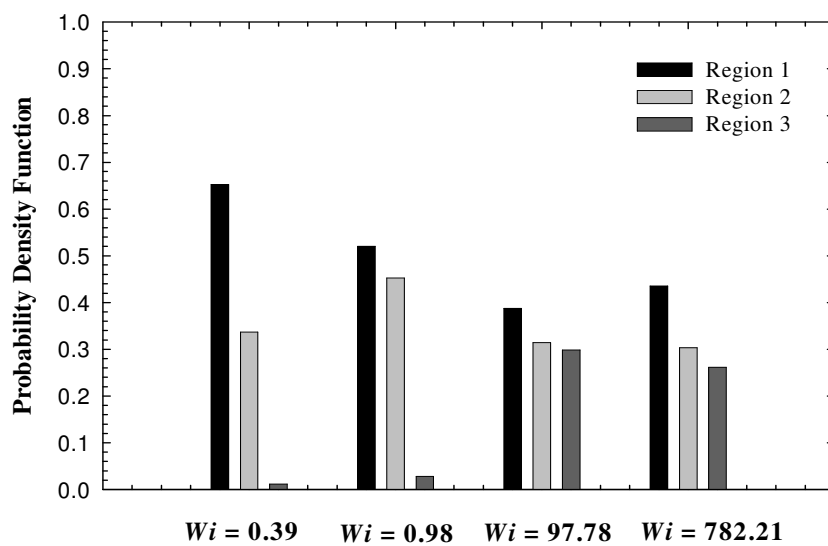


Fig. 4.3.8. Probability distribution of molecules within the three regions of  $|\mathbf{R}_{ete}|$  defined in the text for the dense liquids (NEMD simulations).

region 1 increases from its previous value at  $Wi = 97.8$ , which is due to the hydrodynamic augmentation of the chain tumbling dynamics; i.e., more chains are rotating and with greater frequencies, creating more folded structures on a time-averaged basis. At the same time, the number of chains in stretched configurations has decreased from the previous value of  $Wi$  as the molecules spend less time in stretched configurations due to the increasing frequency of the tumbling behavior.

The behavior of the chains in the BD simulations is qualitatively and quantitatively similar, except at the lowest two values of  $Wi$ . At those shear rates, there were almost no contributions to the regions 2 and 3 probabilities, which again reflects the lack of interbead repulsive forces in the free-draining chain model.

The mechanistic dynamics of the chains can be investigated through calculation of time correlation functions for the components of  $\mathbf{R}_{ete}$ . This allows determination of characteristic timescales intrinsic to the dynamical chain processes. Aust *et al.* (2002) examined time correlations of the components of the gyration tensor for a dilute polymer solution via NEMD simulation, and demonstrated that the average chain angular velocity approached the theoretical value of the vorticity  $(-\dot{\gamma}/2)$  as  $\dot{\gamma} \rightarrow 0$ . As the shear rate increased, the chain became increasingly elongated and its angular velocity dropped relative to the vorticity of the shear field [Aust *et al.*, 2002]

Figure 4.2.9a displays data for the correlation  $\langle R_x(t)R_y(t+\tau) \rangle$  with respect to observation time at values of  $Wi = 0.98, 97.8,$  and  $782$  for the dense liquid NEMD

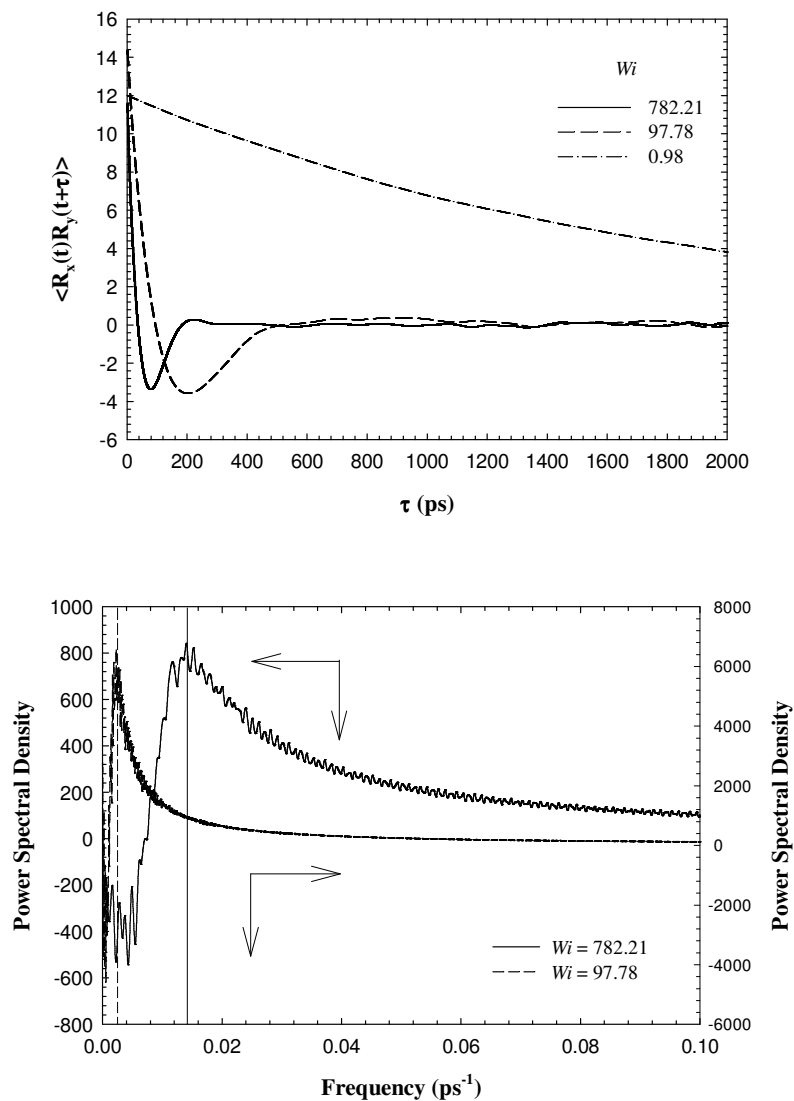


Fig. 4.3.9. Time cross-correlation functions versus observation time for three values of  $Wi$  (4.3.9a), and the power spectral density (4.3.9b) versus frequency for two values of  $Wi$  that exhibit minima in the cross-correlation function curves in the dense liquid simulations.

simulations. Note that the correlations  $\langle R_x(t)R_x(t+\tau) \rangle$  and  $\langle R_y(t)R_y(t+\tau) \rangle$  displayed the same qualitative behavior as indicated in the figure, and that similar plots were obtained at all values of  $Wi$  investigated. Cross correlations between other off-diagonal pairs of components of  $\mathbf{R}_{ete}$ , as well as the  $R_zR_z$  correlation exhibited no correlations. These data reveal definite correlations between certain components of  $\mathbf{R}_{ete}$ , with characteristic timescales that are dependent on  $Wi$ . At low values of  $Wi$ , within the linear viscoelastic regime, the typical behavior is observed in which the chain relaxation is dominated by the longest relaxation time,  $\tau_R$ . However, for  $Wi > 2$ , the correlation curves each exhibit a characteristic minimum, followed by a local maximum, and then a damped oscillatory behavior at longer times; this behavior is indicative of characteristic timescales beyond the Rouse time. The free-draining chain model exhibited the same features.

These time scales can be quantified using the power spectral density, which is displayed in Fig. 4.2.9b, through Fourier transformation of the correlation signal. With respect to the dynamics of  $\mathbf{R}_{ete}$ , it is evident that the correlations describe various aspects of the dynamics of the rotation motion of the chains. Characteristic frequencies can be determined from the maxima in the power spectral density curves, as indicated in the figure.

Fig. 4.2.10 displays data for the intrinsic timescales associated with the dynamical chain motion:  $\tau_R$ , the Rouse time (horizontal line), as well as  $\tau_{xx}$ ,  $\tau_{xy}$ ,  $\tau_{yy}$ , and  $\tau_{conv}$ , as functions of  $Wi$  from both the NEMD and BD simulations. The

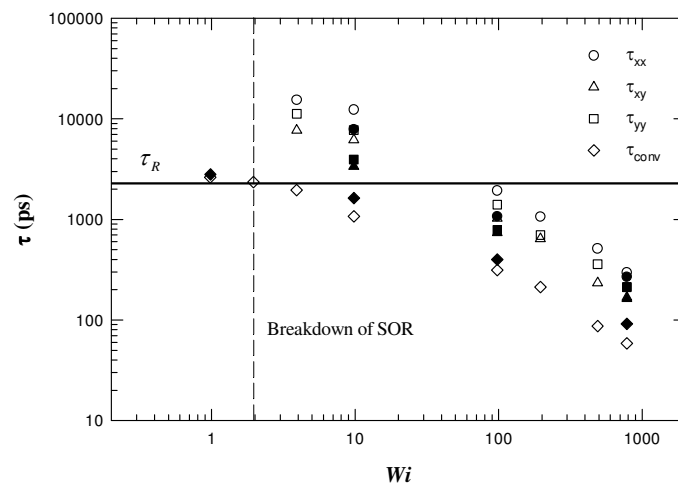


Fig. 4.3.10. Characteristic timescales versus  $Wi$ . The horizontal line represents the Rouse time. The vertical dashed line represents the value of  $Wi$  at which the stress-optical rule begins to breakdown in simulations of  $C_{50}H_{102}$ . Diamonds represent the timescale of relaxation of the extended molecules, and all other symbols represent the timescales associated with the various auto and cross correlations of the end-to-end vector. Solid symbols represent dilute solution data, and unfilled symbols denote dense liquid data.

$\tau_{ii}$  are associated with the correlations of the corresponding components of  $\mathbf{R}_{ete}$ , as defined above. These timescales are expected to be associated with various aspects of the chain rotation, such as the tumbling frequency, wagging motion, etc. Although these timescales are slightly different for the various components of  $\mathbf{R}_{ete}$ , it is not evident what are their exact interpretations; presumably, each represents a distinct facet of the chain tumbling dynamics, which is not apparent at the present time. Since  $\mathbf{R}_{ete}$  has both magnitude and direction, it is possible that these small differences arise due to the stretch contribution (i.e., the magnitude) of  $\mathbf{R}_{ete}$  rather than its directional contribution. Furthermore, the ensemble average of any component of  $\mathbf{R}_{ete}$ , which is performed when calculating the correlation  $\langle R_x(t)R_y(t+\tau) \rangle$  for example, is weighted toward molecules of high extension. To investigate this issue, correlations were also computed in terms of the unit vector,  $\mathbf{u} = \frac{\mathbf{R}_{ete}}{|\mathbf{R}_{ete}|}$ , in which each molecule is weighted equally, regardless of its length. These correlations, such as  $\langle u_x(t)u_y(t+\tau) \rangle$ , should eliminate any stretch contribution to the intrinsic timescales that are manifested through the correlations; however, no statistically discernable difference was noted between these correlations and the data presented in Figure 4.2.10. The timescale  $\tau_{conv}$  is assumed to correspond with the relaxation of the stretched chain configurations, which may be associated with the convection and deformation of the tube-like structures, described above, which are formed by neighboring chains that are almost fully stretched. These timescales can be quantified by assuming that the  $R_x R_x$  correlation bears the functional form of  $A \exp(-t/\tau_{conv}) \cos(2\pi t/\tau_{xx})$ , where  $A$

is a constant. From this expression, at equilibrium,  $\tau_{xx} \rightarrow \infty$ , so that  $\tau_{conv} \rightarrow \tau_R$ . As  $\tau_{conv} \rightarrow \infty$ , the motions of the chains would become purely tumbling, similarly to rigid rods.

Using this assumed expression, as the shear rate decreases toward zero from a finite value, the  $\tau_{ii}$  assume values between 5 and 10 times the Rouse time. For  $Wi < 2$ , one can no longer observe minima in the time correlations of  $\mathbf{R}_{ete}$ , implying that the rotational timescales are no longer evident in the system response. (Note that this value of  $Wi = 2$  corresponds to the profile in Figure 4.3.3a where the distribution became non-Gaussian.) This is caused by the low degree of vorticity in the flow field, which inhibits the excursions of the molecules into negative orientations. In other words, at low values of  $Wi$ , the dynamics are dominated by the deformation of the macromolecules because the shear flow has a timescale greater than the Rouse time (i.e.,  $1/\dot{\gamma}$ ), implying that the rotational motion is insignificant relative to the dynamics of the deforming chains. Apparently, the Brownian-like fluctuations induced by the shear forces are only capable of deforming the molecules in this  $Wi$  regime, and can only induce fluctuations that lead to tumbling once the molecules are at least partially extended and, more importantly oriented near to the flow direction. Once the chains are oriented near to the flow direction (about 5 degrees) at high  $Wi$ , it is easier for random Brownian-like forces to induce the chain orientation to progress into the fourth quadrant, thus initiating a tumbling cycle. At low shear rates, the orientation of the deformed chains is above 15 degrees, which makes it relatively difficult for a Brownian excursion into the negative quadrant. In principle, the rotational timescales



should approach infinity as  $Wi$  approaches zero. Thus, at low values of  $Wi$ , only the Rouse time is evident in the relaxational response of the liquid.

As  $Wi$  increases into the nonlinear viscoelastic regime, all of the rotational timescales are reduced dramatically, until they have decreased below the Rouse time; this indicates a higher frequency of tumbling and induces the first peak in the distributions of Fig. 4.3.3a. Thus at high shear rates, the rotational motion of the chains dominates the system response. The timescale  $\tau_{conv}$  is equivalent to  $\tau_R$  at low shear rates, but then also decreases substantially at higher shear rates. Presumably, this quantifies the affect of the flow kinematics on the convection and orientation of the reptative tube network within the fluid; i.e., as the chains become stretched to their maximum lengths, they form highly oriented, tube-like structures between neighboring stretched chains, which allow freer rotation of other chains occupying the same vicinity. All of these timescales possess power-law behavior with  $Wi$ , as discussed below in reference to Figure 4.3.11.

Recent experiments of semi-dilute and concentrated DNA solutions have revealed multiple timescales associated with the kinematics of shear flow [Teixeira *et al.*, 2007; Robertson and Smith, 2007]. Teixeira *et al.* (2007) observed two distinct timescales, in addition to the Rouse time, for their most concentrated solution; however, for unentangled solutions of lower concentration, they observed only a single timescale. For the highly entangled solution, they observed a ratio of the slow to fast timescales of approximately 50. Furthermore, the fast timescale was roughly a factor of 10 higher than the estimated Rouse time, and was attributed to chain retraction.

Robertson and Smith (2007) recorded three distinct timescales, each differing from the next by an order of magnitude. The shortest timescale was estimated as the Rouse time, the longest timescale was associated with the disengagement time of reptation theory, and the intermediate timescale was related to a second reptative phenomenon that was correlated with the dynamics of the effective reptation tube. The ratio of the tube dynamics (the intermediate) timescale to the Rouse time was roughly 12 [Robertson and Smith, 2007], which is of comparable magnitude to the factor determined by Teixeira *et al.* (2007). Although the liquids simulated in the present study are not even remotely entangled, the rotational timescales are roughly a factor of 6 higher than either the Rouse time or  $\tau_{conv}$  at all values of  $Wi$ . Given the differences in the entangled solutions and the unentangled liquids examined herein, it is difficult to compare directly experiment and simulation. However, in the present case, it does appear that the faster timescale,  $\tau_{conv}$ , is associated with some sort of constraint release through the formation of tube-like structures which allow some molecules to tumble more freely with respect to almost fully stretched surrounding chains in the NEMD simulations. Recall that this timescale is associated with the decay of the correlation between configurations at a specified time with those of later times. Consequently, the data of Figure 4.3.10 indicate that this correlation dies out faster at higher  $Wi$  values than it does in the linear viscoelastic regime; i.e., the molecular configurations become statistically independent at a faster rate when the shear rate is high. This is reasonable since smaller segments of the chain molecules

become dynamically active as  $Wi$  is increased, thus providing additional degrees of freedom to the chain's overall configurational state.

It is very interesting that the NEMD and BD simulations appear to yield similar characteristic timescales, despite the large conceptual differences in the models used in the computations. The BD simulations show faster rotational timescales, which correspond to greater frequencies of rotation. This is to be expected since the free-draining chain model is not constrained by the presence of surrounding macromolecules. It is interesting that the convected timescale,  $\tau_{conv}$ , is also apparent in the BD simulations, which could support the hypothesis that this timescale is associated with the enhanced configurational dynamics at high  $Wi$  of the stretched chain configurations as opposed to the configurations present during the tumbling cycle, whether in the free-draining solution or the dense liquid. Note that the difference in  $\tau_{conv}$  between the NEMD and BD simulations is not assured to be statistically significant based on the present analysis; however, the trend of the data in Figure 4.3.10 suggests that the correlation time is longer for the free-draining chains than it is for the dense liquid. To explain this observation, one can recall the argument presented above concerning the  $Wi$  dependence of the segmental dynamics: as the shear rate increases, smaller chain segments become dynamically active, and contribute to the configuration constraint release. In the free-draining chain simulations, the course-graining procedure dictates the constant bond length between beads, thus permanently freezing the small segmental dynamics beyond a certain limit. Once this limit is achieved, increasing  $Wi$  further does not contribute any additional

degrees of freedom to the configurational chain decorrelation, thus effectively slowing down the decay of the correlation relative to the atomistic chain model used in the NEMD simulations.

An additional explanation for the more rapid decay of the correlation in the NEMD simulation of the dense liquid can be rationalized on the basis of Figure 4.3.4. Recall that the dense liquid displayed only quasi-periodic temporal behavior of the end-to-end vector cycles, whereas the free-draining chain solution experienced a more regular periodic tumbling cycle. Consequently, it is apparent that the dense liquid should exhibit a faster rate of decorrelation than the free-draining liquid, leading to a smaller  $\tau_{conv}$  timescale. Hence another possible interpretation of the simulation data is that the  $\tau_{ii}$  characterize the rotational frequencies of the tumbling molecules, and  $\tau_{conv}$  quantifies the timescale over which the correlation in the rotational motion decays.

Another interesting observation from Figure 4.3.10 is the apparent correlation between the appearance of the rotational timescales, the deviation of the Rouse time from its equilibrium value, and the onset of the breakdown in the stress-optical rule observed for a similar liquid ( $C_{50}H_{102}$ ) by Baig *et al.* (2007). The rotational timescales and the deviation from the Rouse time appear well beyond the transition between the linear and nonlinear viscoelastic regimes ( $Wi = 1$ ). A plausible hypothesis then is that the breakdown in the stress-optical rule under shear is caused by the tumbling motion of the macromolecules, which also could be partially responsible for the shear-thinning behavior; i.e., not only are the stretched configurations of the

chains relieving the hydrodynamic stresses induced by the shear, but the chain tumbling is also offering some relief.

The data of the  $\tau_{ii}$  and  $\tau_{conv}$  presented in Figure 4.3.10 appear to follow power-law behavior at high  $Wi$ . Figure 4.3.11 displays this power-law dependence of the NEMD simulations using graphs of  $\ln\left(\frac{\tau_{xy}}{\tau_R}\right)$  and  $\ln\left(\frac{\tau_{conv}}{\tau_R}\right)$  with respect to  $\ln Wi$ . (The regression of the timescales  $\tau_{xx}$  and  $\tau_{yy}$  revealed essentially the same results as that of  $\tau_{xy}$ .) The power-law exponent of  $\tau_{xy}$  was calculated as - 0.75 over the entire data range, without much deviation from the norm. If this rotational timescale were scaling linearly with shear rate, this exponent would have been -1.0; consequently, it is apparent that the molecules within the sheared liquids are not tumbling with frequencies that are determined by the hydrodynamically imposed vorticity of the flow field. This is most likely due to the fact that over a small period of time, many of the liquid molecules are almost fully stretched at high values of  $Wi$ , and are not in the process of tumbling. As mentioned above, these fully stretched molecules dominate the statistically based averages, and could account for this discrepancy between the vorticity and the tumbling frequency; however, this type of sublinear scaling has been observed experimentally. Teixeira *et al.* (2005) observed a tumbling frequency in dilute DNA solutions that scaled as  $Wi^{0.62}$ . Hence the chain

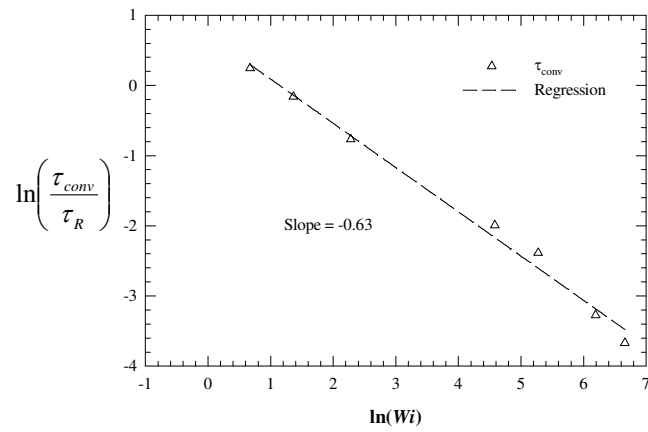
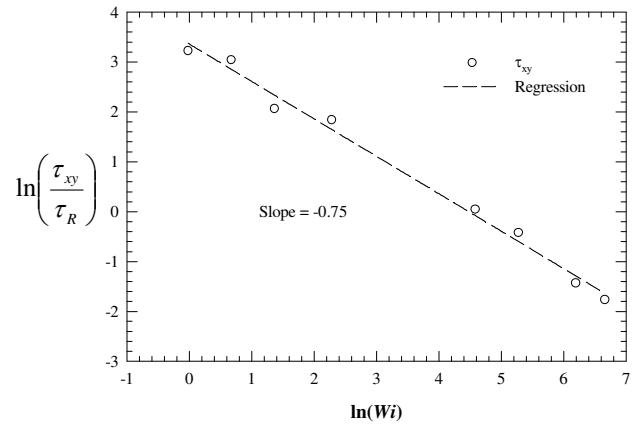


Fig. 4.3.11. Log-log plots of the characteristic timescales, relative to the Rouse time, versus  $Wi$  for the NEMD (open symbols) and BD (filled symbols) simulations. Note that plots of the characteristic frequencies would possess slopes of opposite sign but of the same absolute values as those presented in the figures.

tumbling frequency does not necessarily need to match the vorticity; however, as these solutions were dilute, it is still likely that the background solvent was evolving as dictated by the local kinematics. In other words, although the isolated chains were tumbling at frequencies other than the vorticity, the local solvent was experiencing the vorticity demanded by the shear field, barring hydrodynamic interactions between the macromolecule and the solvent. A similar regression of the BD simulation of the free-draining chain modeled in this study yielded a characteristic tumbling frequency that scaled with a factor of - 0.68.

In the NEMD simulations of the dense liquid, however, the situation is more complicated by the fact that there is no solvent, and the molecules are not isolated. In this circumstance, the hydrodynamic field is solely due to the molecules themselves, not the surrounding solvent. It is also evident from Figure 4.3.11 that  $\tau_{conv}$  scales sublinearly as  $Wi^{-0.63}$ , as fitted to a truncated Spriggs power-law equation in which  $\tau_{conv} = \tau_R$  when  $Wi < 1$ , and  $\tau_{conv} = \tau_R Wi^\alpha$  when  $Wi > 1$ . This value is very close to the value of - 0.62 observed in the experiments of Teixeira *et al.* (2005). The BD simulations of the present study provided a scaling exponent of - 0.66. This fact is either a coincidence, or hints at some underlying universal connection between the tumbling frequencies and the deformation and orientation of macromolecular chains under shear.

Partial rationalization of the similarity in the NEMD and BD results is provided by the realization that the relatively short, stiff chains in the dense liquid are not tightly coiled at equilibrium, whereas the chains in the free-draining model are assumed to be

ideal with no interactions between the beads. According to the Flory Theorem, macromolecules in dense polymer melts behave like ideal chains, similarly to dilute solutions at the theta temperature. Although the short-chain polyethylene liquid examined here is not a fully entangled system, it is still likely that the same type of screening of the long-range interactions (between beads of the same chain separated by three or more bonds) of a particular chain by neighboring and interpenetrating chains. Were the system entangled, however, it is highly likely that this quantitatively similar scaling behavior would not be evident.

Several groups of researchers have postulated a deformational dependence of the longest relaxation time,  $\tau_R$ , under application of an external flow field [Marrucci, 1996; Souvaliotis and Beris, 1992; Apelian *et al.*, 1988]. For example, Souvaliotis and Beris (1992) postulated the functional form of  $\tau_{conv} = \tau_R \left( \frac{\text{tr} \mathbf{C}}{3} \right)^k$ , where  $k$  is a negative constant and  $\mathbf{C}$  is the conformation tensor defined in Eq. (47). This power-law dependence of the relaxation time was then inserted into the pre-averaged Upper-Convected Maxwell Model, and allowed for the prediction of shear thinning in the shear viscosity. However, any connection between molecular tumbling and the degree of molecular deformation and orientation is lost through this procedure, and only the pre-averaged contributions on the longest timescale will be evident in the macroscopic model behavior. Clearly, pre-averaged theories have little possibility of capturing the dynamical tumbling phenomena that are occurring at very small time and length scales.



#### 4.4 A mean-field anisotropic diffusion model for unentangled polymeric liquids and semi-dilute solutions

In Figure 4.4.1, the  $\langle \tilde{R}_{ete}^2 \rangle$  is calculated by changing the dimensionless parameter  $\alpha$ , and plotted as a function of  $Wi$ . From the figure, it is evident that the mesoscopic model at  $\alpha = 0.6$  is best at describing the overall behavior of atomistic model. This  $\alpha$  value nearly corresponds to Doi and Edwards' result [Doi and Edwards, 1986] that the ratio of the perpendicular and parallel diffusion coefficients of a rod-like molecule is 0.5 in dilute and semi-dilute solutions. However, the continuum model at the same value of  $\alpha$  diverges from NEMD simulation data in the neighborhood where the rotational effect begins to become significant. This is an explicit demonstration that the rotational effect is not described by the continuum model. Note that  $\langle \tilde{R}_{ete}^2 \rangle$  of the mesoscopic model reaches plateau, whereas the atomistic model attains a maximum at high values of  $Wi$ . The plateau and maximum value correspond to 30% of square of the fully-stretched chain length. (The value of  $\langle \tilde{R}_{ete}^2 \rangle$  at the plateau is around 6 and the  $\tilde{R}_{max}^2$  is 20. Thus, the ratio is approximately 0.3.) In this work,  $\alpha = 0.6$  is chosen based solely on Fig. 4.4.1 and this value is subsequently used to calculate further the rheological and structural properties to compare with the NEMD simulation data and experimental results of semi-dilute DNA solutions. The rheological behavior of polymeric liquids can be expressed by the rheological materials functions, such as viscosity, normal stress coefficients, and so on. Therefore, by comparing rheological

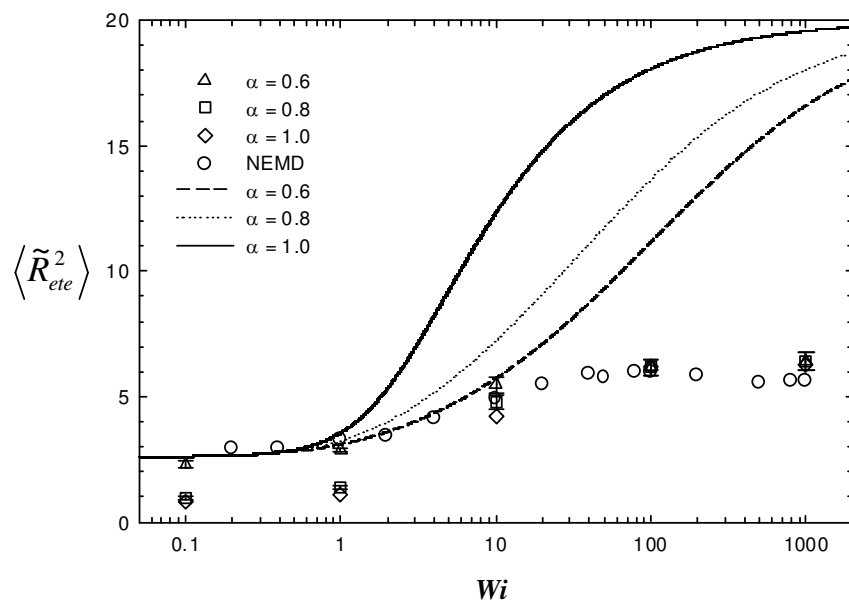


Fig. 4.4.1. The mean-square end-to-end distance,  $\langle \tilde{R}_{ete}^2 \rangle$ , for all levels as a function of  $Wi$  at various of values of  $\alpha$ . Note that in this and all subsequent figures, symbols were calculated from the mesoscopic model and lines were obtained from the continuum model, and most figures are normalized with respect to the equilibrium values.

material functions computed from our model with NEMD simulation data, the reliability of our model can be verified. Figure 4.4.2 exhibits the steady-shear viscosity as a function of  $Wi$ . Note that viscosity is normalized with respect to its zero-shear viscosity. The shear-thinning behavior is observed at all levels of description. The mesoscopic model at  $\alpha = 0.6$  is consistent with the NEMD simulation data over all values of  $Wi$  examined in the simulations. However, the continuum model at the same value of  $\alpha$  underpredicts the NEMD simulation data. In the mesoscopic and continuum models, as  $\alpha$  decreases, the viscosity becomes smaller for a given value of  $Wi$ . This is reasonable from a physical point of view. As  $\alpha$  decreases, an individual chain tends to move along its contour, which implies that the chain will experience fewer interactions with the surrounding chains, reducing frictional drag. As a result, the hydrodynamic stress imposed by the shear flow decreases and viscosity decreases with decreasing  $\alpha$  at the same value of  $Wi$ . In the continuum model, it is reasonable that the value of  $Wi$  at the onset of shear thinning behavior decreases with decreasing  $\alpha$ . The power-law index ( $b$ ) was calculated at high values of  $Wi$  at each level ( $\eta \propto \dot{\gamma}^{-b}$ ). While the power-law index is  $0.48 \pm 0.02$  in NEMD simulations, it changes with  $\alpha$  in mesoscopic and continuum models. In the mesoscopic and continuum models, the power law index decreases from 0.58 to 0.53 and from 0.83 to 0.64 as  $\alpha$  increases from 0.6 to 1.0, respectively.

Figure 4.4.3 displays the normal stress coefficients as functions of  $Wi$ . From the figure, it is evident that the first normal stress coefficient,  $\Psi_1$ , and second normal stress coefficient,  $\Psi_2$ , decrease with increasing values of  $Wi$ . In other words, the

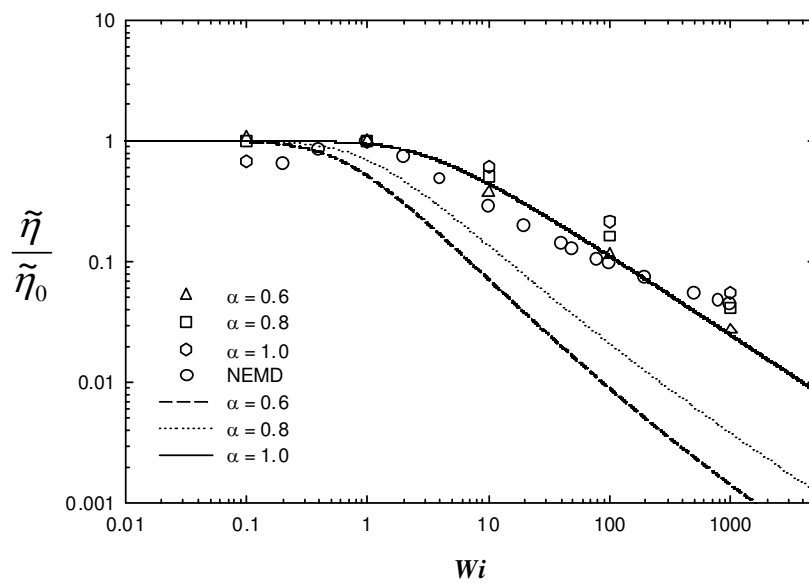


Fig. 4.4.2. The steady shear viscosity vs.  $Wi$ .

thinning behavior is observed in  $\Psi_1$  and  $\Psi_2$  for all models. In the first normal stress coefficient, the mesoscopic model at  $\alpha = 0.6$  remarkably captures the overall behavior of the NEMD simulation data over the entire range of  $Wi$ , whereas the continuum model at the same value of  $\alpha$  always underpredicts the NEMD simulation data. In the second normal stress coefficient, there is an extremely remarkable overlap between the mesoscopic model at  $\alpha = 0.6$  and NEMD simulation data in spite of the difficulty in measurement. However, the continuum model always predicts a value of zero for  $\Psi_2$ . In the mesoscopic and continuum models,  $\Psi_1$  appears to decrease with decreasing  $\alpha$  for a given value of  $Wi$ . However,  $\Psi_2$  seems to be insensitive to  $\alpha$  at the same value of  $Wi$ .

The steady-state shear stress,  $\tilde{\sigma}_{xy}$ , of mesoscopic and continuum models are plotted in Figure 4.4.4 as functions of  $Wi$  at various values of  $\alpha$ . The  $\tilde{\sigma}_{xy}$  of the semi-dilute T4 DNA solutions is displayed as a function of  $\dot{\gamma}\tau_D$ , where  $\tau_D$  is disengagement time. Note that the  $\tilde{\sigma}_{xy}$  for comparison is provided from previous experimental work on semi-dilute T4 DNA solutions instead of the NEMD simulation data and the semi-dilute T4 DNA solutions ( $C = 0.49$  mg/ml) compared in this figure have around 7-8 entanglements per chain [Jary *et al.*, 1999]. In the mesoscopic model, it seems that there are three characteristic regimes as function of  $Wi$ . In the first regime,  $\tilde{\sigma}_{xy}$  increases linearly with increasing  $Wi$ . In the second regime, the  $\tilde{\sigma}_{xy}$  increases very slowly with increasing value of  $Wi$  resulting in a characteristic slight stress plateau.

In the third regime,  $\tilde{\sigma}_{xy}$  increases again as  $Wi$  increases. This characteristic behavior of the mesoscopic model corresponds well with experimental results of semi-dilute DNA solutions [Jary *et al.*, 1999]. It is also interesting that the boundary between the first and second regimes roughly corresponds to  $Wi = 1$  where the transition between linear and nonlinear viscoelastic regimes, and the boundary between the second and third regimes located around critical value of  $Wi$  ( $Wi = 100$ ) corresponds to the point where the rotational motion of the chains begins to dominate the system response. The overall behavior of  $\tilde{\sigma}_{xy}$  is very similar between the mesoscopic model at  $\alpha = 0.6$  and the semi-dilute DNA solutions. However, the continuum model at the same value of  $\alpha$  overpredicts at low values of  $Wi$  and underpredicts beyond  $Wi = 10$ . In the mesoscopic model,  $\tilde{\sigma}_{xy}$  increases with decreasing  $\alpha$  at the same value of  $Wi$ , whereas the continuum model shows different behavior. In the continuum model, the dependence of  $\tilde{\sigma}_{xy}$  on  $\alpha$  switches at  $Wi = 1$ . While  $\tilde{\sigma}_{xy}$  also increases with decreasing  $\alpha$  for  $Wi < 1$ , it behaves in the opposite direction for  $Wi \geq 1$ . In other words,  $\tilde{\sigma}_{xy}$  increases with increasing values of  $\alpha$  in this region for a given value of  $Wi$ . Recently, Zhu *et al.* (2008) measured the rheological properties of  $\lambda$ -phase DNA solutions at various concentrations. The  $\tilde{\sigma}_{xy}$  obtained from the mesoscopic model also compared well

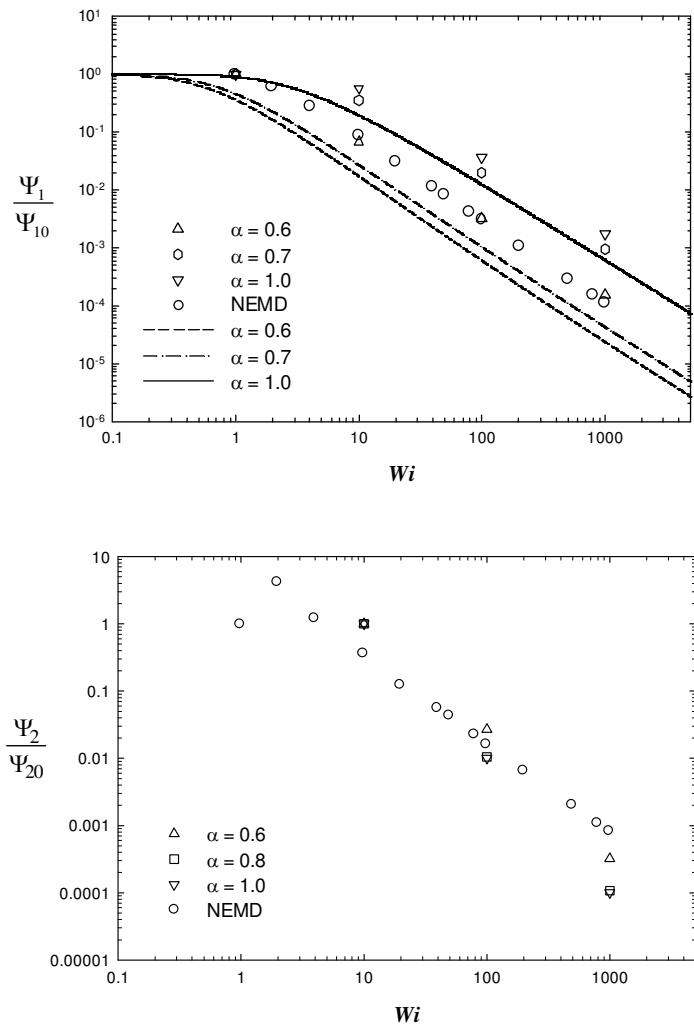


Fig. 4.4.3. The normal stress coefficients as a function of  $Wi$ .

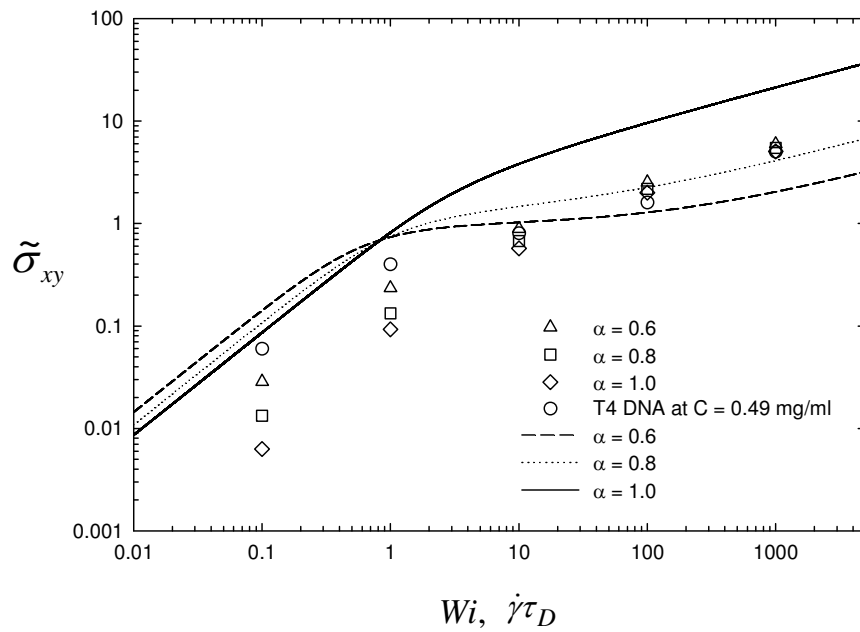


Fig. 4.4.4. Comparison of the shear stress computed from models with experimental results of semi-dilute DNA solutions as a function of  $Wi$ .



with  $\lambda$ -phase DNA solutions for further proof. The  $\tilde{\sigma}_{xy}$  of  $\lambda$ -phase DNA solutions was calculated as a function of  $Wi$  using the Cox-Merz rule [Morrison, 2001], and qualitative agreements with the results of Zhu *et al.* (2008) have been found between the mesoscopic model and experiments of  $\lambda$ -phase DNA solutions.

The orientation angle,  $\theta$ , of the mesoscopic model is displayed in Figure 4.4.5 as a function of  $Wi$ . Typically, under shear flow, the orientation angle decreases from  $45^\circ$  with increasing shear rate, and approaches a value of a few degrees above the direction of flow at high shear rates [Kroger, 2005; Baig *et al.*, 2007]. This is due to the random orientation of chains under quiescent conditions and alignment of the chain molecules in the direction of flow at high shear rates. As shown in Figure 4.4.5, the orientation angle follows typical behavior. It decreases from around  $45^\circ$  with increasing  $Wi$  and remains a few positive degrees above the direction of flow, on average, at high values of  $Wi$ . Note that the orientation angle for all  $\alpha$  is expected to converge to  $45^\circ$  at low values of  $Wi$ . In the inset of the figure, the slope of the orientation angle at  $\alpha = 0.6$  is  $-0.497$  and is very close to  $-0.46$  obtained from DNA solutions [Teixeira *et al.*, 2005].

The radius of gyration represents the size of polymeric chains. Thus, the mean configuration thickness has been calculated using the radius of gyration tensor in previous studies [Schroeder *et al.*, 2005; Teixeira *et al.*, 2005; Thomas *et al.*, 2009]. Figure 4.4.6 shows the mean molecular configuration thickness computed from the mesoscopic model as a function of  $Wi$ . It is very reasonable that the mean molecular

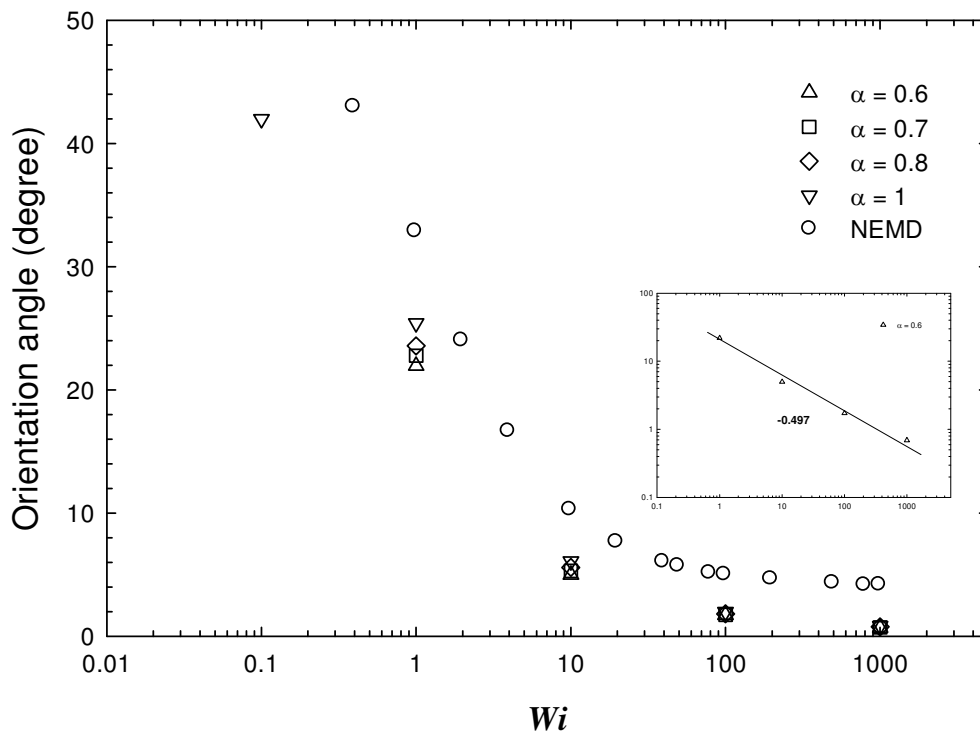


Fig. 4.4.5. The orientation angle of the mesoscopic model as a function of  $Wi$ . The inset of this figure displays the orientation angle at  $\alpha = 0.6$  vs.  $Wi$  in log-log plot.

configuration thickness in the flow direction,  $\langle \delta_x \rangle$ , exhibits very similar behavior to  $\langle \tilde{R}_{ete}^2 \rangle$ . It maintains its equilibrium value near the quiescent condition, and increases rapidly at intermediate values of  $Wi$ . At high values of  $Wi$ ,  $\langle \delta_x \rangle$  begins to plateau, as does  $\langle \tilde{R}_{ete}^2 \rangle$ . It is also evident that  $\langle \delta_x \rangle$  increases with decreasing  $\alpha$  at the same value of  $Wi$  because the chain moves along its contour more freely than in the perpendicular direction. As expected, the mean molecular configuration thickness in the flow gradient direction,  $\langle \delta_y \rangle$ , and in neutral direction,  $\langle \delta_z \rangle$ , decrease with increasing  $Wi$ . The  $\langle \delta_y \rangle$  and  $\langle \delta_z \rangle$  decrease with decreasing  $\alpha$  for a given value of  $Wi$  for the same reasons as above. It is also interesting that the slope of  $\langle \delta_y \rangle$  at  $\alpha = 0.6$  is very close to that of the DNA solutions in a previous study [Teixeira *et al.*, 2005]. They are - 0.255 and - 0.26, respectively.

Although the end-to-end distance is one of the most important properties in polymer dynamics, it is hard to measure it experimentally due to poor resolution and dimensional limitations of typical experimental devices. (In experiment, 2D images are observed instead of 3D ones.) In previous experimental studies, the projected distance  $s$  between the two farthest beads to the flow-gradient and flow-vorticity planes were calculated [Smith *et al.*, 1999; Hur *et al.*, 2001; Schroeder *et al.*, 2005; Teixeira *et al.*, 2005, 2007]. In Figure 4.4.7, the projected farthest distance between two beads on the chain at each plane is shown as a function of  $Wi$ . Reasonably, the overall

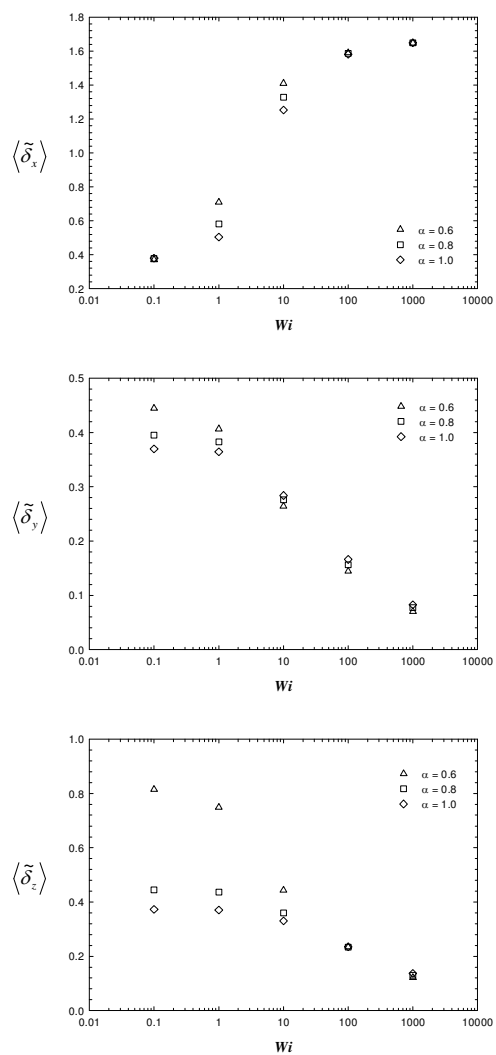


Fig. 4.4.6. Molecular configuration thickness in the mesoscopic model as a function of  $Wi$ .

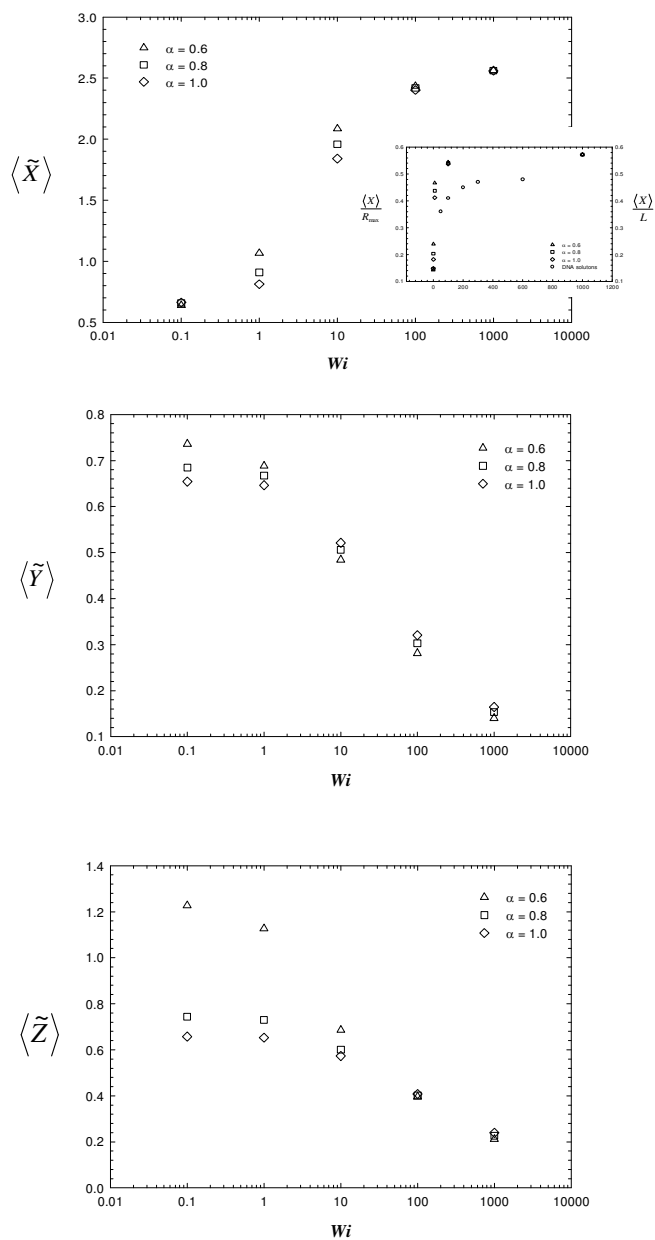


Fig. 4.4.7. The mean molecular extension in the mesoscopic model vs.  $Wi$ . The inset of this figure is the mean fractional extension vs.  $Wi$ . Note that the  $R_{max}$  is the fully-stretched chain length of the bead-spring chain and the  $L$  is the contour length of the DNA molecules.

behavior of mean molecular extension to flow-vorticity plane,  $\langle \tilde{x} \rangle$ , is qualitatively similar to  $\langle R_{ete}^2 \rangle$  and  $\langle \tilde{\delta}_x \rangle$ . It increases with increasing  $Wi$  at low values of  $Wi$ . At intermediate values of  $Wi$ ,  $\langle \tilde{\delta}_x \rangle$  increases dramatically, but it does not reach the plateau value at high values of  $Wi$ . In the inset of Figure 4.4.7, the  $\langle \tilde{x} \rangle / \tilde{R}_{max}$  is consistent with DNA solutions [Teixeira *et al.*, 2005, 2007]. The mean molecular extension in the vorticity-gradient and flow-gradient planes,  $\langle \tilde{y} \rangle$  and  $\langle \tilde{z} \rangle$ , display corresponding behavior to the  $\langle \tilde{\delta}_y \rangle$  and  $\langle \tilde{\delta}_z \rangle$  as functions of  $Wi$ : they decrease with increasing  $Wi$ . The dependence of the mean molecular extension,  $\langle \tilde{x} \rangle$ ,  $\langle \tilde{y} \rangle$ , and  $\langle \tilde{z} \rangle$ , on  $\alpha$  exhibits the same behavior as the mean configuration thickness,  $\langle \tilde{\delta}_x \rangle$ ,  $\langle \tilde{\delta}_y \rangle$ , and  $\langle \tilde{\delta}_z \rangle$ , respectively.

The conformation tensor is not only the simplest descriptor of polymer chain configurational properties, but also one of the most important properties in characterizing polymeric materials under flow conditions since it has information regarding both the orientation and extension of the constituent chains [Beris and Edwards, 1994]. Note that conformation tensor is the unit tensor under equilibrium conditions. The conformation tensor components are shown in Figure 4.4.8. The mesoscopic and continuum models are displayed at  $\alpha = 0.6$  in this figure. It is reasonable that the overall behavior of  $\tilde{C}_{xx}$  is very similar to  $\langle \tilde{R}_{ete}^2 \rangle$ . At low values

of  $Wi$ ,  $\tilde{C}_{xx}$  increases with increasing  $Wi$  due to the alignment and extension of chain molecules. At high values of  $Wi$ , the mesoscopic model achieved values corresponding to 30% of square of the fully-stretched chain length due to the rotational motion of the chains, whereas the continuum model approached to fully-stretched chain length. This provides direct evidence that the rotational effect is not accounted for in the continuum model. Note that the continuum model diverges from the NEMD simulation data beyond  $Wi = 10$ . It is also obvious that  $\tilde{C}_{yy}$  decreases with increasing  $Wi$  since chains are compressed in flow gradient direction under shear flow. The  $\tilde{C}_{zz}$  component also decreases with increasing  $Wi$  because the chains are stretched and aligned with respect to the flow direction. The dimensionless parameter  $\alpha$ , which is ratio of the perpendicular and parallel diffusion coefficients, becomes 1 as  $Wi$  approaches zero since the anisotropic diffusion tensor reduces to the isotropic diffusion tensor under equilibrium conditions. However,  $\alpha$  has a constant value in the mesoscopic model over the entire range of  $Wi$ . Thus,  $\tilde{C}_{yy}$  and  $\tilde{C}_{zz}$  do not approach the appropriate values near equilibrium conditions in this model. Further refinement of this model would include a  $Wi$ -dependent  $\alpha$ , however, the dynamical effects that we are interested in currently, are at high values of  $Wi$ , where this issue is not present. In the mesoscopic and continuum models, the overall behavior of  $\tilde{C}_{xy}$  is very similar to that of the NEMD simulation. The continuum model overpredicts the NEMD simulation data, whereas the mesoscopic model underpredicts the NEMD

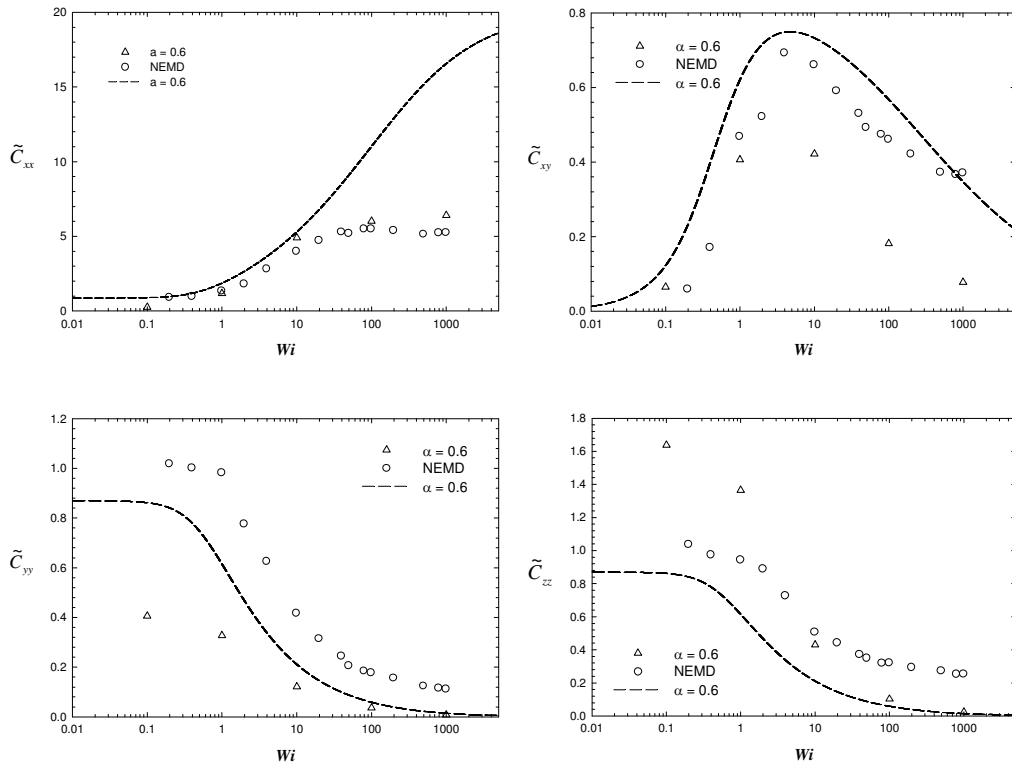


Fig. 4.4.8. The non-zero components of the conformation tensor as function of  $Wi$ .



simulation data at the same value of  $Wi$ . Interestingly, the continuum model in the  $\tilde{C}_{yy}$ ,  $\tilde{C}_{zz}$ , and  $\tilde{C}_{xy}$  plots is closer to the NEMD simulation data than mesoscopic model. However, the magnitude should be considered between  $\tilde{C}_{xx}$  and the other components in these plots.

As stated before, the dimensionless parameter  $\alpha$  is the ratio of the perpendicular and parallel diffusion coefficients ( $\alpha = \Lambda_{\perp} / \Lambda_{\parallel}$ ). When  $\alpha = 1$ , the anisotropic diffusion tensor reduces to an isotropic diffusion tensor. When  $0 < \alpha < 1$ , parallel diffusion is preferred. Thus, it is very meaningful to examine the dependence of the probability distribution of  $|\mathbf{R}_{ete}|$  on  $\alpha$  in the mesoscopic model. In Figure 4.4.10, two values of  $\alpha$  were chosen: one with isotropic diffusion tensor ( $\alpha = 1$ ), and one with anisotropic diffusion tensor ( $\alpha = 0.6$ ). For the isotropic diffusion tensor ( $\alpha = 1$ ), the probability distributions exhibit typical overall behavior of dilute solutions [Smith *et al.*, 1999; Hur *et al.*, 2001; Teixeira *et al.*, 2007]. It follows Gaussian behavior at low values of  $Wi$ , and becomes wide at intermediate values of  $Wi$ . At high values of  $Wi$ , the probability distributions display bimodal behavior with stretch and rotational peaks. At high shear rates, the different qualitative behavior of distribution (bimodal and wide spread) between our simulation and previous studies are caused by bin size. If we increase the bin size in the bead-rod model of Section 4.3, we observe the typical widely spread distribution in Fig. 4.4.9.

For the anisotropic diffusion tensor ( $\alpha = 0.6$ ), the probability distribution displays different behavior compared to dilute solutions or the isotropic diffusion

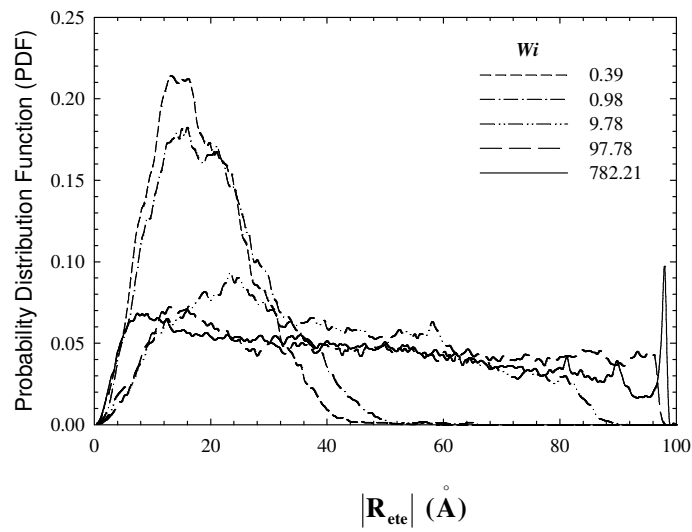
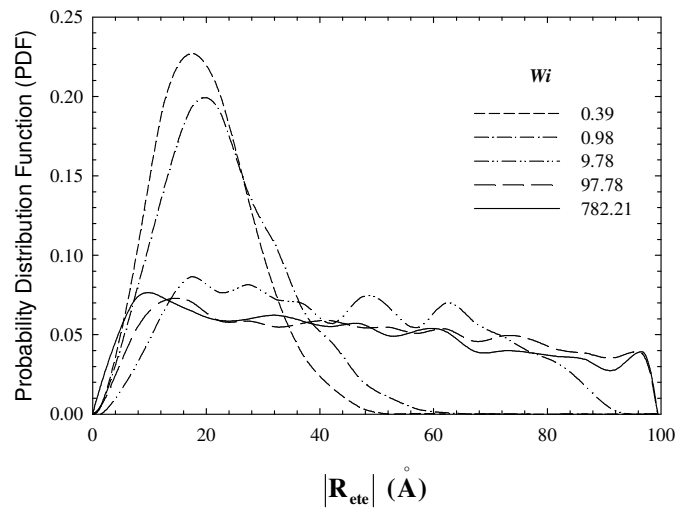


Fig. 4.4.9. Same probability distribution functions of a bead-rod chain vs.  $|\mathbf{R}_{ete}|$  at five values of  $Wi$  with different bin sizes. Fig. 4.4.9 (b) has the smaller bin size than Fig. 4.4.9 (a).

tensor model. Although it maintains the Gaussian character at low values of  $Wi$ , the entire width of the distributions becomes wider and the peaks of the distributions lower in height compared to the isotropic diffusion tensor. It is reasonable that the anisotropic diffusion, where chains are diffusing along their contours, results in this change of shape of the probability distribution. Since parallel diffusion is preferred, the number of chains with extended lengths should increase. At intermediate values of  $Wi$ , the shape of the probability distribution is no longer Gaussian. At high values of  $Wi$ , the bimodal behavior is also observed with stretch and rotational peaks for the anisotropic diffusion tensor ( $\alpha = 0.6$ ). It is very interesting that the overall behavior of the probability distribution depends on  $\alpha$  at low and intermediate values of  $Wi$ , whereas it is independent of  $\alpha$  at high values of  $Wi$ . This might be related to a competition between the entropic spring effect (deformation of the chains) and hydrodynamic drag imposed by shear flow (rotational motion of the chain) on system response. At low values of  $Wi$ , the system response is dominated by the entropic spring effect since the hydrodynamic drag imposed by shear flow (or vorticity) is weak. The entropic spring effect is thus strongly affected by the anisotropic diffusion matrix. Hence, the probability distribution depends to some degree on  $\alpha$  in this  $Wi$  regime. However, at high values of  $Wi$ , the hydrodynamic drag imposed by strong shear flow overcomes the entropic spring effect. Hence, only the rotational motion of the chains dominates the system response and the probability distribution is independent of  $\alpha$ .

The probability distributions of the mesoscopic model at  $\alpha = 0.6$  are also compared with NEMD simulation data in this figure since it predicted well other

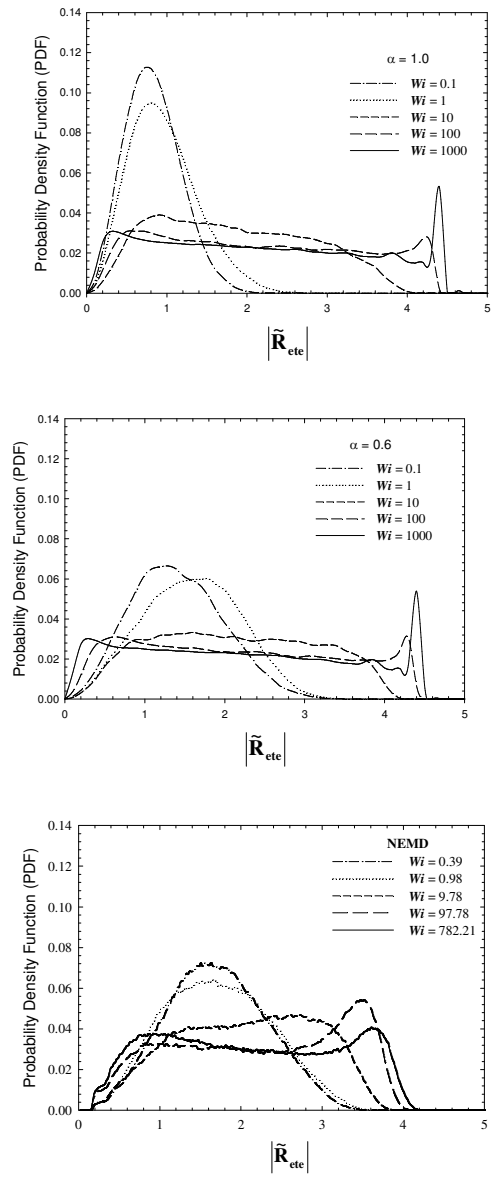


Fig. 4.4.10. The probability distribution of the NEMD simulations and the mesoscopic model vs.  $|\tilde{\mathbf{R}}_{ete}|$ .

rheological and structural properties of the NEMD simulations. As expected, the probability distributions of the mesoscopic model at  $\alpha = 0.6$  show very similar behavior to the NEMD simulations. Especially, the probability distributions at low values of  $Wi$  considerably resemble NEMD simulation data. For example, the width of the probability distribution for  $Wi = 1$  is roughly the same between the mesoscopic model and the NEMD simulations. Note that the peak is much narrower for the isotropic diffusion tensor ( $\alpha = 1$ ) than the NEMD simulations. At intermediate values of  $Wi$ , the overall shape of the probability distributions are very similar between the mesoscopic model at  $\alpha = 0.6$  and the NEMD simulations. However, the probability distribution of the NEMD simulations is slightly biased to higher  $|\mathbf{R}_{ete}|$  compared to the mesoscopic model. At high values of  $Wi$ , the bimodal behavior with stretch and rotational peaks is observed in both simulations.

Time correlation functions of the components of the end-to-end vector provide significant characteristic time scales of the system response through Fourier transform of the correlation signal. Thus, rheological and structural responses of the mesoscopic model can be confirmed by comparing characteristic time scales between the mesoscopic model and NEMD simulation data. Figure 4.4.11 exhibits time correlation functions of the  $xx$  component of the end-to-end vector,  $\tilde{\mathbf{R}}_{ete}$ , as functions of observation time,  $\tilde{t}$ . The correlation curves of the mesoscopic model show similar behavior to the NEMD simulations at corresponding values of  $Wi$ . For example, the correlation curves of the mesoscopic model display typical exponential

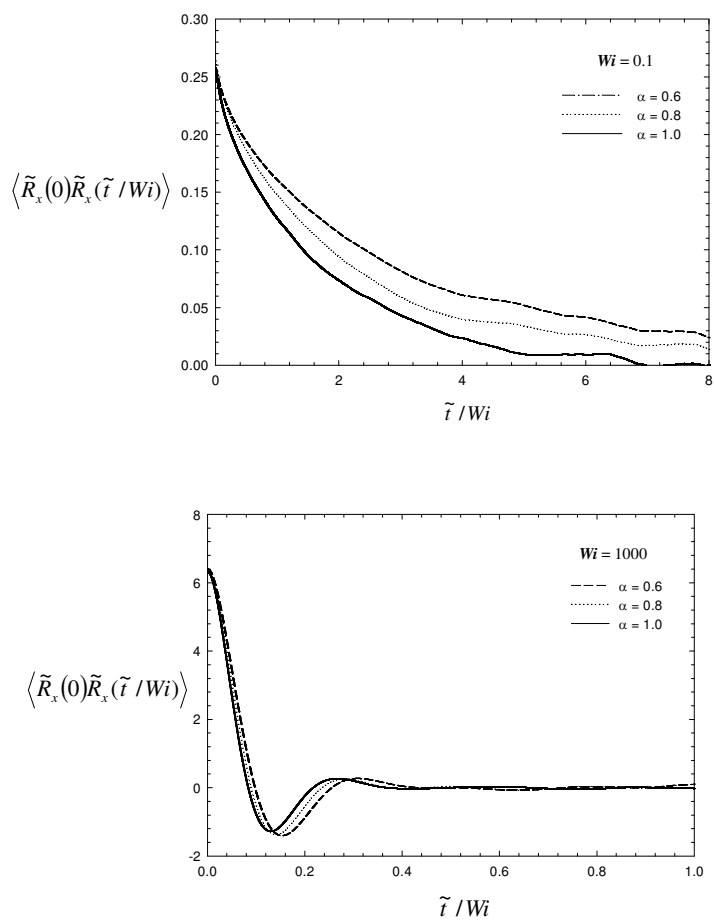


Fig. 4.4.11. The time correlation functions of  $xx$  component of the  $\tilde{\mathbf{R}}_{ete}$  vs. observation time at  $Wi = 0.1$  and  $Wi = 1000$ .

decay for  $Wi < 2$ , and exhibit a characteristic minimum, local maximum, and damped oscillatory behavior at longer times for  $Wi \geq 2$ . Note that the slope of the decay at low values of  $Wi$  and the appearance of characteristic minimum at high values of  $Wi$  depend on  $\alpha$ .

In Figure 4.4.12, the characteristic time scales are displayed as functions of  $Wi$ . In this figure,  $\tau_R$  denotes the longest relaxation time (Rouse time) and  $\tau_{xx}$  refers to the characteristic time scales extracted from the correlation of  $xx$  components of  $\tilde{\mathbf{R}}_{ete}$ . More detailed explanations regarding characteristic time scales have been already discussed in Section 4.3. Note that the characteristic time scales of the mesoscopic model were normalized by the Rouse time at  $\alpha = 0.6$ . For  $Wi < 2$ , the characteristic time scales were extracted by fitting the time correlation of the end-to-end vector with an exponential. On the other hand, the power spectral density function through Fourier transform of the correlation signal was used to extract the characteristic time scales for  $Wi \geq 2$ .

There are two regimes in Figure 4.4.12. In the first regime ( $Wi < 2$ ), the characteristic time scales of the mesoscopic model converge to the Rouse time near quiescent conditions. However, they increase with increasing  $Wi$ . In addition, the characteristic time scales become larger with decreasing  $\alpha$  at the same value of  $Wi$ . This might be related to the entropic spring effect. With decreasing  $\alpha$  and increasing  $Wi$ , the bead-spring chain moves more easily in the parallel direction, and is slightly stretched from its equilibrium chain length, respectively. Thus, a given chain has a slightly longer correlation time. As a result, the characteristic time scales

increase with increasing  $Wi$  and decreasing  $\alpha$ . The previous results of the bead-rod chains in Section 4.3 also support this assumption. In the bead-rod chain model, the characteristic time scales maintain nearly constant values since the bead-rod chain might not admit small bond extensions caused by weak shear flow. In the second regime ( $Wi \geq 2$ ), the characteristic time scales of the mesoscopic model almost overlap with the NEMD simulation data, and are independent of  $\alpha$ . The same explanation regarding the behavior of the probability distribution as a function of  $Wi$  can be applied here. For  $Wi < 2$ , the entropic spring effect or deformation of chains controls the system response since the rotational motion of chains caused by shear flow is insignificant. Thus, the characteristic time scales are influenced by  $\alpha$ . However, for  $Wi \geq 2$ , the rotational motion of chains imposed by shear flow begins and then eventually dominates the entropic spring effect or deformation of chains on the system response at high values of  $Wi$ . Thus, the characteristic time scales are independent of  $\alpha$ . This suggests a conjecture that the characteristic power-law exponents of the time scales as function of  $Wi$  and independent of the exact nature of the “reptation tube”.

According to Doi and Edwards (1986), there is a possibilities that the characteristic time scales  $\tau_{xx}$  and  $\tau_{yy}$  can be related to parallel and perpendicular diffusion coefficients, respectively. In Doi and Edwards’ results of rod-like polymers in dilute and semi-dilute solutions, the ratio of the parallel and perpendicular diffusion coefficients is 0.5. The ratio of  $\tau_{xx}$  and  $\tau_{yy}$  obtained from NEMD simulation is 0.6-0.7, and is very close to Doi and Edwards’ result. Furthermore, this ratio is also



very similar to  $\alpha = 0.6$  for the mesoscopic model which captures well the NEMD simulation data. Thus, it is reasonable that the characteristic time scale  $\tau_{xx}$  is related to parallel diffusion and the characteristic time scale  $\tau_{yy}$  corresponds to perpendicular diffusion.

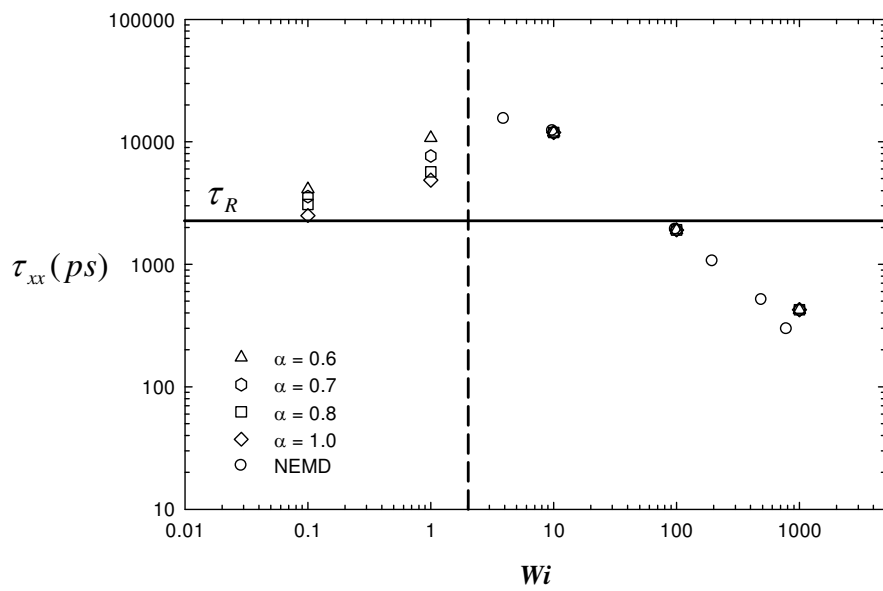


Fig. 4.4.12. The characteristic time scale,  $\tau_{xx}$ , as a function of  $Wi$ .

## Chapter V Summary and Conclusion

At the atomistic level of description, NEMD simulations of linear short-chain polyethylene liquids were performed under shear and planar elongational flows to collect fundamental rheological and structural properties and to examine entanglement characteristics. The viscosities for both flow fields became larger as the chain length increased. Thinning behavior with strain rate in these liquids was observed under both shear and PEF. The zero shear-rate viscosity for these polyethylene liquids was approximately equal to the zero elongation-rate viscosity, as predicted from Trouton's rule. All viscosities followed the power-law model. Although the power-law index of  $\eta_1$  under PEF increased as the chain length increased, it was independent of chain length under shear.

From a microscopic viewpoint, the pressure is determined from potential and kinetic contributions. The intermolecular LJ potential energy appears to dominate the potential contribution to pressure, and therefore bears a close relationship to the mean pressure since the kinetic contribution is linear in particle density, and thus small for the dense liquid under examination here. The behavior observed for the mean pressure and the intermolecular LJ potential displayed a distinct correlation for all polyethylene liquids. Similarly, the behavior of  $\langle R_{ete}^2 \rangle$  and  $\langle R_g^2 \rangle$  seemed to correlate with the intramolecular LJ potential energy for all liquids.

The global and local chain flexibilities were examined by investigating the bond-torsional, bond-bending, and bond-stretching energies per mode. As might be

expected, the chains are highly flexible at low strain rates, but become fairly stiff at the very highest strain rates simulated. Some quantitative measures of the shear and extensional flow-induced variations in the number of topological constraints were also presented. Although the simulated systems must be considered as unentangled, since their molecular weight is below the known critical entanglement molecular weight for polyethylene liquids [Foteinopoulou *et al.*, 2006; Tzoumanekas and Theodorou, 2006; Kröger, 2005; Kröger and Hess, 2000], there is reason to believe that the transient behavior should have been captured qualitatively by the present results, and should remain to some extent unaffected also for liquids with larger molecular weights. Some of the depicted results for viscosities, pressure, and energies resemble behavior observed for more coarse-grained models, such as the anharmonic multibead spring model [Kröger, 2005]. Such evidence, substantiated through the present study, could be used to motivate replacing the atomistically detailed, and computationally demanding SKS model with a coarse-grained one. This would allow the attainment of the fully entangled state, for which structure-property relationships are still required to test theoretical approaches [Öttinger, 1999; Fang, 2000; Nair and Schieber, 2006], or the dynamics of the entanglement network.

Understanding the dynamics of the entanglement network subject to flow conditions will help to establish new multiscale methods for describing the dynamics of polymeric liquids, in which not only the atomistic configuration is mapped to a network, but the reverse operation needs to be established. The present work

demonstrated the feasibility of this approach concerning the accumulation of reference data for two relevant, ‘orthogonal’ flow types, from atomistically detailed simulations.

At the mesoscopic level of description, Brownian dynamics simulations of a free-draining bead-rod model with equivalent contour length to linear  $C_{78}H_{158}$  were performed to examine the motion of individual molecules as a function of shear rate. In this work, the Brownian dynamics simulations of the bead-rod model were used to describe dilute solutions and nonequilibrium molecular dynamics was used to simulate the dense liquids. The mean-squared, end-to-end vector,  $\langle R_{ete}^2 \rangle$ , was shown to increase from its equilibrium value to attain a maximum at high shear rates. Moore *et al.* (2000) hypothesized that this effect was due to a competition between chain stretch/alignment, and a Brownian-like collisional force. However, the present study suggested that the rotational motion of the chain molecules is primarily responsible for this peculiar behavior.

Both NEMD and BD simulations revealed a probability distribution of  $|R_{ete}|$  that was Gaussian at low Weissenberg number ( $Wi$ ); however, non-Gaussian behavior was evident at intermediate values of  $Wi$ , in contrast to the predictions of pre-averaged theories. At high  $Wi$ , the NEMD distribution was bimodal, with two distinct peaks associated with rotation (low  $Wi$  peak) and stretching (high  $Wi$  peak). The BD simulations of the free-draining chain exhibited a non-Gaussian and very wide distribution of chain lengths, with the absolute width increasing dramatically with increasing  $Wi$  as chain rotation became increasingly significant. Time correlations

between the components of  $R_{ete}$  of the dense liquid used in the NEMD simulations exhibited characteristic tumbling frequencies that scaled as  $Wi^{0.75}$  power. An additional characteristic timescale appeared after a critical  $Wi$  of about 2, which scaled as  $Wi^{-0.63}$ . The BD simulations also exhibited characteristic timescales, which scaled as  $Wi^{-0.68}$  and  $Wi^{-0.66}$ . The scaling behavior of these timescales is consistent with experimental values reported by Teixeira *et al.* (2005).

Time trajectories of individual chain  $|R_{ete}|$  values and orientation angles revealed a dramatic onset of tumbling behavior of the chains at a critical  $Wi$  ( $\sim 2$ ). Auto-correlations and cross-correlations between the components of  $R_{ete}$  revealed characteristic frequencies of molecular rotation, which scaled as  $Wi^{-0.75}$  power. Furthermore, after a critical  $Wi$  of approximately 2, another characteristic timescale appeared which scaled as  $Wi^{-0.63}$ . This was associated with a dramatic decrease in the elastic response of the system, which was apparently associated with the relaxation of rotational constraints and the decorrelation of the tumbling cycles (resulting in the first peak of the bimodal probability distribution) due to the formation of loosely-defined, tube-like structures of fully-stretched neighboring chains (comprising the second peak of the distribution). Although the free-draining solution is very different in character than the dense liquid, the BD simulations revealed a similar behavior, with the characteristic timescales mentioned above scaling as  $Wi^{-0.68}$  and  $Wi^{-0.66}$ , respectively. Individual chain configurations were explored as functions of  $Wi$  and  $|R_{ete}|$ ; NEMD and BD simulations provided similar results at high values of  $Wi$ , both qualitatively

and quantitatively. At low values of  $|\mathbf{R}_{ete}|$ , the chain configurations were predominantly coiled at low  $Wi$  and folded at high  $Wi$ , indicating increasingly hairpin-like rotation with growing shear strength. At high values of  $|\mathbf{R}_{ete}|$ , the chain configurations were essentially either fully stretched or of half-dumbbell nature at high  $Wi$ , thus constituting a loose network of tube-like structures.

Based on enormous information on the dynamics of linear, short-chain polyethylene liquids, a coarse-grained mesoscopic model was proposed and compared with NEMD simulation data of linear, short-chain liquids and experiments of semi-dilute DNA solutions under shear flow. Moreover, this model was further coarse-grained to the continuum level through pre-averaging.

The  $\langle \tilde{R}_{ete}^2 \rangle$  of the mesoscopic model at  $\alpha = 0.6$  was remarkably consistent with NEMD simulation data. However, the continuum model at the same value of  $\alpha$  diverged from NEMD simulation data beyond a critical value of  $Wi$  and reached the fully-stretched chain length at high values of  $Wi$ . This is a direct demonstration that the rotational effect is absent in the continuum model. In addition, the value of the dimensionless parameter ( $\alpha = 0.6$ ) is very similar to Doi and Edwards' result of rod-like chains in dilute and semi-dilute solutions, which is 0.5. The steady shear viscosity displayed well shear-thinning behavior. The mesoscopic model at  $\alpha = 0.6$  agreed well NEMD simulation data. However, the continuum model at the same value of  $\alpha$  underpredicted NEMD simulation data. In the mesoscopic and continuum models, the viscosity depended on  $\alpha$  at the same value of  $Wi$ . Although

power-law behavior was observed in all models, the power-law index ( $b$ ) was different in each case. The first and second normal stress coefficients,  $\Psi_1$  and  $\Psi_2$ , exhibited thinning behavior. Also the mesoscopic model at  $\alpha = 0.6$  captured well the overall behavior of  $\Psi_1$  and  $\Psi_2$ . However, the continuum model at the same value of  $\alpha$  for  $\Psi_1$  underpredicted the NEMD simulation data and the continuum model for  $\Psi_2$  was zero, as expected.

The steady-state shear stress,  $\tilde{\sigma}_{xy}$ , of the mesoscopic and continuum models was compared with experiments of semi-dilute DNA solutions. It seems that three characteristic regimes of the mesoscopic model correspond well with data of semi-dilute DNA solutions, and the overall behavior of  $\tilde{\sigma}_{xy}$  was very similar between the mesoscopic model  $\alpha = 0.6$  and the semi-dilute DNA solutions. However, the dependence of  $\tilde{\sigma}_{xy}$  on  $\alpha$  was different between the mesoscopic and continuum models. The orientation angle,  $\theta$ , of the mesoscopic model displayed the typical behavior under shear flow: it decreased from  $45^\circ$  with increasing  $Wi$  and eventually formed a small positive angle with respect to the flow direction at high values of  $Wi$ . The orientation angle of the mesoscopic model at  $\alpha = 0.6$  scaled as  $\langle \theta \rangle \propto Wi^{-0.497}$ , and, interestingly, compared well with DNA solution results, which were given by  $\langle \theta \rangle \propto Wi^{-0.46 \pm 0.04}$ .

The mean configurational thickness and mean molecular extension of the mesoscopic model showed similar behavior as functions of  $Wi$ . The  $\langle \delta_x \rangle$  and  $\langle x \rangle$



increased with increasing  $Wi$ , and reached plateaus at high values of  $Wi$ . On the other hand,  $\langle \delta_y \rangle$  and  $\langle y \rangle$  decreased with increasing  $Wi$ , and  $\langle \delta_z \rangle$  and  $\langle z \rangle$  exhibited similar behavior. The dependence of both properties on  $\alpha$  was also very similar. It was very interesting that the slope of  $\langle \delta_y \rangle$  at  $\alpha = 0.6$  was very close to that of the DNA solutions in the previous study, and the ratio  $\langle x \rangle / R_{max}$  was consistent with the DNA solutions also.

The conformation tensors of the mesoscopic and continuum models at  $\alpha = 0.6$  were examined as functions of  $Wi$ . As expected,  $C_{xx}$  of the mesoscopic model behaved very similar to  $\langle \tilde{R}_{ele}^2 \rangle$ . However,  $C_{xx}$  of the continuum model diverged from NEMD simulation data in the  $Wi$  range where the rotational effect became important. In the mesoscopic and continuum models, the  $C_{yy}$  and  $C_{zz}$  components decreased with increasing  $Wi$ , and  $C_{xy}$  was very closed to NEMD simulation data.

The influence of  $\alpha$  on the probability distribution functions of the mesoscopic model was examined. Although the probability distributions attained from both isotropic and anisotropic diffusion tensors showed Gaussian characteristic at low values of  $Wi$ , the characteristic shapes were different each other. All probability distributions obtained from the anisotropic diffusion tensor became wider, and lowered in height compared to probability distributions calculated from the isotropic diffusion tensor. At high values of  $Wi$ , the probability distributions obtained from both isotropic and anisotropic diffusion tensors exhibited bimodal behavior with both

stretch and rotational peaks. This can be explained by a competition between the entropic spring effect and hydrodynamic drag imposed by shear flow. The probability distributions of the mesoscopic model were also considerably similar to that of the NEMD simulations. The characteristic time scales were extracted and plotted as functions of  $Wi$ . There were two regimes of characteristic time scales vs.  $Wi$ . In the first regime ( $Wi < 2$ ), the characteristic time scales recovered the longest rotational relaxation time (Rouse time) near equilibrium. However, they increased with increasing  $Wi$ , and were heavily influenced by  $\alpha$ . In the second regime ( $Wi > 2$ ), the characteristic time scales overlapped with the NEMD simulation data, and were independent of  $\alpha$ . This kind of behavior of characteristic time scales at low and high values of  $Wi$  might be related to the competition between the entropic spring effect and hydrodynamic drag imposed by shear flow.

The coarse-grained mesoscopic model revealed quantitative agreement with NEMD simulation of linear short-chain polyethylene liquids and experiments of semi-dilute DNA solutions in the rheological and structural properties such as viscosity, normal stress coefficients, and so on. In addition, the characteristic time scales of this model were similar to NEMD simulation data. Thus, it is reasonable to conclude that the coarse-grained mesoscopic model proposed in this study is able to describe the dynamics of unentangled polymeric liquids and semi-dilute solutions under shear flow. However, the continuum model, which is further coarse-grained from mesoscopic model through pre-averaging, is not appropriate to express the dynamical behavior of polymeric liquids since the rotational effect is absent.

## **References**

- Aris, R., *Vectors, Tensors, and the Basic Equations of Fluid Mechanics* (Dover Publications, New York, 1989).
- Apelian, M.R., R.C. Armstrong, and R.A. Brown, Impact of the constitutive equation and singularity on the calculation of stick-slip flow: The modified upper-convected maxwell model (mucm), *J. Non-Newtonian Fluid Mech.* **27**, 299-321 (1988).
- Aust, C., S. Hess, and M. Kröger, Rotation and deformation of a finitely extendable flexible polymer molecule in a steady shear flow, *Macromolecules* **35**, 8621-8630 (2002).
- Baig, C., B.J. Edwards, D.J. Keffer, and H.D. Cochran, A proper approach for nonequilibrium molecular dynamics simulations of planar elongational flow, *J. Chem. Phys.*, **122**, 114103 (2005a).
- Baig, C., B.J. Edwards, D.J. Keffer, and H. D. Cochran, Rheological and structural studies of liquid decane, hexadecane, and tetracosane under planar elongational flow using nonequilibrium molecular dynamics simulations, *J. Chem. Phys.* **122**, 184906 (2005b).
- Baig, C., B. Jiang, B.J. Edwards, and D.J. Keffer, and H.D. Cochran, A comparison of simple rheological models and simulation data of n-hexadecane under shear and elongational flow, *J. Rheol.* **50**, 625-640 (2006a).
- Baig, C., B.J. Edwards, D.J. Keffer, H.D. Cochran, and V.A. Harmandaris, Rheological and structural studies of linear polyethylene melts under planar elongational flow using nonequilibrium molecular dynamics simulations, *J. Chem. Phys.* **124**, 084902 (2006b).
- Baig, C., B.J. Edwards, and D.J. Keffer, A molecular dynamics study of the stress-optical behavior of a linear short-chain polyethylene melt under shear, *Rheologica Acta* **46**, 1171-1186 (2007).

- Baig, C., and V.G. Mavrantzas, Multiscale simulation of polymer melt viscoelasticity: Expanded-ensemble Monte Carlo coupled with atomistic Nonequilibrium molecular dynamics, *Phys. Rev. B* **79**, 144302 (2009).
- Beris, A. and B.J. Edwards, *Thermodynamics of Flowing Systems* (Oxford University Press, New York, 1994).
- Bird, R.B., R.C. Armstrong, and O. Hassager, *Dynamics of Polymeric Liquids, Vol. I* (Wiley, New York, 1987a).
- Bird, R.B., C.F. Curtiss, R.C. Armstrong, and O. Hassager, *Dynamics of Polymeric Liquids, Vol. II* (Wiley, New York, 1987b).
- Cui, S.T., P.T. Cummings, and H.D. Cochran, Multiple time step nonequilibrium molecular dynamics simulation of the rheological properties of liquid *n*-decane, *J. Chem. Phys.* **104**, 225-262 (1996).
- Daivis, P.J. and B.D. Todd, A simple, direct derivation and proof of the validity of the SLLOD equations of motion for generalized homogeneous flows, *J. Chem. Phys.* **124**, 194103 (2006).
- Dambal, A., A. Kushwaha, and E.S.G. Shaqfeh, Slip-link simulations of entangled, finitely extensible, wormlike chains in shear flow, *Macromolecules*, **42**, 7168–7183 (2009)
- Deschenes, L.A., and D.A. Vanden Bout, Single-molecule studies of heterogeneous dynamics in polymer melts near the glass transition, *Science* **292**, 255-258 (2001).
- Doyle, P. S., E.S.G. Shaqfeh, and A.P. Gast, Dynamic simulation of freely draining flexible polymers in steady linear flows, *J. Fluid Mech.* **334**, 251-291 (1997).

- Doi, M. and S.F. Edwards, *The Theory of Polymer Dynamics* (Clarendon Press, Oxford, 1986).
- Doi, M., Molecular dynamics and rheological properties of concentrated solutions of rodlike polymers in isotropic and liquid crystalline phases, *J. Polym. Sci., Polym. Phys.* **19**, 229-243 (1981).
- Dunstan, D.E., E.K. Hill, and Y. Wei, Direct measurement of polydiacetylene 4-butoxycarbonylmethylurethane segment orientation and distortion in shear: Semidilute solutions, *Macromolecules* **37**, 1663-1665 (2004).
- Edwards, B.J., C. Baig, and D.J. Keffer, A validation of the p-SLLOD equations of motion for homogeneous steady-state flows, *J. Chem. Phys.* **124**, 194104 (2006).
- Edwards, B.J., C. Baig, and D.J. Keffer, An examination of the validity of non-equilibrium molecular dynamics simulation algorithms for arbitrary steady-state flows, *J. Chem. Phys.* **123**, 114106 (2005).
- Edwards, B.J. and M. Dressler, A reversible problem in non-equilibrium thermodynamics: Hamiltonian evolution equations for non-equilibrium molecular dynamics simulations, *J. Non-Newtonian Fluid Mech.* **96**, 163-175 (2001).
- Edwards, B.J. and H.C. Öttinger, Time/structure invariance criteria for closure approximations, *Phys. Rev. E* **56**, 4097-4103 (1997).
- Edwards, S.F., and Th. Vilgis, The effect of entanglements in rubber elasticity, *Polymer*, **27**, 483-492 (1986).
- Evans, D.J. and G.P. Morriss, *Statistical Mechanics of Nonequilibrium Liquids* (Academic Press, New York, 1990).

- Fang, J., M. Kröger, H.C. Öttinger, A thermodynamically admissible reptation model for fast flows of entangled polymers. II. Model predictions for shear and extensional flows, *J. Rheol.* **44**, 1293-1317 (2000).
- Flyvbjerg, H., and H.G. Petersen, Error estimates on averages of correlated data, *J. Chem. Phys.* **91**, 461-466 (1989).
- Foteinopoulou, K., N.C. Karayiannis, V.G. Mavrantzas, and M. Kröger, Primitive path identification and entanglement statistics in polymer melts: Results from direct topological analysis on atomistic polyethylene models, *Macromolecules* **39**, 4207-4216 (2006).
- Fuller, G.G., *Optical rheometry of complex fluids* (Oxford university press, New York, 1995).
- Grassia, P., and E.J. Hinch, Computer simulations of polymer chain relaxation via Brownian motion, *J. Fluid Mech.* **308**, 255-288 (1996).
- Harmandaris, V.A., N.P. Adhikari, N.F.A. van der Vegt, and K. Kremer, Hierarchical modeling of polystyrene: from Atomistic to coarse-grained Simulations, *Macromolecules*, **39**, 6708-6719 (2006)
- Hur, J. S., E.S.G. Shaqfeh, H.P. Babcock, D.E. Smith, and S. Chu, Dynamics of dilute and semidilute DNA solutions in the start-up of shear flow, *J. Rheol.* **45**, 421-450 (2001).
- Irving, J.H. and J. G. Kirkwood, The statistical mechanical theory of transport processes. 4. The equations of hydrodynamics, *J. Chem. Phys.* **18**, 817-829 (1950).
- Ionescu, T.C., C. Baig, B.J. Edwards, D.J. Keffer, and A. Habenschuss, Structure formation under steady-state isothermal planar elongational flow of *n*-eicosane:

- a comparison between simulation and experiment, *Phys. Rev. Lett.* **96**, 037802 (2006).
- Jorgensen, W.L., J.D. Madura, and C.J. Swenson, Optimized intermolecular potential functions for liquid hydrocarbons, *J. Am. Chem. Soc.* **106**, 6638-6646 (1984).
- Kraynik, A.M. and D.A. Reinelt, Extensional motions of spatially periodic lattices, *Int. J. Multiphase Flow* **18**, 1045-1059 (1992).
- Kröger, M., Simple models for complex nonequilibrium fluids, *Phys. Rep.* **390**, 453-551 (2004).
- Kröger, M., Shortest multiple disconnected path for the analysis of entanglements in two- and three-dimensional polymeric systems, *Comput. Phys. Commun.* **168**, 209-232 (2005).
- Kröger, M., and S.J. Hess, Rheological evidence for a dynamical crossover in polymer melts via nonequilibrium molecular dynamics, *Phys. Rev. Lett.* **85**, 1128-1131 (2000).
- Kröger, M., W. Loose, and S.J. Hess, Rheology and structural changes of polymer melts via nonequilibrium molecular dynamics, *J. Rheol.* **37**, 1057-1079 (1993).
- Kröger, M., J. Ramirez, and H.C. Öttinger, Projection from an atomistic chain contour to its primitive path, *Polymer*, **43**, 477-487 (2002).
- Larson, R.G., *The structure and rheology of complex fluids* (Oxford university press, New York, 1999).
- LeDuc, P., C. Haber, G. Bao, and D. Wirtz, Dynamics of individual flexible polymers in a shear flow, *Nature* **399**, 564-566 (1999).
- Liu, T.W., Flexible polymer chain dynamics and rheological properties in steady flows, *J. Chem. Phys.* **90**, 5826-5842 (1989).



- Marrucci, G., Dynamics of entanglements: A nonlinear model consistent with the cox-merz rule, *J. Non-Newtonian Fluid Mech.* **62**, 279-289 (1996)
- Mavrantzas, V.G., and H.C. Öttinger, Atomistic monte carlo simulations of polymer melt elasticity: Their nonequilibrium thermodynamics generic formulation in a generalized canonical ensemble, *Macromolecules* **35**, 960-975 (2002).
- Mavrantzas, V.G., and D.N. Theodorou, Atomistic simulation of polymer melt elasticity: Calculation of the free energy of an oriented polymer melt, *Macromolecules* **31**, 6310-6332 (1998).
- Moore, J. D., S.T. Cui, H.D. Cochran, and P.T. Cummings, A molecular dynamics study of a short-chain polyethylene melt. I. Steady-state shear, *J. Non-Newtonian Fluid Mech.* **93**, 83-99 (2000).
- Morrison, F.A., *Understanding Rheology* (Oxford University Press, New York, 2001).
- Morriss, G.P., P.J. Daivis, and D.J. Evans, The rheology of n-alkanes: Decane and eicosane, *J. Chem. Phys.* **94**, 7420-7433 (1991).
- Müller-Plathe, F., Coarse-Graining in Polymer Simulation: From the Atomistic to the Mesoscopic Scale and Back, *Chemphyschem.* **3**, 757-769 (2002)
- Nair, D.M., and J.D. Schieber, Linear viscoelastic predictions of a consistently unconstrained Brownian slip-link model, *Macromolecules* **39**, 3386-3397 (2006).
- Öttinger, H. C., *Stochastic processes in polymeric fluids* (Springer, Berlin, 1996).
- Öttinger, H.C., A thermodynamically admissible reptation model for fast flows of entangled polymers, *J. Rheol.* **43**, 1461-1493 (1999).

- Robertson, R.M., and D.E. Smith, Direct measurement of the intermolecular forces confining a single molecule in an entangled polymer solution, *Phys. Rev. Lett.* **99**, 126001 (2007).
- Schieber, J.D., D.M. Nair, and T. Kitkrailard, Comprehensive comparisons with nonlinear flow data of a consistently unconstrained Brownian slip-link model, *J. Rheol.* **51**, 1111-1141 (2007).
- Schroeder, C.M., R.E. Teixeira, E.S.G. Shaqfeh, and S. Chu, Characteristic periodic motion of polymer in shear flow, *Phys. Rev. Lett.* **95**, 018301 (2005).
- Shanbhag, S., and M. Kröger, Primitive path networks generated by annealing and geometrical methods: Insights into differences, *Macromolecules* **40**, 2897–2903 (2007).
- Siepmann, J.I., S. Karaboni, and B. Smit, Simulating the critical behaviour of complex fluids, *Nature* **365**, 330-332 (1993).
- Smith, D.E., H.P. Babcock, and S. Chu, Single-polymer dynamics in steady shear flow, *Science* **283**, 1724-1727 (1999).
- Smith, D.E., and S. Chu, Response of flexible polymers to a sudden elongational flow, *Science* **281**, 1335-1340 (1998).
- Somasi, M., B. Khomami, N.J. Woo, J.S. Hur, and E.S.G. Shaqfeh, Brownian dynamics simulations of bead-rod and bead-spring chains: numerical algorithms and coarse-graining issues, *J. Non-Newtonian Fluid Mech.* **108**, 227-255 (2002)
- Souvaliotis, A., and A.N. Beris, An extended white–metzner viscoelastic fluid model based on an internal structural parameter, *J. Rheol.* **36**, 241-271 (1992).

- Stoltz, C., J.J. de Pablo, and M.D. Graham, Concentration dependence of shear and extensional rheology of polymer solutions: Brownian dynamics simulations, *J. Rheol.* **50**, 137-167 (2006).
- Teixeira, R.E., H.P. Babcock, E.S.G. Shaqfeh, and S. Chu, Shear thinning and tumbling dynamics of single polymer in the flow-gradient plane, *Macromolecules* **38**, 581-592 (2005).
- Teixeira, R.E., A.K. Dambal, D.H. Richter, E.S.G. Shaqfeh, and S. Chu, The individualistic dynamics of entangled DNA in solution, *Macromolecules* **40**, 2461-2476 (2007).
- Todd, B.D., and P.J. Daivis, Nonequilibrium molecular dynamics simulations of planar elongational flow with spatially and temporally periodic boundary conditions, *Phys. Rev. Lett.* **81**, 1118-1121 (1998).
- Todd, B.D. and P.J. Daivis, The stability of nonequilibrium molecular dynamics simulations of elongational flows, *J. Chem. Phys.* **112**, 40-46 (2000).
- Treloar, L.R.G., *The physics of rubber elasticity* (Oxford university press, Oxford, 1975).
- Tsolou, G., V.G. Mavrantzas V. G., and D.N. Theodorou, Detailed atomistic molecular dynamics simulation of *cis*-1,4-poly(butadiene), *Macromolecules* **38**, 1478-1492 (2005).
- Tuckerman, M., B.J. Berne, and G.J. Martyna, Reversible multiple time scale molecular dynamics, *J. Chem. Phys.* **97**, 1990-2001 (1992).
- Tzoumanekas, C. and D.N. Theodorou, Topological analysis of linear polymer melts: a statistical approach, *Macromolecules* **39**, 4592-4604 (2006).

- Venkataramani, V., R. Sureshkumar, and B. Khomami, Coarse-grained modeling of macromolecular solutions using a configuration-based approach, *J. Rheol.* **52**, 1143-1177 (2008).
- Vladkov, M., and J.L. Barrat, Linear and nonlinear viscoelasticity of a model unentangled polymer melt: Molecular dynamics and rouse modes analysis, *Macromol. Theory Simul.* **15**, 252-262 (2006).
- Williams, G., and D.C. Watts, Non-symmetrical dielectric relaxation behaviour arising from a simple empirical decay function, *Transactions of the Faraday Society* **66**, 80-85 (1970).
- Williams, G., D.C. Watts, S.B. Dev, and A.M. North, Further considerations of non symmetrical dielectric relaxation behaviour arising from a simple empirical decay function, *Transactions of the Faraday Society* **67**, 1323-1335 (1971).
- Zylka, W., and H.C. Öttinger , A comparison between simulations and various approximations for Hookean dumbbells with hydrodynamic interaction, *J. Chem. Phys.* **90**, 474-480 (1989).

## **Vitae**

Jun Mo Kim was born in Pohang, Kyungbuk-do, South Korea on March 15, 1978. He grew up there and went to Jungang elementary school, Sangdo middle school, and Pohang high school. After graduating high school, he went to Korea university, Seoul, in 1997. He also finished his compulsory military service as a decontamination soldier from March 11, 1999 to May 10, 2001. After military service, he continued undergraduate study and worked at Polymer Blends & Characterization Lab. as an undergraduate researcher from 2003 to 2005. He also worked at Michigan State University from February to August 2004, and was supported by the Korea Science and Engineering Foundation (KOSEF). He received the B.E degree in Chemical & Biological Engineering in 2005. In 2005, he was admitted to study in the Master of science program of the Chemical & Biomolecular Engineering Department at University of Tennessee, Knoxville, and received his Master of science degree in 2007. He continued to pursue his Ph. D program at the same institution, and published five journal papers.